



PONTIFICIA UNIVERSIDAD CATOLICA DE CHILE  
SCHOOL OF ENGINEERING

# **SEISMIC DEMANDS IN REINFORCED CONCRETE WALLS IN BUILDINGS WITH COUPLING SLABS**

**LILIBETH RAMOS CASTILLO**

Thesis submitted to the Office of Graduate Studies in partial fulfillment  
of the requirements for the Degree of Doctor in Engineering Sciences

Advisor:

**MATÍAS HUBE GINESTAR**

Santiago de Chile, enero, 2022

© 2022, Lilibeth Ramos Castillo



PONTIFICIA UNIVERSIDAD CATOLICA DE CHILE  
SCHOOL OF ENGINEERING

# SEISMIC DEMANDS IN REINFORCED CONCRETE WALLS IN BUILDINGS WITH COUPLING SLABS

LILIBETH RAMOS CASTILLO

Members of the Committee:

**MATÍAS HUBE**

DocuSigned by:

*Matías Hube G.*

363F8AB9C14E4EC...

**DIEGO LÓPEZ-GARCÍA**

DocuSigned by:

*Diego López-García*

7170C26055AA4D4...

**RODRIGO JORDÁN**

DocuSigned by:

*Rodrigo Jordán*

F4EB982663B2452...

**LEONARDO MASSONE**

DocuSigned by:

*Leonardo Massone S.*

13031052A59D466...

**CARLOS ARTETA**

DocuSigned by:

*Carlos Arteta*

7C1231BF69964D0...

**GUSTAVO LAGOS**

DocuSigned by:

*Gustavo Lagos C.*

B558E9FD3B4641F...

Thesis submitted to the Office of Graduate Studies in partial fulfillment  
of the requirements for the Degree Doctor in Engineering Sciences

Santiago of Chile, January 2022

To my parents who never doubted me,  
and to my Ph.D. colleagues who made  
this journey enjoyable.

## ACKNOWLEDGEMENTS

Firstly, I would like to thank God for giving me the chance to start this journey and finish it satisfactorily. I would also like to especially thank my family for their constant support and trust in me. Thanks for encouraging me to complete this objective. For listening to me during difficult times, for giving me strength when I needed it. I would have never achieved my goals without their support. I want to especially thank my advisor, Professor Matías Hube, for his guide, knowledge, motivation, and support throughout this entire project. I appreciate all the time he spent encouraging me and guiding me in this process. I would like to thank Juan Diego Pozo and Santiago Tagle for their outstanding collaboration in using the DIANA software and for their excellent disposition to resolve my doubts and to José Gallardo for his help with the improvement of the figures and his collaboration with the discussion of some results.

My thanks also go to the faculty of the Structural and Geotechnical Engineering Department of the Pontificia Universidad Católica de Chile, especially to the professors Rodrigo Jordán and Diego Lopez-Garcia for their encouragement and comments to my research. I also thank Professors Leonardo Massone and Carlos Arteta for their valuable comments on this thesis. I would also like to thank all those people who participated in one way or another in my formation as a researcher, professional and as a human being. To my friends: Tamara, to the Legion team and the Ecuadorian team for their support in bad times, but most importantly, for all the good moments we share and for helping make my time in Chile a memorable experience.

Finally, I am grateful for the financial support of the ANID agency through the scholarship Doctorado Nacional 21151525, ANID/Fondecyt/1171062, and ANID/FONDAP/15110017.

## TABLE OF CONTENTS

	Page.
DEDICATION .....	ii
ACKNOWLEDGEMENTS .....	iii
LIST OF TABLES .....	6
LIST OF FIGURES.....	7
RESUMEN.....	11
ABSTRACT .....	13
1. INTRODUCTION .....	15
1.1 Motivation .....	15
1.2 Literature review .....	17
1.3 Hypothesis and objectives.....	22
1.4 Methodology .....	24
1.5 Dissertation organization.....	25
2. CONTRIBUTION OF COUPLING ELEMENTS TO THE LINEAR SEISMIC DEMAND OF WALLS IN RC BUILDINGS .....	27
2.1 Introduction .....	27
2.2 Building description .....	28
2.3 Finite element models and ground motions .....	31
2.3.1 Ground motions .....	33
2.4 Seismic demand on walls and contribution of coupling elements .....	35
2.5 Influence of the modeling assumptions.....	49
3. STATIC ANALYSIS OF RC WALL BUILDING WITH NON-LINEAR COUPLING SLABS.....	58
3.1 Introduction .....	58
3.2 Case study building .....	59
3.3 Non-linear finite element models.....	63
3.4 Effect of the reduced moment of inertia of slabs .....	76
3.5 Seismic behavior of the building with non-linear coupling slabs .....	80

3.6	Effect of slab reinforcement .....	91
4.	DYNAMIC ANALYSIS OF RC WALL BUILDING WITH NON-LINEAR COUPLING SLABS .....	100
4.1	Introduction .....	100
4.2	Ground motions and analysis considerations .....	100
4.3	Dynamic response of the building with non-linear slabs .....	102
4.4	Comparison between the dynamic and the static response .....	110
4.5	Effect of the slab reinforcement in the dynamic response. ....	115
5.	CONCLUSIONS .....	118
	REFERENCES .....	124

## LIST OF TABLES

	Page.
Table II- 1: General characteristics of RC buildings considered in this investigation.....	30
Table II- 2: PGA of ground motions, spectral displacements at the fundamental building periods, and scaling factors for the buildings CM and AH located in Concepcion .....	34
Table II- 3: PGA of ground motions, spectral displacements at the fundamental building periods, and scaling factors for the SO building located in Santiago .....	34
Table II- 4: Modelling assumptions considered for each building.....	50
Table II- 5: Fundamental periods of the three buildings with the four modelling assumptions .....	51
Table II- 6: Maximum roof drift ratio (%) predicted for each building for the six ground motions .....	52
Table II- 7: Axial Loads Ratios for all selected walls in the three buildings.....	56
Table III- 1: Computational time needed to obtain the results from models with different mesh size. ....	73
Table III- 2: Numerical models of the case study building.....	75
Table III- 3: Strength, overstrength factor and deformation capacity, LS100, LS40, LS25, LS10, and NLS1 models. ....	78
Table III- 4: Strength, overstrength factor, deformation capacity and parameters of the idealized bi-linear constitutive, NLS1, NLS2, and NLS3 models. ....	93
Table IV- 1: ALRs predicted with the three seismic records at similar roof drift ratios. ..	108
Table IV- 2: Maximum roof drift ratios and corresponding base shear forces predicted with the three seismic records .....	111
Table IV- 3: Maximum base shear forces and corresponding roof drift ratios predicted with the three seismic records. ....	112

## LIST OF FIGURES

	Page.
Figure 1- 1 Floor plan layout of three existing residential Chilean buildings.....	16
Figure 2- 1: 2010 Chile earthquake hypocenter and location of Santiago and Concepción cities. ....	29
Figure 2- 2: Plan view of typical story of considered buildings: a) CM; b) AH; c) SO. Considered walls in this study are shown in red. ....	31
Figure 2- 3: 3D views of the finite element models: a) CM building; b) AH building; c) SO building.....	32
Figure 2- 4: Pseudo-acceleration and displacement response spectrum for selected ground motions (5% damping ratio).....	33
Figure 2- 5: Elevation view and cross-sections of studied walls: a) wall E-CM; b) wall V-AH; and c) wall U-SO.....	36
Figure 2- 6: Representative a) three-dimensional layout of a pier, slabs, and beams and b) pier forces at the i-th story.....	39
Figure 2- 7: Seismic contribution of coupling elements to: a) P of E-CM wall; b) V of E-CM wall; c) M of E-CM wall; d) P of V-AH wall; e) V of V-AH wall; f) M of V-AH wall; g) P of U-SO wall; h) V of U-SO wall and i) M of U-SO wall. (G.L. corresponds to the ground level).....	41
Figure 2- 8: Contribution of the coupling elements to the gravitational axial load in: a) E-CM wall; b) V-AH wall, and c) U-SO wall (G.L. correspond to the ground level).....	44
Figure 2- 9: Compressive axial load demand envelopes for the three seismic records and two possible orientations: a) wall E-CM; b) V-AH; and c) U-SO. ....	45
Figure 2- 10: Shear demand envelopes for the three seismic records and two possible orientations: a) wall E-CM; b) V-AH; and c) U-SO. ....	46
Figure 2- 11: Moment demand envelopes for the three seismic records and two possible orientations: a) wall E-CM; b) V-AH; and c) U-SO. ....	47
Figure 2- 12: Median contribution of coupling elements to the maximum seismic axial load of walls at the first story for compression (a) and tension (b).....	48

Figure 2- 13: Seismic ALRs of eight walls at the first story in: a) compression (shown with positive values) and b) tension. ....	49
Figure 2- 15: Seismic demand for four modeling assumptions: a) P of E-CM wall; b) V of E-CM wall; c) M of E-CM wall; d) P of V-AH wall; e) V of V-AH wall; f) M of V-AH wall; g) P of U-SO wall; h) V of U-SO wall and i) M of U-SO wall. (GL corresponds to the ground level). ....	53
Figure 3- 1: Plan view of case study building, representative of the of residential buildings configuration in Chile. ....	60
Figure 3- 2: Reinforcement details of the T-shape walls. a) Special boundary elements for both web and flange and b) web-flange intersection. ....	63
Figure 3- 3: a) Cross-section and reinforcement TW2 wall and b) Experimental and analytical global results; c) and d) Local results for reinforcement strain at the base of the TW2 wall for positive and negative displacement, respectively. ....	66
Figure 3- 4: 3D drawing of the full-scale EUC_BUILD3 prototype (from Brunesi et al. 2018). ....	67
Figure 3- 5. 3D view of the EUC_BUILD3 DIANA model. ....	68
Figure 3- 6: Comparison between experimental cyclic response and monotonic response estimated with the DIANA model. ....	69
Figure 3- 7: a) Three-dimensional; b) elevation; c) plan and d) special boundary elements reinforcement views of the DIANA model (units in meters). ....	70
Figure 3- 8: Comparison of global result (roof drift ratio and total base shear) predicted with models with different mesh size for both walls and slabs. ....	72
Figure 3- 9: Comparison of the axial load ratio predicted with the four models with different mesh size. ....	73
Figure 3- 10: Non-linear static analysis results for the four linear models with linear slabs (LS100, LS40, LS25, and LS10) and the NLS1 model with non-linear slabs. Structural failure is marked with dots. $\delta u$ is the design displacement (0.31%) according to DS61 and $Vu$ the ultimate design shear (0.087W). ....	77
Figure 3- 11 Degree of coupling for the four linear models with linear slabs (LS100, LS40, LS25 and LS10) and the NLS1 model with non-linear slabs. ....	80

Figure 3- 12: Deformation of the building and normal crack strains in concrete with the NLS1 model for roof drift ratios of a) 0.04% (only the slabs of stories 4,7,10, 13, and 16 are shown), b) 0.20%, and c) 0.6% .	82
Figure 3- 13: Predicted forces at the base of the walls for the NLS1 model: a) Axial load ratio; b) Normalized base shear force, and c) Bending moment	83
Figure 3- 14: a) Interaction diagram of the T-shape wall and b) Moment-curvature relationships for gravitational axial load and failure axial load in each wall.	85
Figure 3- 15: Strain demands in longitudinal bars at the base of the walls in the NLS1 model.	88
Figure 3- 16: Strains state at the beginning of the non-linear static analysis in longitudinal bars at the base of the walls in the NLS1 model.	89
Figure 3- 17: Stress-strain relationships in the longitudinal direction at the base of the walls, NLS1 model: a) Concrete in compression and b) Steel in tension.	90
Figure 3- 18: Strain demands of slab reinforcement at each story for a) bottom grid nearest to $W_T$ and b) top grid nearest to $W_C$ .	91
Figure 3- 19: Non-linear static analysis results for NLS1, NLS2 and NLS3 models. Structural failure is marked with dots. $\delta u$ is the design displacement according to the DS61 (0.31%) and $Vu$ the ultimate shear design (0.0087W).	92
Figure 3- 20: Idealized bi-linear constitute relationships for NLS1, NLS2, and NLS3 models.	94
Figure 3- 21: Comparative result for NLS1, NLS2, and NLS3 for the a) Axial load between tensioned and compressed wall; b) Distribution of normalized base shear force and c) Distribution of moment at the base of each wall.	95
Figure 3- 22 Degree of coupling for the NLS1, NLS2, and NLS3 model.	97
Figure 3- 23: Strain demands in most demanded longitudinal bars at the base of the walls, models NLS1, NLS2 and NLS3.	98
Figure 3- 24: Strain demands of slabs reinforcement at each story for top grid in a) NLS2 model and b) NLS3 model.	99
Figure 4- 1: Ground motions and significant duration of the seismic records at station a) SN; b) SC and c) SPA.	101

Figure 4- 2: Roof drift ratio of the study case building predicted with NLS1 model and an elastic model for seismic records: a) SN; b) SC and c) SPA. ....	104
Figure 4- 3: Normalized total base shear (V/W) predicted with NLS1 model and seismic records: a) SN; b) SC and c) SPA. ....	105
Figure 4- 4: Hysteretic response of the base shear and roof displacements of the case study building, for the seismic records: a) SN; b) SC, and c) SPA .....	106
Figure 4- 5: Axial load ratio at the base of each wall predicted with for the NLS1 model for seismic records: a) SN; b) SC, and c) SPA. ....	107
Figure 4- 6 Normalized total base shear (V/W) at the base of each wall predicted with NLS1 model and seismic records at stations: a) SN; b) SC and c) SPA. ....	109
Figure 4- 7: Moment at the base of each wall predicted with NLS1 model and seismic records at stations: a) SN; b) SC and c) SPA. ....	110
Figure 4- 8: Non-linear static results compared with the maximum values predicted with dynamic analysis, NLS1 model.....	112
Figure 4- 9: Forces at the base of the walls for the NLS1 model predicted by the static and dynamic analyses: a) Axial load ratio; b) Normalized shear force, and c) Bending moment. ....	113
Figure 4- 10: Degree of coupling computed from the static and dynamic analysis.....	115
Figure 4- 11: Non-linear dynamic analysis results for NLS1, NLS2 and NLS3 models... ..	116
Figure 4- 12: Comparative Axial load ratio results in $W_C$ from NLS1, NLS2 and NLS3 models. ....	117

PONTIFICIA UNIVERSIDAD CATOLICA DE CHILE  
ESCUELA DE INGENIERIA

DEMANDAS SISMICAS EN EDIFICIOS DE MUROS DE HORMIGÓN ARMADO  
CON LOSAS DE ACOPLAMIENTO

Tesis enviada a la Dirección de Postgrado en cumplimiento parcial de los requisitos para el grado de Doctor en Ciencias de la Ingeniería.

LILIBETH RAMOS CASTILLO

RESUMEN

La capacidad inherente de los muros estructurales de hormigón armado (HA) para soportar cargas sísmicas, controlar los desplazamientos laterales y limitar el daño en los componentes no estructurales ha permitido su amplia aceptación en edificios de gran altura. Chile, Colombia, Nueva Zelanda y Canadá, entre otros países, han adoptado los muros estructurales de HA como el sistema principal de resistencia a fuerza lateral para un porcentaje significativo de sus edificios de altura media a alta. Las configuraciones arquitectónicas de este tipo de edificios fuerzan la conexión de los muros estructurales con losas, vigas y muros adyacentes para distribuir los espacios habitacionales. Debido a la interacción que se genera entre estos elementos, los edificios se comportan como sistemas estructurales acoplados, que deben ser estudiados como tal.

Estudios sobre edificios de HA dañados por el terremoto de Chile de 2010 han señalado a las losas como un elemento clave para comprender el comportamiento sísmico de estos. Algunas investigaciones recientes, han concluido que el comportamiento de los muros de HA estuvo altamente influenciado por la interacción tridimensional (3D) de estos con el resto de la estructura. Aún más, otro estudio indicó que la acción de acoplamiento entre muros y losas proporciona una resistencia adicional en los edificios a expensas de reducir la capacidad de deformación de los mismos y de aumentar la demanda de corte en algunos muros. A pesar de los avances en el entendimiento de los edificios de muros de HA con losas de acoplamiento, aún falta conocimiento e información sobre su comportamiento sísmico que requiere investigación adicional. Entonces resulta importante evaluar el comportamiento no lineal de las losas para obtener información adicional sobre su influencia en el comportamiento sísmico de los edificios de muros de HA.

La interacción entre muros, losas y vigas en los edificios de HA es la motivación de esta investigación. El objetivo principal es identificar cómo la interacción tridimensional de los elementos conectados afecta las demandas sísmicas de los muros de HA en edificios residenciales chilenos. Adicionalmente, analiza el efecto del comportamiento no lineal de las losas como factor clave para entender mejor el comportamiento de dichos edificios. Este trabajo consta de dos partes. La primera considera modelos lineales de edificios con muros de HA, y la segunda modelos no lineales de un edificio de caso de estudio.

En la primera parte se revisan las demandas sísmicas lineales de carga axial, corte y momento de los muros de HA, estimadas a partir de modelos lineales de elementos finitos creados en ETABS de tres edificios dañados durante el terremoto de Chile de 2010. Las fuerzas de los elementos obtenidas de estos modelos se utilizan para cuantificar la contribución de losas, vigas y muros adyacentes, a las demandas sísmicas de los muros estudiados. Adicionalmente, se evalúa la influencia de utilizar diferentes valores de momentos de inercia para los elementos estructurales y diferentes supuestos de diafragma para las losas. Los resultados muestran que las losas tuvieron la mayor contribución a la carga axial sísmica en los muros, con más del 90% de contribución, seguidas de los muros adyacentes y las vigas de conexión. Adicionalmente, se concluyó que la supuesta rigidez de los elementos estructurales tiene una influencia significativa en la predicción de las demandas sísmicas de los muros de HA. Los resultados obtenidos apoyan el hecho de que la rigidez en el plano asumida para las losas influye en la predicción de las demandas sísmicas de los muros.

La segunda parte de la investigación se centra en la respuesta sísmica no lineal de edificios de muros de HA con losas de acoplamiento no lineales. En esta parte, se crearon siete modelos 3D no lineales de un edificio de estudio que representa una estructura residencial en Chile. Los modelos se construyeron en el programa DIANA y la respuesta sísmica del edificio se evalúa considerando análisis no lineales estáticos y dinámicos. Los parámetros de respuesta que se consideran son el desplazamiento de techo, el corte basal, el momento y la carga axial de los muros. También fueron evaluadas las demandas de deformaciones unitarias del hormigón y el acero de refuerzo en muros y losas. Los resultados de los primeros cuatro modelos se utilizan para determinar la precisión de modelos con muros no lineales y losas lineales con momento de inercia reducido para representar la respuesta del edificio con comportamiento completamente no lineal. Los últimos tres modelos se utilizan para evaluar el efecto de la cuantía de refuerzo de losas de acoplamiento sobre la respuesta sísmica del edificio de caso de estudio. De esta segunda parte de la investigación se concluye que ninguno de los modelos con muros no lineales y losas lineales con momento de inercia reducido es capaz de predecir con precisión la relación fuerza-desplazamiento del modelo con comportamiento completamente no lineal. Adicionalmente, se encontró que el aumento del refuerzo de la losa aumentó la resistencia lateral del edificio, pero disminuyó la capacidad de deformación del mismo. En base a los resultados obtenidos, se pueden hacer dos importantes recomendaciones de diseño: 1) utilizar un factor de reducción de momento de inercia de entre 0.25 y 0.4 para simular las losas en modelos no lineales con losas elásticas y 2) el aumento del refuerzo longitudinal en losas de acoplamiento es perjudicial para el desempeño sísmico del edificio porque disminuye la capacidad de deformación.

Miembros de la Comisión de Tesis Doctoral  
MATÍAS HUBE GINESTAR  
DIEGO LOPEZ GARCIA  
RODRIGO JORDAN  
LEONARDO MASSONE  
CARLOS ARTETA  
GUSTABO LAGOS  
Santiago, enero, 2022

PONTIFICIA UNIVERSIDAD CATOLICA DE CHILE  
ESCUELA DE INGENIERIA

SEISMIC DEMANDS IN REINFORCED CONCRETE WALLS IN BUILDINGS WITH  
COUPLING SLABS

A thesis submitted to the Office of Graduate Studies in partial fulfillment of the  
requirements for the Degree of Doctor in Engineering Sciences by

LILIBETH RAMOS CASTILLO

ABSTRACT

The inherent capacity to withstand seismic loads, to control lateral displacements, and limit damage on nonstructural components of reinforced concrete (RC) structural walls has allowed for their wide acceptance in high-rise buildings. Chile, Colombia, New Zealand, and Canada, among other countries, have adopted RC structural walls as the lateral force-resisting system for a significant percentage of their mid to high-rise buildings. Architectural configurations of these kinds of buildings force the connection of structural walls with slabs, beams, and adjacent walls to distribute habitational spaces. Because of the interaction between the structural elements, the buildings behave as coupled structural systems, which must be studied as such.

Studies on RC buildings damaged by the 2010 Chile earthquake have pointed the slabs as a key element for understanding the seismic behavior of the buildings. Recent investigations have concluded that the RC walls' behavior was highly influenced by the three-dimensional (3D) interaction of the walls with the rest of the structure. Moreover, another study indicated that the coupling action between walls and slabs provides additional resistance at the expense of reducing the drift capacity of the building and increased the shear demand in some walls. Notwithstanding the advances in the understanding of the RC wall buildings with coupling slabs, there is still a lack of knowledge and information regarding their seismic behavior, which requires additional investigation. Therefore, assessing the non-linear behavior of slabs is important to get further information about their influence on the seismic behavior of RC wall buildings.

The interaction between walls, slabs, and beams in RC buildings is the motivation of this investigation. The main objective is identify how, through the 3D interaction, the connected elements affect the seismic demands of RC walls in Chilean residential buildings. Additionally, the effect of the non-linear behavior of the slabs is analyzed as a key factor to understand the overall behavior of such buildings better. Therefore, this research work comprises two parts. The first part considers elastic models of RC wall buildings, and the second part considers non-linear models of a case study building.

The first part explores the linear seismic demands of axial load, shear, and moment of RC walls, estimated from three buildings damaged during the 2010 Chile earthquake using detailed elastic finite element models in ETABS. The elements forces obtained from such models are used to quantify the contribution of the connected structural elements to the seismic demands of the studied walls. Additionally, the influence of using different moments of inertia for the structural elements and different diaphragm assumptions for the slabs were evaluated. It was found that slabs have the most significant contribution to the seismic axial load in walls, contributing more than 90%, followed by adjacent walls (walls connected to the analyzed wall) and connecting beams. Furthermore, it is concluded that the assumed stiffness of structural elements significantly influences the prediction of the seismic demands in RC walls. The results support that the assumed in-plane slabs stiffness affects the prediction of the seismic demands on walls.

The second part of the research focuses on the non-linear seismic response of RC buildings with non-linear slabs. In this part, seven three-dimensional non-linear models of a case study building, representing a typical residential structure in Chile, were created in DIANA. The seismic response of the building is evaluated from the results of roof displacement, shear, moment, and axial forces of the walls obtained through non-linear static and dynamic analysis. The predicted strain demands of concrete and steel in both walls and slabs are also reviewed. Results from the first four models are used to determine the accuracy of models with non-linear walls and elastic slabs with reduced moment of inertia to represent the response of the structure considering a total non-linear behavior.

Additionally, the last three models are used to evaluate the effect of the reinforcement ratio of the coupling slabs on the seismic response of the case study building. It is concluded from this part of the research that none of the models with non-linear walls and linear slabs with reduced moment of inertia are able to predict the force-displacement relationship of the full non-linear model accurately. Additionally, it was found that even though an increase of the slab reinforcement increases the lateral strength of the building, it decreases the deformation capacity of the building. Based on the results, two important design recommendations can be made: 1) use a moment of inertia reduction factor between 0.25 and 0.4 for simulating the slabs in non-linear models with elastic slabs and 2). It is not recommended to increase the reinforcement in coupling slabs to avoid affecting the deformation capacity of the buildings.

Members of the Doctoral Thesis Committee:

MATÍAS HUBE GINESTAR

DIEGO LOPEZ GARCIA

RODRIGO JORDAN

LEONARDO MASSONE

CARLOS ARTETA

GUSTABO LAGOS

Santiago, January, 2022

## 1. INTRODUCTION

### 1.1 Motivation

Reinforced concrete (RC) structural walls are used worldwide due to their capacity to withstand seismic loads, control lateral displacements, and limit damage on nonstructural components. The construction of RC wall buildings is also known to be very competitive because simple formwork and low congested reinforcement lead to reduced labor costs and fast construction. Chile, Colombia, New Zealand, and Canada, among other countries, have adopted RC structural walls as the lateral force-resisting system for a significant percentage of their mid- to high-rise buildings (Wallace et al. 2012; Kam et al. 2011; Blandón et al. 2018). Particularly in Chile, this structural system is the most used in residential buildings (Massone et al. 2012).

Figure 1- 1 shows the floor plan layout of three existing Chilean residential buildings. These buildings are characterized by having several RC walls in both directions, which are connected mainly through RC slabs. Some beams are present in these buildings, which are used to support balconies and, in a few cases, to connect the walls. Walls with rectangular and non-rectangular cross-sections are common in these buildings. The connection between walls and slabs generates an interaction between these structural elements causing the buildings to behave as a coupled structural system, which must be studied as such.

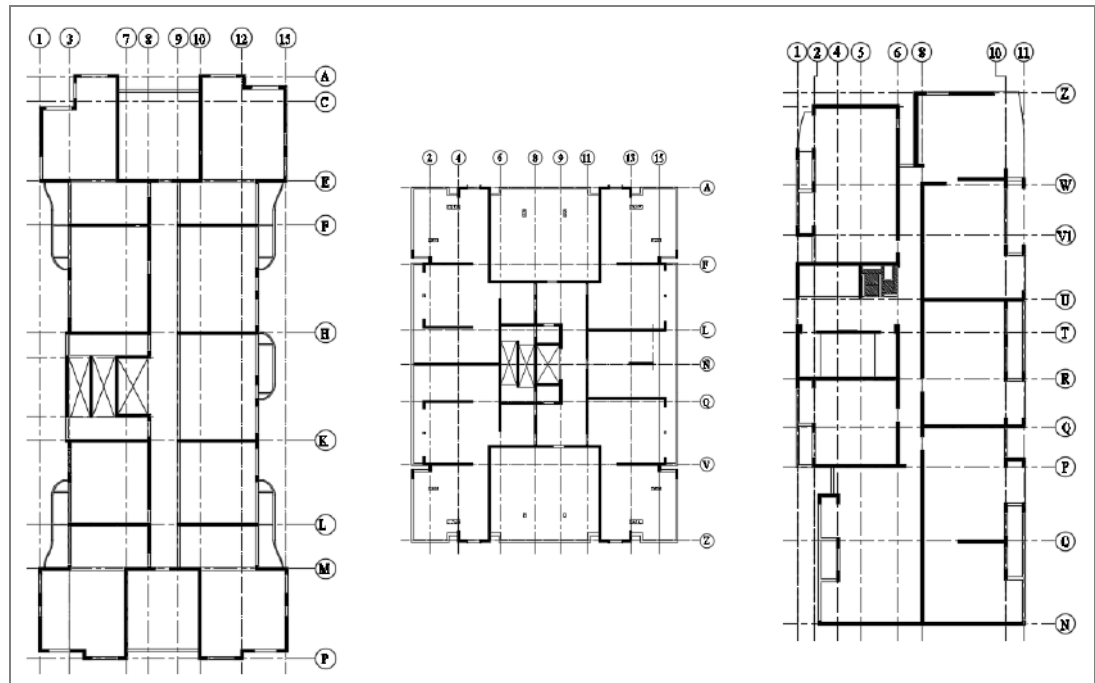


Figure 1- 1 Floor plan layout of three existing residential Chilean buildings.

Predicting the seismic response of RC wall buildings with coupling slabs is difficult. The complex geometry configurations and the three-dimensional (3D) interaction between the structural elements need to be considered. Furthermore, the connected structural elements contribute to the seismic demands of the RC walls. Hence, to further understand the seismic response of walls within RC buildings, it is critical to properly identify how through the 3D interaction, the connected elements affect the seismic demands in such walls.

The interaction between walls, slabs, and beams in RC buildings motivates the investigation presented in this thesis. This research aims to quantify the contribution of coupling elements to the seismic demands of RC walls in Chilean residential buildings. Additionally, the effect of the non-linear behavior of the slabs on the seismic demands of RC walls is analyzed.

## 1.2 Literature review

As mentioned in the previous section, RC walls are a common lateral force resisting system worldwide due to their advantages. Particularly, the structural system of multistory residential buildings in Chile is based on RC walls. These buildings are characterized by having a large wall density per floor (Jünemann et al. 2015). In other countries, RC wall buildings have fewer walls, and they are combined with RC frames to carry gravity loads, while internal partitions are made with masonry or drywalls. The behavior of both kinds of RC wall buildings during an earthquake has been the main subject of several studies (Wallace et al. 2012; Blandón et al. 2018; Fischinger et al. 2017; Lehman et al. 2013). Moreover, some studies have focused on understanding the behavior of entire buildings (Jünemann et al. 2016b; Cando et al. 2020; Ugalde and Lopez-Garcia 2020), and some others have focused on understanding the behavior of isolated walls (Pozo et al. 2020; Massone et al. 2019; Santa Maria et al. 2017).

After the 2010 earthquake in Chile and the 2010 and 2011 earthquakes in New Zealand, significant research has been conducted on RC wall buildings. Some of these studies have tried to describe and identify the possible causes of the observed damage. Westenenk et al. (2012) presented a thorough damage survey for eight damaged buildings in Concepción (Chile), including a detailed description of the buildings. In addition, Westenenk et al. (2013) presented a complete code-type analysis of four damaged buildings and studied critical aspects like building orientation, vertical and horizontal irregularities, wall detailing, and energy dissipation sources. Wallace et al. (2012) described the observed damage in RC wall building and analyzed critical aspects such as the lack of confinement at wall boundaries, wall cross-section, and axial loads on walls, including suggestions to design special RC structural walls. These authors concluded that Chilean buildings remained essentially elastic during the 2010 earthquake until an abrupt brittle failure occurred in some cases. The observed damage was produced by a combination of bending and axial effects, and that the failure was

characterized by concrete crushing and spalling of the concrete cover (Jünemann et al. 2016a; Vásquez et al. 2020).

Other investigations related to the behavior of Chilean RC wall buildings were focused mainly on the description of the observed damage and the typical design and construction practices (Carpenter et al. 2011; Rojas et al. 2011 and Massone et al. 2012). Similarly, Kam et al. (2011) described observations of damaged RC buildings after the 2011 Christchurch earthquake.

On the other hand, several researchers have conducted experimental campaigns to assess the seismic behavior of isolated RC walls. Some of these investigations focused on reproducing the failure observed after the 2010 Chile earthquake and analyzing some characteristics of the walls, which may have influenced the observed behavior. For instance, Alarcon et al. (2014) and Hube et al. (2014) tested 1/2-scale slender RC walls using a quasi-static cyclic incremental lateral displacement protocol with a constant axial load. The main variables analyzed were the axial load ratio, wall thickness, wall aspect ratio, distribution of vertical reinforcement, and the effect of the addition of stirrups and crossties at wall boundaries. Furthermore, Massone et al. (2014), and Arteta et al. (2014), tested RC boundary elements with different levels of confinement under pure compression. These authors concluded that additional confining reinforcement could not prevent a limited ductile behavior of boundary elements when subjected to pure compression. More recently, Massone et al. (2019) tested slender RC walls with discontinuities of different sizes at the base and concluded about the effect of the degree of the discontinuity on the plastic hinge length of the walls.

Other experimental campaigns of isolated RC walls were aimed to identify potential deficiencies in current codes design provisions (Segura and Wallace 2018 and Sritharan et al. 2014). Sritharan et al. (2014) conducted an experimental study of the performance of RC walls after the 2010 and 2011 earthquakes in New Zealand and they provided suggestions to improve the performance of RC wall buildings in future earthquakes.

Regarding the numerical simulation of the seismic response of RC walls, macroscopic and microscopic models have been proposed (Kolozvari et al. 2018). The macroscopic models represent walls by simplified non-linear elements, which simulate the behavior of concrete, steel bars and their interaction under cyclic loads. Their formulations are typically characterized by simplifying assumptions (e.g., plane-sections-remain-plane hypothesis, uncoupled flexural and shear responses, assumption of uniformly distributed shear strains along the wall cross-section, etc.) (Kolozvari et al. 2018). Examples of these models are: the Multiple Vertical Line Element Model with and without shear flexural interaction. (Orakcal and Wallace 2006; Chowdhury and Orakcal 2013; Kolozvari et al. 2015a; Kolozvari et al. 2015b; Orakcal et al. 2004); distributed-plasticity beam-column models with fiber sections with and without flexural-shear interaction (Chen et al. 2011; Vázquez et al. 2016; Pugh et al. 2015; Pozo et al. 2021); the Beam-Truss-Model (Panagiotou et al. 2012); and models with concentrated plasticity (Jiang and Kurama 2010; Magna et al. 2014).

Microscopic models correspond to those based on Finite Element (FE) formulations and generalized multi-dimensional constitutive models, which provides the potential to capture wall responses for a wide range of configurations and behavioral features (Kolozvari et al. 2019). Some of the analytical formulations considered on these models are: the four-node reinforced concrete element (Wong et al. 2002); Fixed-Strut-Angle Finite Element (FSAFE) (Gullu and Orakcal 2021); quadrilateral layered membrane element with drilling degrees of freedom (QLMEDD) (Sezen and Moehle 2004); and curved shell element (TNO DIANA 2017).

The seismic behavior of RC wall buildings with floor plan configurations different from that of the described residential Chilean building has also been studied. Most of such studies have considered walls coupled by beams, which is a common structural configuration used in other countries. Harries et al. (2004) contributed to identifying optimal geometrical configurations for such kinds of coupled walls, and Lehman et al. (2013) contributed to identify their failure mechanism by using real scale models. A pre-design method has also been proposed (Aksogan et al. 2014), and a comparison

between the force and displacement design methods has been performed (Fox et al. 2014a). Additionally, Fox et al. (2014b) compared three different methods for the capacity design of coupled walls. Furthermore, procedures for estimating the inelastic response of higher modes for coupled walls were proposed by Pennucci et al. (2015), and for estimating the seismic shear demand of buildings with coupled walls-beams were developed by Pugh et al. (2017). Finally, a shake table test of a five-story RC coupled wall subassembly (Fischinger et al. 2017), representative of a residential building in central Europe, showed that coupled beams induced axial loads in the walls, which contributed to the sudden shear failure of the walls.

As part of the studies related to walls coupled with coupling beams, there are those, which investigated the degree of coupling of such structures. The Canadian concrete standard CAN3 A23.3-94 (CAN3 1994) defined the degree of coupling as the percentage of base overturning moment resisted by the coupled response of the walls; that is axial compression and tension in the walls resulting from shears in coupling beams. Harries (1995) investigates the behavior of RC coupled walls system through two experimental programs. Furthermore, Harries (2001) assessed the degree of coupling of many non-linear analyses performed under different circumstances, and with different analysis assumptions from his work, some limits on the degree of coupling were proposed. Meftah et al. (2013) studied how to improve the seismic performance of different scale RC coupled wall structures, enhancing the degree of coupling by reducing the lateral displacements of system by means of using composite material in the coupling beams. Additionally, Chandran et al. (2014) compared isolated walls with coupled walls changing the beam slenderness in the coupled wall system, concluding that the beam slenderness determines if the coupled system's behavior is similar to the isolated wall or not.

Furthermore, several authors have studied the behavior of slabs within RC wall-slab coupled systems. Schwaighofer and Collins (1977) and Paulay and Taylor (1981) analyzed the influence of concrete cracking on the effective stiffness of the slabs using monotonic and cyclic tests. These authors concluded that a considerable loss of

stiffness of the slab occurs because of cracking. Lim (1989) reported the response of four 1/3-scale slab-wall systems subjected to deformation cycles. This latter investigation describes the cracking sequence and the variation of stresses and strains in RC slabs. More recently, Hossain (2003) studied analytically and experimentally the non-linear behavior of a subassembly of two walls coupled by a RC slab. This author analyzed the failure modes of the slab and concluded that cracking in the slabs started near the edges of the wall, at the interior of the slab, and gradually propagated towards the edges of the slab. Additionally, the tests showed that the slab reinforcement located close to the interior edges of the walls yielded first, and the slab reinforcement far from the walls yielded later. Recently, Kaushik et al. (2016) investigated the seismic damage in wall-slab junctions using finite element models constructed in ABAQUS. From the results of response history analyses, those authors concluded that the predicted damage in slabs highlights the need for guidelines for designing slabs in earthquake-resistant systems.

Finally, few researchers have investigated the overall behavior of 3D RC wall buildings with coupling slabs. NIST (2014) and Ramos and Hube (2016) studied the increase of axial loads in walls due to the coupling effect of slabs in RC buildings using linear numerical models. Jünemann et al. (2016a) conducted a 3D dynamic non-linear analysis of an RC wall building damaged during the 2010 Chile earthquake and concluded that the 3D interaction of the walls with the rest of the structure is a key factor for understanding the seismic behavior of the studied building. Additionally, Gallardo et al. (2021) used an ANSYS model to reproduce the patterns of failure observed in another RC wall building damaged after the 2010 Chile earthquake. These authors concluded that the effective stiffness of the slabs is relevant for the seismic building response. Cando et al. (2019) evaluated the effect of the stiffness on the seismic performance of Chilean residential buildings using non-linear models on OpenSees. Zhang et al. (2017) assessed the collapse of an RC wall building with a 3D non-linear model. They concluded that the coupling action between slabs and walls along the central corridor of the building is one of the reasons for the large reserve of lateral strength identified in such building. Additionally, the authors concluded that the

coupling action between walls and slabs provides additional resistance at the expense of reducing the drift capacity of the building and increasing the shear demand in some walls. Finally, Ugalde et al. (2019) studied the seismic capacity of residential Chilean buildings using non-linear 3D models in PERFORM-3D. These latter authors concluded that the stiffness of the slabs was one of the two modeling issues that influenced the most the analyses of the buildings.

Notwithstanding the advances in RC buildings with coupling slabs, there is still a lack of knowledge and information regarding their seismic behavior, which requires additional investigation. How much does the coupling elements contribute to the seismic demands of walls in RC buildings during earthquakes is still an open question. Then, it is relevant to study and identify how through the 3D interaction, the connected elements affect the seismic demands of RC walls. Furthermore, the behavior of the slabs within the RC wall building systems has been identified as a key element to understand the overall behavior of such buildings better. Therefore, assessing the non-linear behavior of slabs is important to get additional information about their influence on the seismic behavior of RC wall buildings.

### **1.3 Hypothesis and objectives**

The main hypothesis of this investigation is that the slabs act as a coupling element within the RC wall buildings, which significantly affect the seismic demands of axial load, shear, and moment in the walls. The following research questions guide this thesis: What are the elastic seismic demands of axial load, shear, and moment on walls in RC buildings? How much do slabs, beams, and adjacent walls contribute to the seismic demands of walls in RC buildings? What is the effect of the assumed stiffness of the slabs on the elastic seismic demands of RC walls? Which are the inelastic seismic demands of axial load, shear, and moment in RC buildings with coupling slabs? Is it possible to estimate the seismic demands of RC walls accurately in buildings using

linear analyses with reduced moment of inertia for the slabs? What is the effect of the slab reinforcement on the non-linear response of RC wall buildings?

To answer the questions above, the main objective of this research is to evaluate with analytical models the seismic demands of walls in RC buildings with coupling slabs.

The specific objectives of this thesis are:

1. Estimate the seismic demand of axial load, shear, and moment of walls in RC buildings using linear models.
2. Quantify the contribution of coupling elements to the seismic demands of axial load, shear, and moment in walls of RC buildings with linear models.
3. Analyze the effect of using different reduced moments of inertia for the structural elements and using different slabs stiffness on the predicted seismic demands of RC walls.
4. Estimate the seismic demands of axial load, shear, and moment of walls in RC buildings with coupling slabs using full non-linear models.
5. Estimate the accuracy of models with linear slabs and reduced moment of inertia to represent the response of models of RC walls buildings with non-linear slabs.
6. Evaluate the effect of the amount of slab reinforcement on the seismic performance of RC walls buildings using full non-linear models.
7. Provide design recommendations for RC walls buildings with coupling slabs.

Findings from this research regarding the coupling action of the slabs are relevant for better understanding the seismic behavior of RC wall buildings. Additionally, the obtained results about the effect of the slabs on the seismic demands of the walls and the overall behavior of the studied RC building could be considered in future updates of seismic design codes in Chile and abroad. Furthermore, results from this investigation indicate that the increase of longitudinal reinforcement in coupling slabs, commonly considered in engineering practice in Chile to increase the strength of the slabs, is detrimental for the building behavior because the deformation capacity is reduced.

## 1.4 Methodology

This research work is comprised of two parts. The first part considers elastic models of RC wall buildings and responds to the specific objectives 1, 2 and 3. The second part considers non-linear models and responds to the specific objectives 4, 5, and 6. Finally, both parts are used to respond to the last specific objective related to design recommendations.

In the first part of this research, three buildings damaged during the 2010 Chile earthquake are analyzed using detailed elastic models in ETABS. The linear seismic demands of axial load, shear, and moment of selected walls are estimated through response history analyses. The seismic response is evaluated using six seismic records from the 2010 Chile earthquake applied in both horizontal directions of the building simultaneously. The resulting forces obtained from the ETABS models are processed to compute the contribution of coupling elements (beams, slabs, and adjacent walls) to the seismic demands of walls. Additionally, three additional models are considered for each building to analyze the effect of the effective stiffness of the structural elements on the seismic demands. The moment of inertia reduction factors proposed by the ACI 318 (ACI 2019) are used for columns, beams, walls, and slabs, and the diaphragm flexibility is varied. Finally, the responses obtained from the different models are compared to assess the effect of the modeling assumptions on the seismic demands of the walls.

In the second part of this research, a case study building representing a residential structure in Chile is used. Seven different 3D non-linear models of this building were created in the commercial software DIANA (TNO DIANA 2017). The non-linear seismic demands of axial load, shear, and moment of the walls of the considered RC wall building with coupling slabs are estimated by means of static and dynamic analyses. Results from the first four models are used to determine the accuracy of models with non-linear walls and elastic slabs with reduced moment of inertia to

represent the response of the structure considering a full non-linear behavior (i.e. non-linear walls and slabs). Finally, the last three models are used to evaluate the effect of the reinforcement ratio of the coupling slabs on the seismic response of the RC building. The novel aspect of these three models is that the non-linear behavior of the slabs is considered.

## **1.5 Dissertation organization**

The dissertation begins with this introductory chapter, which includes an overview and motivation of the work, objectives, and methodology. Previous experimental and analytical research involving RC wall buildings is summarized in this chapter as part of the literature review of this research.

Chapter 2 is focused on the estimation of the elastic seismic demands of walls in RC buildings. This chapter includes results of linear analyses, which allow quantifying the contribution of the coupling elements to the seismic demands of walls. Additionally, the influence of the assumed stiffness of the structural elements on the predicted seismic demands of walls is evaluated. This chapter is a self-contained paper published in the *Latin American Journal of Solids and Structures* (Ramos and Hube 2020).

Chapter 3 is the second stage of the investigation and involves results from non-linear static analyses used to assess the seismic response of RC wall buildings. This third chapter is focused on evaluating the effect of the non-linear behavior and reinforcement ratio of the slabs on the seismic demands of the walls. Additionally, in this chapter, the accuracy of modeling the slabs elastically with reduced moment of inertia is determined. This part of the research was summarized in a second paper published in the journal *Engineering Structures* (Ramos and Hube 2021).

Chapter 4 is part of the second stage of the investigation, and it includes results from non-linear dynamic analyses. This fourth chapter describes the dynamic response of

the case study building when subjected to three seismic records. The results obtained by the dynamic analyses support the results obtained by the static analysis in chapter 3. Additionally, the results obtained by the dynamic analysis show the important effect of the reinforcement of the slabs on the seismic axial load of the walls.

Finally, Chapter 5 summarizes the conclusions of this work and provides recommendations for future studies.

In addition to the two journal papers composing this document, three conference papers were published in English (Ramos and Hube 2017a; Ramos and Hube 2018) and one in Spanish (Ramos and Hube 2017b). These conference papers address the same topics developed with more detail in this dissertation and are not included in this document.

## 2. CONTRIBUTION OF COUPLING ELEMENTS TO THE LINEAR SEISMIC DEMAND OF WALLS IN RC BUILDINGS

### 2.1 Introduction

Typically, the architectural configurations of RC wall buildings force the connection of structural walls with beams, slabs, and adjacent walls to distribute habitational spaces. Hence, an interaction between the structural elements occurs, and the buildings become a coupled system, which suggests that these buildings must be studied considering a three-dimensional behavior. Indeed, experimental studies have shown that buildings responses are influenced by wall coupling due to slabs and beams (Bertero et al. 1985) and that the 3D interaction between walls and slabs increases the overturning moment capacity (Panagiotou et al. 2011), and the shear demand in walls (Panagiotou et al. 2009).

A recent study by Alarcon et al. (Alarcón et al. 2015) on structural walls of RC buildings damaged during the 2010 Chile earthquake suggests that the behavior of walls was highly influenced by its interaction with slabs, beams, and other walls within the building. Additionally, other researchers (Wallace et al. 2012; Jünemann et al. 2015; Alarcón et al. 2014) have identified the high axial load levels as one of the principal causes of the observed wall damage on RC wall buildings during the 2010 Chile earthquake. Hence, to further understand the behavior of RC walls, it is critical to estimate the seismic axial loads properly and identify how the three-dimensional interaction of the different coupling elements contributes to the seismic demands in such walls.

This chapter quantifies the contribution of coupling elements to the seismic demands of axial load, shear, and moment along walls height in RC buildings and analyses the effects of using different modeling assumptions on the predicted seismic demands in the walls. Three buildings damaged during the 2010 Chile Earthquake are used to

assess the seismic demand in RC walls to achieve these goals. The buildings are analyzed considering their three-dimensional layout, using detailed elastic finite element models constructed in ETABS. The reduction factors for the moments of inertia proposed by ACI 318 (ACI 2019) are used for columns, beams, walls, and slabs, since the yielding of elements is expected before the buildings reach their peak strengths (Englekirk 2003).

The seismic demands are estimated through response history analyses using a set of six Chilean seismic records from the 2010 earthquake, applying the ground motions in both horizontal directions simultaneously. From these analyses, an estimation of the height-wise contributions of coupling elements to the seismic axial load, shear, and moment in eight damaged walls is obtained, identifying the participation of slabs, beams, and adjacent walls.

To analyze the effects of using different modeling assumptions on the seismic demands of the selected walls, three additional models were created and were subjected to the same ground motions as the base model. The first one uses the ACI 318 (ACI 2019) reduction factors for beams, columns, and walls, but a larger factor for slabs. For the second model, gross section properties are considered for the structural elements. Finally, the third additional model is identical to the second one, but it considers a diaphragm with infinite in-plane stiffness, as commonly assumed in engineering practice.

## **2.2 Building description**

Three residential buildings damaged during the 2010 Chile earthquake are considered to assess the seismic demand in RC walls. The three buildings were designed using the Chilean seismic codes that were in force at the time of the 2010 earthquake. These codes were the NCh430 and NCh433 (INN 1996; INN 2008), which incorporated ACI 318 (ACI 1995) seismic provisions except the special boundary elements. Two of these

buildings (CM and AH) are located in Concepción and the third one (SO) is in Santiago. Concepción was the city most affected by the earthquake, and it is located about 60 km southeast of the hypocenter (Boroschek et al. 2012). Santiago is located approximately 450 km north of Concepción (see Figure 2- 1). These buildings experienced moderate to severe damaged, mostly concentrated in RC walls of the basements and the first floor. After the earthquake, the CM building was demolished, and the buildings AH and SO were repaired, those last two buildings remain operational thus far.

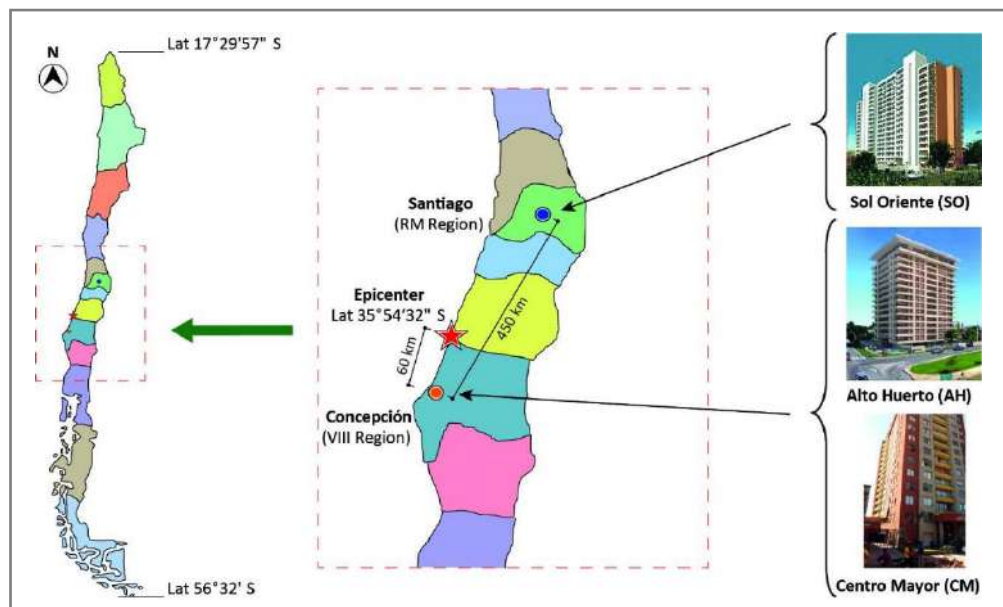


Figure 2- 1: 2010 Chile earthquake hypocenter and location of Santiago and Concepción cities.

General characteristics of the three buildings are summarized in Table II- 1, including the city, the number of stories (above grade and below grade), built year, floor plan area (including basements area), and the soil type used for designing the buildings according to the Chilean code (INN 1996). Soil type II represents a dense gravel or clay with shear wave velocity larger than 400 m/s in the upper 10 m, and soil type III represents a gravel or clay with shear wave velocity lower than 400 m/s (INN 1996).  $A_0$  in Table II- 1 is the effective acceleration according to NCh 433 (INN 1996), which may be interpreted as the peak ground acceleration.  $\bar{\rho}_t$  and  $\bar{\rho}_l$  in Table II- 1 indicate

the average wall densities in transverse and longitudinal direction, respectively. The wall density is defined as the ratio between the wall section area and the floor plan area. Finally,  $T$  is the fundamental period of the building. The fundamental period of each building was estimated using a finite element model considering cracked sections following ACI 318 (ACI 2019). The finite element models are described later.

Table II- 1: General characteristics of RC buildings considered in this investigation

ID building	City	# Stories	Built year	Floor plan area (m <sup>2</sup> )	$\bar{\rho}_t$ (%)	$\bar{\rho}_l$ (%)	Soil type	$A_0$ (g)	$T$ (s)	
CM	Concepción	18+1	2005	13,870	2.44	2.34	III	0.4	1.24	
AH	Concepción	15+2	2009	12,665	2.57	2.39	III	0.4	0.92	
SO	Santiago	18+2	2007	10,190	3.46	3.00	II	0.3	1.33	

The plan layouts of the typical story of the three buildings are shown in Figure 2- 2. The buildings' structural system is composed mainly of RC structural walls to withstand gravity and lateral loads. The typical floor plans of buildings (a) and (c) in Figure 2- 2 are characterized by having longitudinal walls that defines a central corridor and transverse walls that separate building apartments and interior rooms. Transverse walls run from the corridor toward the building exterior creating a topology referred to as "fish bone" (Jünemann et al. 2015) (Figure 2- 2). Most of the walls have a thickness of 20 cm, non-rectangular cross sections and the damaged walls analyzed in this study are highlighted in red in Figure 2- 2. The CM building has 18 stories and one basement, with commercial spaces on the first level. It has slabs 15 cm thick and inverted deep beams 20 cm wide and between 50 to 150 cm depth. The AH building has 15 stories and 2 basements, with slabs of 15 and 20 cm thick, respectively. Beams sections have widths of 20, 30, and 40 cm, and depths that range from 35 to 150 cm. The SO building has 18 stories and two basements, and it is composed of two symmetrical rectangular blocks separated by a construction joint (Figure 2- 2c shows one of these blocks). This latter building has few deep beams of 20 by 75 cm and slabs of 15 cm thick. More

information about these buildings is available elsewhere (Westenenk et al. 2012; Westenenk et al. 2013; Jünemann et al. 2016a).

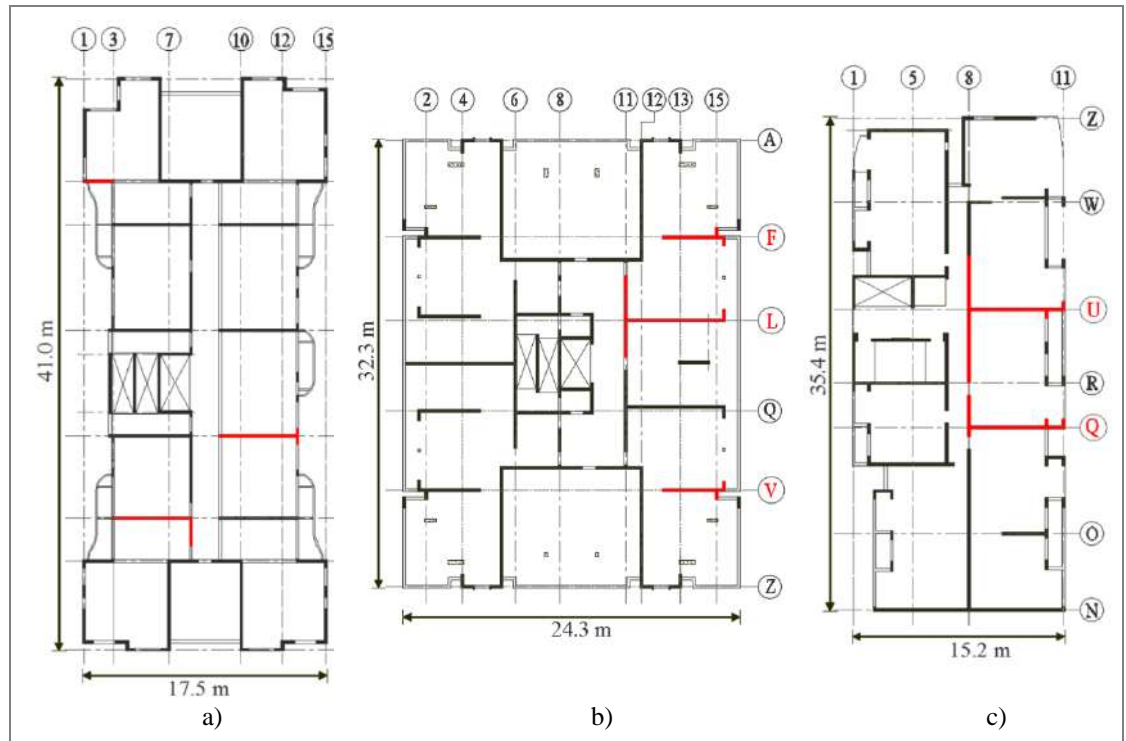


Figure 2- 2: Plan view of typical story of considered buildings: a) CM; b) AH; c) SO. Considered walls in this study are shown in red.

### 2.3 Finite element models and ground motions

The elastic seismic demands of the described buildings were obtained from response history analyses carried out with finite element models developed in ETABS 2010 (Figure 2- 3). Walls and slabs were modeled using 4-node shell elements with a thin plate formulation, which neglects transverse shear deformation (Habibullah 1992). Beams were modeled as frame elements, and the soil-structure interaction was not accounted for. Fixed supports were considered in the base, and the seismic mass was calculated from the dead load and 25% of the live load. The diaphragms were modeled

considering flexural and in-plane stiffness, which are referred to as semi-rigid in ETABS (Habibullah 1992).

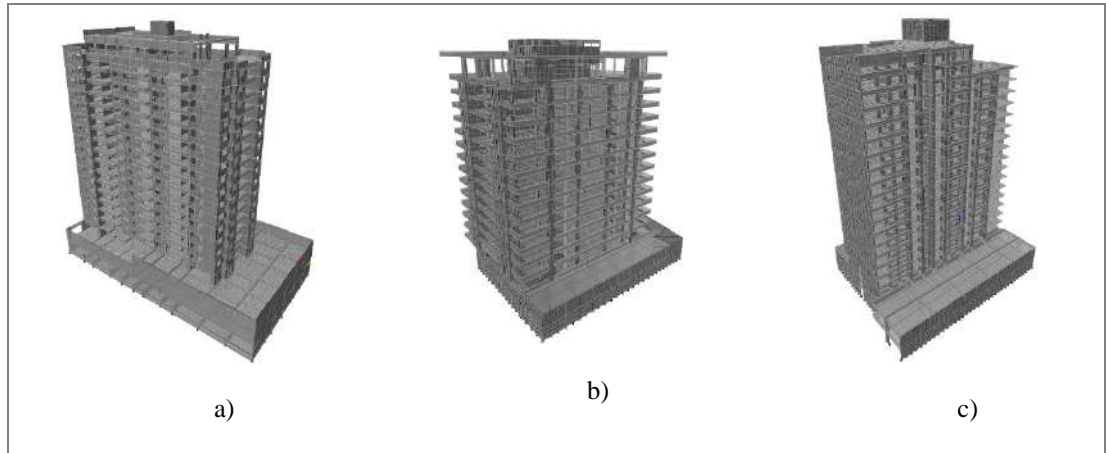


Figure 2- 3: 3D views of the finite element models: a) CM building; b) AH building; c) SO building.

Reduced moments of inertia were used in the models as proposed by ACI 318 (ACI 2019) for factored load analysis. These reduced moments of inertia aim to reflect the degree of cracking and the inelastic action of structural members near or beyond yielding. The moments of inertia used for beams columns and slab were  $0.35I_g$ ,  $0.7I_g$ , and  $0.25I_g$ , respectively, where  $I_g$  is the gross moment of inertia. The moment of inertia used for walls was  $0.5I_g$ , which is an intermediate value between  $0.35I_g$  and  $0.7I_g$  proposed by ACI 318. The moment of inertia of  $0.25I_g$  used for slabs have also been used by previous studies (Ugalde et al. 2019 and Gallardo et al. 2021). The value of  $0.5I_g$  for walls is smaller than the value of  $0.7I_g$  used by (Gallardo et al. 2021) because this latter study considered non-linear behavior of the walls in the first stories and linear behavior with reduced moment of inertia ( $0.7I_g$ ) only in the upper stories. Reduced shear and axial stiffness were not considered for walls as they are not prescribed in the ACI 318. The buildings' fundamental periods calculated with the described assumptions were summarized in Table II- 1.

### 2.3.1 Ground motions

Ground motions for conducting the response history analyses were selected based on buildings' location from the available records of the 2010 Chile earthquake. Buildings located in Concepcion (CM and AH) were subjected to seismic records from the San Pedro (SP), Constitución (CT) and Concepcion (CO) stations (CSN 2019; ONEMI 2019). The seismic records of Santiago Centro (SC), Santiago Peñalolén (SN), and Santiago Puente Alto (SPA) (ONEMI 2019) were used for the SO building located in Santiago. The pseudo-acceleration and displacement response spectrum of the two horizontal components (EW, NS) of the six considered ground motions are shown in Figure 2- 4.

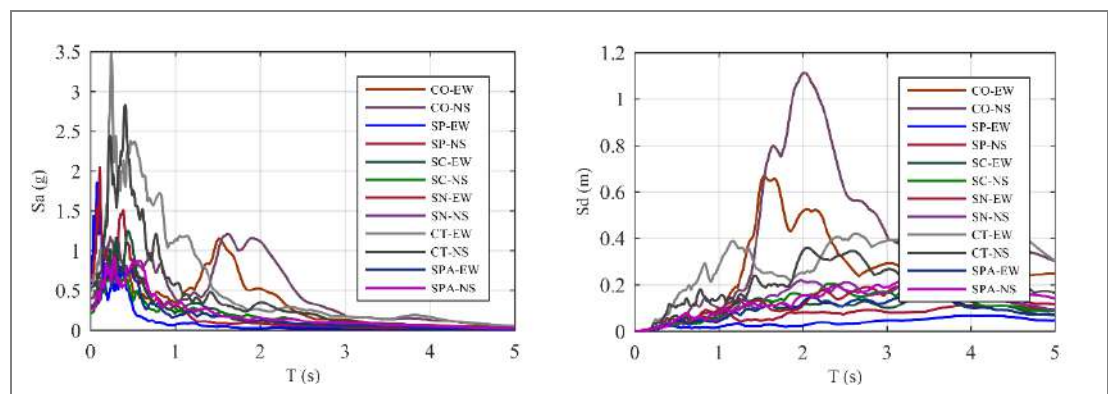


Figure 2- 4: Pseudo-acceleration and displacement response spectrum for selected ground motions (5% damping ratio).

For conducting the response history analyses, both horizontal components of the seismic records were applied simultaneously considering two possible orientations of the ground shaking (i.e., aligning the NS component of a ground motion with the longitudinal direction of the buildings or with the transverse direction of the buildings). To obtain comparable responses between ground motions, seismic records were scaled to a spectral displacement (Sd) of 10 cm at the fundamental period of the buildings. This spectral displacement is about the design displacement according to the current

Chilean code (MINVU 2011) at the average period of the three buildings, for a site characterized by medium stiff soil, and an effective acceleration of 0.3g ( $S_d = 10.19$  cm for an average period of 1.17 s). The horizontal component applied in the transverse direction of the buildings (i.e., the direction of the damaged walls) was considered for obtaining the scaling factor of the seismic records, and the obtained factor was applied to both horizontal components in the model. The spectral displacement at the fundamental periods of the buildings and the scaling factors of each component of the ground motions for buildings located in Concepción and Santiago are summarized in Table II- 2 and Table II- 3, respectively. The tables also show the peak ground acceleration (PGA) of each component of the seismic records without scaling.

Table II- 2: PGA of ground motions, spectral displacements at the fundamental building periods, and scaling factors for the buildings CM and AH located in Concepcion

Ground motions	PGAs (g)	Sd (cm)		Scaling factors	
		CM	AH	CM	AH
CO_EW	0.29	21.21	8.30	0.47	1.21
CO_NS	0.40	17.67	11.19	0.57	0.89
SP_EW	0.58	3.10	1.37	3.22	7.29
SP_NS	0.61	4.33	5.46	2.31	1.83
CT_EW	0.63	35.65	13.69	0.28	0.73
CT_NS	0.54	15.58	22.58	0.64	0.44

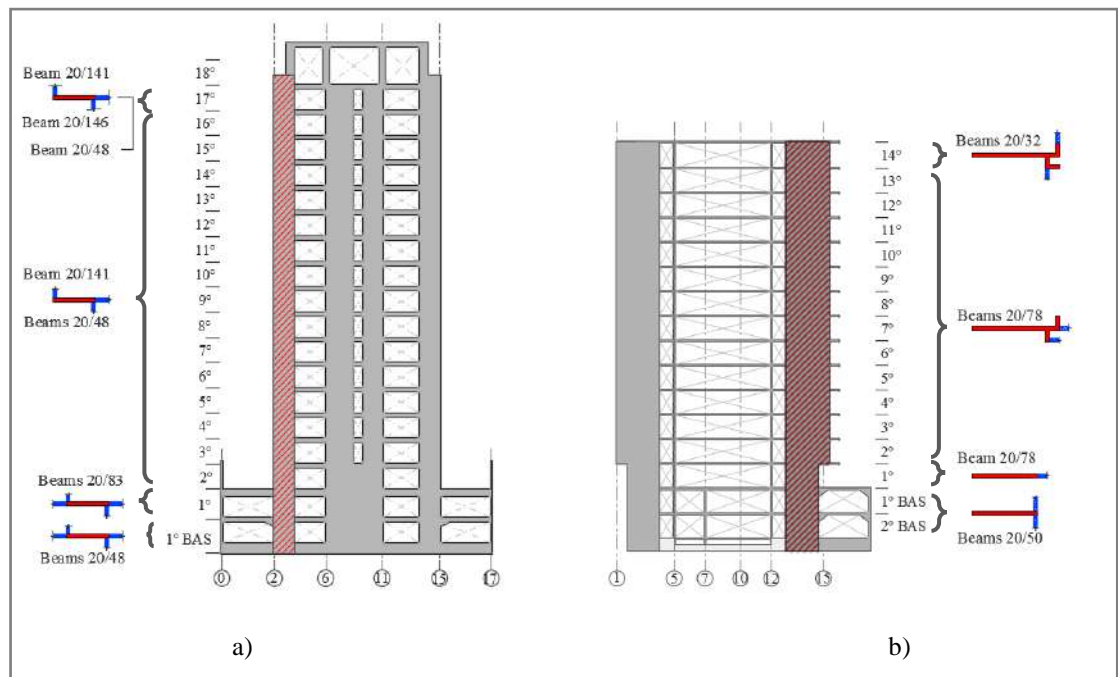
Table II- 3: PGA of ground motions, spectral displacements at the fundamental building periods, and scaling factors for the SO building located in Santiago

Ground motions	PGAs (g)	Sd (cm)	Scaling factors
SC_EW	0.31	13.14	0.76
SC_NS	0.21	9.38	1.07

SN_EW	0.29	10.80	0.93
SN_NS	0.30	13.52	0.74
SPA_EW	0.27	9.40	1.06
SPA_NS	0.27	11.74	0.85

## 2.4 Seismic demand on walls and contribution of coupling elements

The seismic demands of the eight damaged walls highlighted in red in Figure 2- 2 were estimated. In this section, detailed results for one wall in each building are presented: wall in axis E in CM building (E-CM), wall in axis V in AH building (V-AH), and wall in axis U in SO building (U-SO) (See Figure 2- 2). These three walls are highlighted in the elevations of Figure 2- 5, and their thickness is 20 cm. Additionally, Figure 2- 5 shows the variation of the cross-sections of the studied walls along the height of the buildings. The beams attached to the walls are shown in blue, and the dimensions of their cross-sections are specified. Figure 2- 5 clearly shows the complexity of the layout of actual walls in RC buildings.



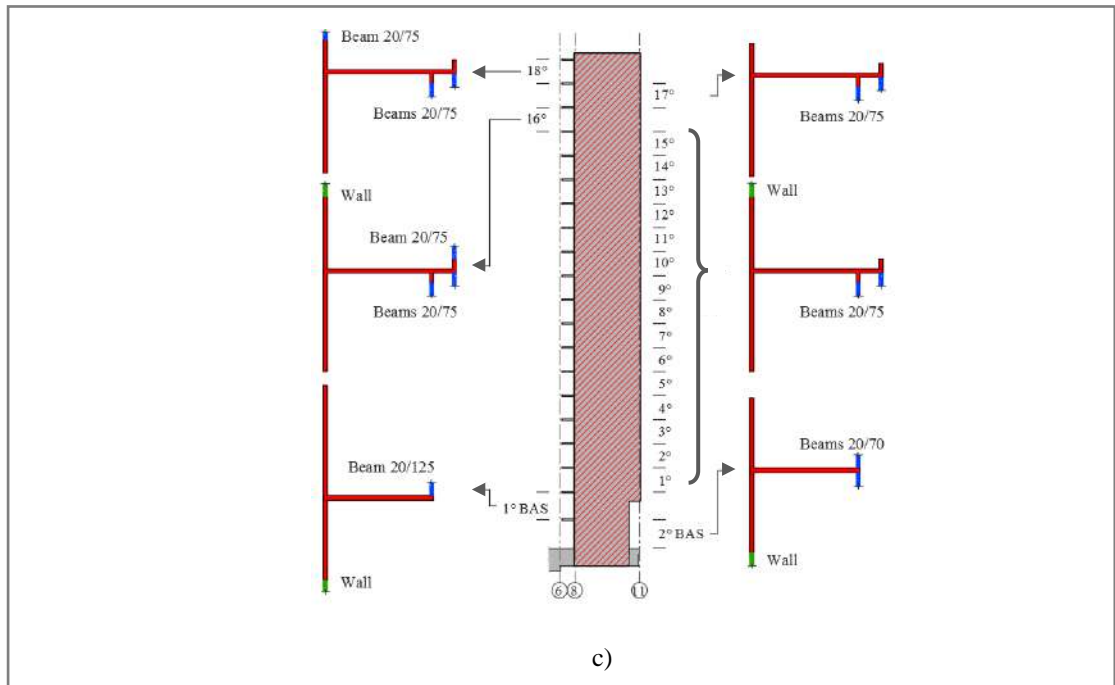


Figure 2- 5: Elevation view and cross-sections of studied walls: a) wall E-CM; b) wall V-AH; and c) wall U-SO.

The wall E-CM (Figure 2- 5a) has a rectangular cross-section along its height, and it is not connected to adjacent walls. The numbers of beams attached to this wall vary along the wall height, as well as the dimensions of the beams. The wall V-AH is flag-shaped as its length increases from the 2<sup>nd</sup> story (Figure 2- 5b). The cross-section of this wall is rectangular from the second basement to the 1<sup>st</sup> story, and it contains flanges at the exterior side of the building in upper stories. The cross-section of wall V-AH is constant from the 2<sup>nd</sup> to the 13<sup>th</sup> story, and the number and cross-sections of connecting beams vary along the wall height.

Finally, the wall U-SO is also a flag-shaped wall as its length increases from the 1<sup>st</sup> story (Figure 2- 5c). For the 1<sup>st</sup> and 2<sup>nd</sup> basement, the wall has a T-shaped cross-section with a 25 cm thickness web, a 20 cm thickness flange. The flange length was defined based on the effective flange width of ACI 318 (ACI 2019). Therefore, the wall's flange is connected to an adjacent wall in these stories, which is shown in green in Figure 2-

5c. Starting from the 1<sup>st</sup> story, the thickness of the web is reduced to 20 cm, and the cross-section has two small flanges at the exterior side of the building. Between the 1<sup>st</sup> and the 16<sup>th</sup> story, the wall is connected to an adjacent wall through the flange, but on the opposite side as the one of the basements stories. For U-SO wall, the number and cross-section of connecting beams also vary along the wall height.

The response history of the seismic demands of axial load ( $P$ ), shear ( $V$ ), and moment ( $M$ ) of the walls was obtained at the top and bottom locations of each story. Response values for  $P$ ,  $V$  and  $M$  at the instant of maximum and minimum roof displacements are analyzed. (Further results are shown for the instant of maximum roof displacement). This instant is considered because the ACI 318 (ACI 2019) and the Chilean code (MINVU 2011) use the roof displacement to determine whether special boundary elements are required in walls.

The piers to compute output forces of walls in ETABS were defined according to the cross-sections shown in red in Figure 2- 5, where a pier is a group of shell elements that are considered as a unity for estimating member forces. Figure 2- 6a shows schematically a wall pier connected to slabs and beams at different stories. The axial load, shear, and moment at the bottom of the pier at  $i$ -th story are  $P_{w,i}^B$ ,  $V_{w,i}^B$ , and  $M_{w,i}^B$ , respectively (Figure 2- 6). The corresponding forces at the top of the pier are  $P_{w,i}^T$ ,  $V_{w,i}^T$  and  $M_{w,i}^T$ . These forces are obtained from the pier force output table of ETABS.

The axial force, shear, and moment at the bottom of a pier of the story  $i+1$  are different than those at the top of the pier of the  $i$ -th story. The forces transferred by the slab and beams to the pier at this level generate these differences. Therefore, the relationship of axial load, shear, and moment between adjacent stories can be expressed as:

$$P_{w,i}^T = P_{w,i+1}^B + P_{b,i} + P_{s,i} \quad (2.1)$$

$$V_{w,i}^T = V_{w,i+1}^B + V_{b,i} + V_{s,i} \quad (2.2)$$

$$M_{w,i}^T = M_{w,i+1}^B + M_{b,i} + M_{s,i} \quad (2.3)$$

Where  $P_{b,i}$ ,  $V_{b,i}$ , and  $M_{b,i}$  are the axial load, shear, and moment transferred by the beams of the story  $i$  (Figure 2- 6a), respectively, and  $P_{s,i}$ ,  $V_{s,i}$ , and  $M_{s,i}$  are those transferred by the slab of the same story. From the output forces of the beam elements in ETABS (e.g., shear in beam is the transferred axial load to the pier) is possible to obtain the forces transferred by the beams. Finally, the contribution of the slabs to the axial load, shear, and moment, is obtained by solving equations (2.1), (2.2), and (2.3) for  $P_{s,i}$ ,  $V_{s,i}$ , and  $M_{s,i}$ , respectively.

The axial load and shear at the top and bottom of a pier of the  $i$ -th story are identical when the pier is not connected to adjacent walls, and the moment varies along the pier height because of the shear. Therefore, the shear generated by the beams and slab connected at the top of a pier generates moments at the bottom of the pier. These contributions were considered in this study.

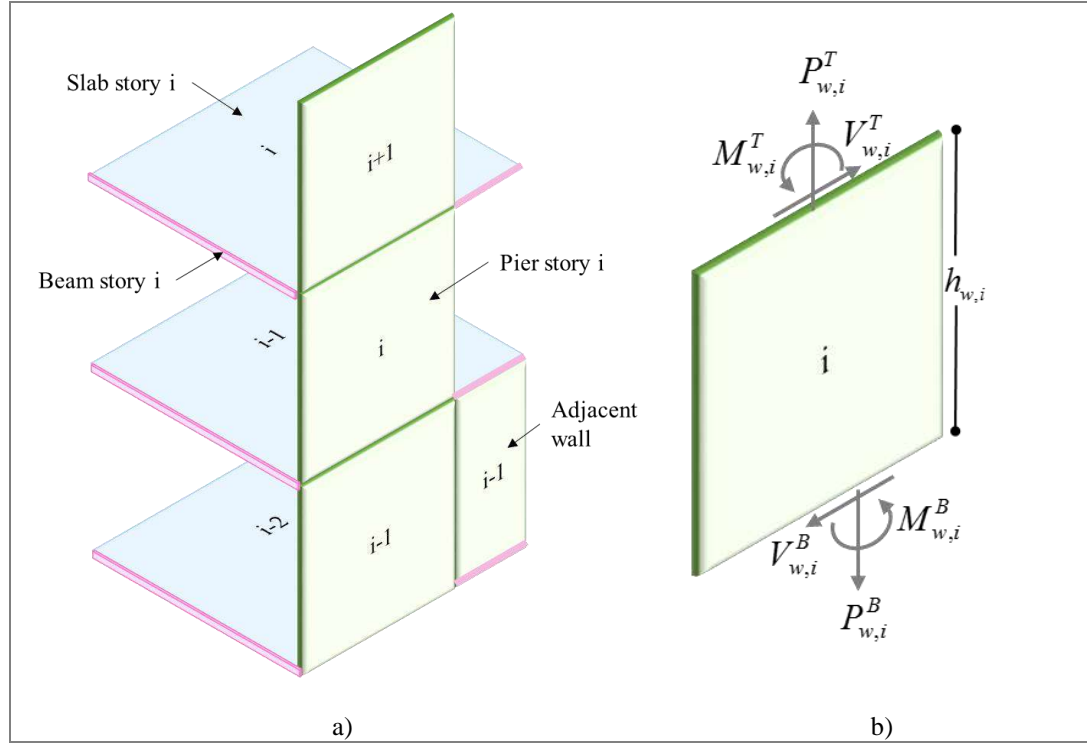


Figure 2- 6: Representative a) three-dimensional layout of a pier, slabs, and beams and b) pier forces at the i-th story.

When a pier is connected to an adjacent wall (e.g., wall of story i-1 in Figure 2- 6a), the axial load and shear at the top and bottom of the pier of the i-th story are different.

$$P_{a,i} = P_{w,i}^B - P_{w,i}^T \quad (2.4)$$

$$V_{a,i} = V_{w,i}^B - V_{w,i}^T \quad (2.5)$$

The differences  $P_{a,i}$  and  $V_{a,i}$  correspond to the contribution of the adjacent wall to the axial load and shear of the pier at this story, respectively. Finally, to obtain the contribution of the adjacent wall to the moment ( $M_{a,i}$ ) of the pier, the moment

generated by shear of the beams and slab needs to be subtracted as follows, where  $h_{w,i}$  is the height of the pier at the  $i$ -th story.

$$M_{a,i} = M_{w,i}^B - M_{w,i}^T - (V_{b,i} + V_{s,i}) \cdot h_{w,i} \quad (2.6)$$

The seismic demands of axial load, shear, and moment along the normalized building height of walls E-CM, V-AH, and U-SO, at the instant of maximum roof displacement are shown in Figure 2- 7. Notice that the gravitational forces are not considered in the figure. The figure shows the results from the ground motion that induced the maximum compressive axial load in the walls (i.e., negative axial load in this study) of each building. Additionally, the figure shows the contribution of the slabs, beams, and adjacent walls to the seismic demands of the studied walls. These contributions were obtained with the previously described procedure. The results shown in Figure 2- 7 correspond to the SP seismic record applied with the NS and EW components in the direction of the damaged walls for the CM and AH building, respectively. For the SO building, the results correspond to the SC seismic record applied with the NS component in the direction of the damaged walls. The horizontal dashed line indicates the ground level (G.L.).

The maximum compressive seismic axial load predicted for the wall E-CM is 2,945 kN (total load in Figure 2- 7a), representing an axial load ratio  $ALR = P/f'_c A_g$  of 0.27, where  $f'_c$  is the specified concrete compressive strength and  $A_g$  is the gross cross-section of the wall. The maximum seismic axial loads predicted for the walls V-AH and U-SO are 5,119 kN and 5,664 kN, which correspond to ALRs of 0.30 and 0.07, respectively. These maximum values are predicted at the first story for the three walls since the axial load decreases at the basements stories due to load transfer from the core walls to the basement perimeter walls.

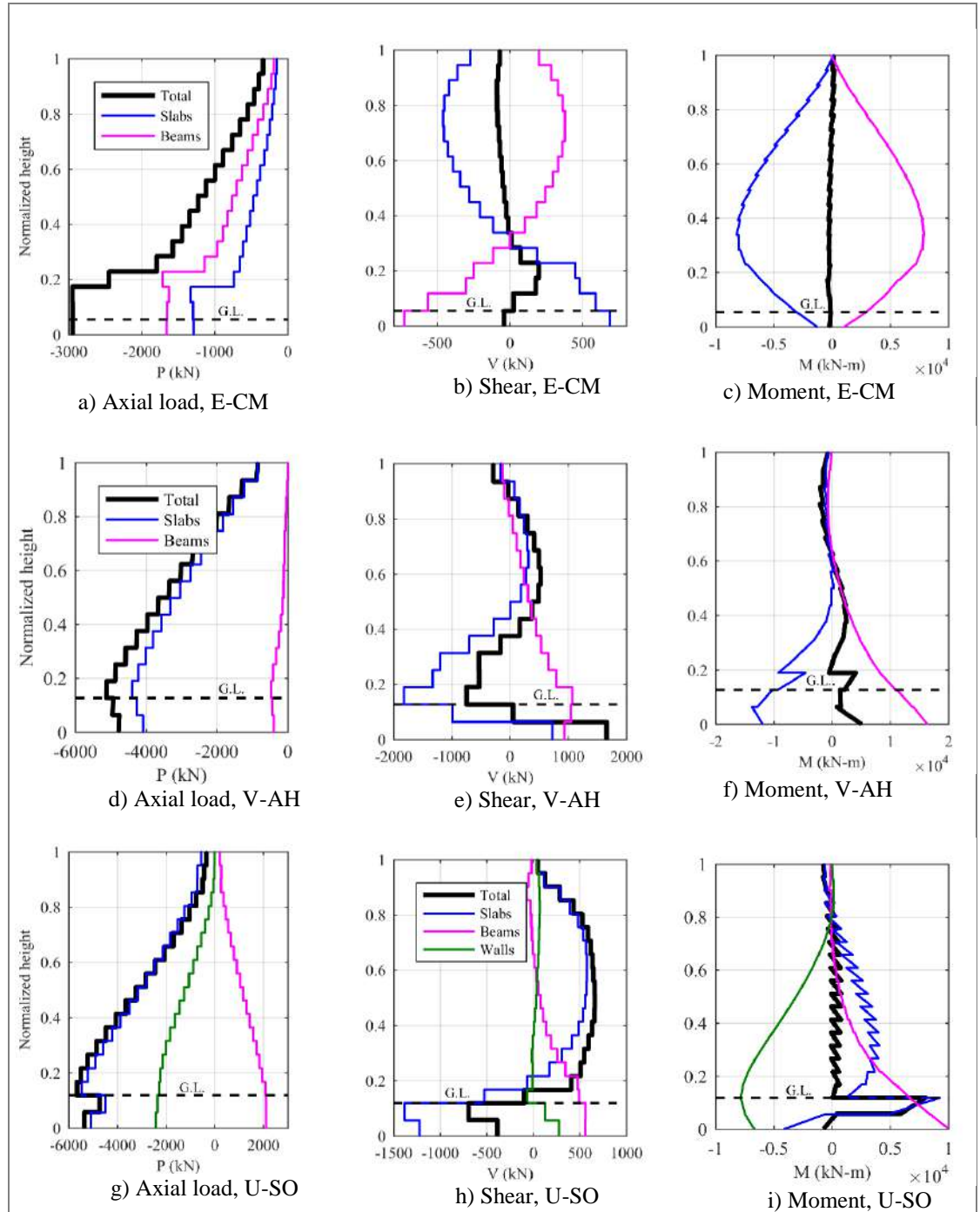


Figure 2- 7: Seismic contribution of coupling elements to: a) P of E-CM wall; b) V of E-CM wall; c) M of E-CM wall; d) P of V-AH wall; e) V of V-AH wall; f) M of V-AH wall; g) P of U-SO wall; h) V of U-SO wall and i) M of U-SO wall. (G.L. corresponds to the ground level).

The different contribution of slabs, beams, and adjacent walls to the seismic axial loads of the studied walls (Figure 2- 7) is related to the location of such walls within the floor plan of the buildings and the connection with adjacent structural elements. For wall V-AH, the connected beams in the typical story (Figure 2- 5b) are gravitational exterior beams that do not carry significant seismic forces. Therefore, the largest contribution of the slabs in V-AH wall is related to the short distance between this wall and the long transverse wall on axis 12 (Figure 2- 2b), which induces shear forces in the slabs. For the wall E-CM, coupling beams of significant dimensions are connected to nearby walls, and as expected, the beams in the elevation of the wall (axis E) are the ones that contribute the most. In consequence, the contribution of beams for the seismic axial load of wall E-CM is larger than the contribution of slabs (Figure 2- 7a). Finally, the opposite axial loads induced by beams and adjacent walls in wall U-SO are explained by the opposite locations of the beams and adjacent walls with respect to the web of this wall.

Regarding the shear demand at the instant of maximum roof displacement, Figure 2- 7 shows that the sign of the total shears changes at ground level for the three studied walls. This change is attributed to the back-stay effect induced by the basement stories (Moehle 2015). Additionally, walls E-CM and V-AH show an additional sign change of the shear at a normalized height of 0.28 and 0.38, respectively. For the three walls, the maximum shears are located at the bottom (in the first 20% of the height of the building), but they occur in different stories. For the wall E-CM, the maximum shear of 198 kN occurs at the third story and is equivalent to a shear stress coefficient  $\tau = 0.09$ . Where  $\tau = V/(\sqrt{f'_c}A_v)$ ,  $A_v$  is the effective shear area of the wall in  $\text{mm}^2$  and  $f'_c$  is in MPa. For the walls V-AH and U-SO, a maximum shear of 1,659 kN ( $\tau = 0.29$ ) and 885 kN ( $\tau = 0.13$ ) are predicted at the second and first basement, respectively.

Figure 2- 7 e and Figure 2- 7 h show that the total shear demand in walls V-AH and U-SO is mainly attributed to the contribution of slabs. For such walls, the beams help to

reduce the total shear demand in the lower stories. For wall E-CM, coupling beams and slabs exert opposite contributions of similar magnitudes to the shear (Figure 2- 7b), which results in a reduced total shear along the wall height. Finally, Figure 2- 7 shows that the contribution of the slabs to the total shear at the basement stories is significant in walls V-AH and U-SO because the slabs transfer significant shear forces to the perimeter walls.

Regarding the moment demand, Figure 2- 7c shows that in the E-CM wall the total maximum moment (-397 kN-m) is negligible compared to the moments transferred by the beams and the slabs. For the wall V-AH (Figure 2- 7f), a maximum moment of 5,091 kN-m occurs at the wall base, and two sign changes are observed in the diagram, at 23% and 60% of the wall height. Finally, for the wall U-SO, a maximum moment of 8,047 kN-m is predicted at the ground level, and several sign changes are observed along the wall height.

The contribution of the coupling elements to the total seismic moment for wall E-CM follows the same trend observed for the shear diagram, where beams and slabs exert opposite contributions of similar magnitudes. Similar behavior is observed for the moment diagram in wall V-AH, where beams and slabs exert opposite contributions in the lower stories. Finally, for the wall U-SO, the beams and slabs exert a joint contribution that is similar and opposite to the contribution of the adjacent walls. This behavior is observed above the ground level, whereas in the first basement, the moment transferred by the slab to the wall U-SO increases significantly.

Figure 2- 8 shows the contribution of the coupling elements to the gravitational axial load of the studied walls. The figure confirms that the beams connected to the wall V-AH are gravitational beams because of the large contribution to the gravitational axial load in the wall. For the wall E-CM the figure shows that the contribution of the coupling beams to the gravitational axial load is similar than the contribution of the slabs. Finally, the figure shows for the wall U-SO that the gravitational axial load is

mostly generated by the slabs and adjacent walls. The contribution of the beams to the axial load of the wall U-SO is negligible.

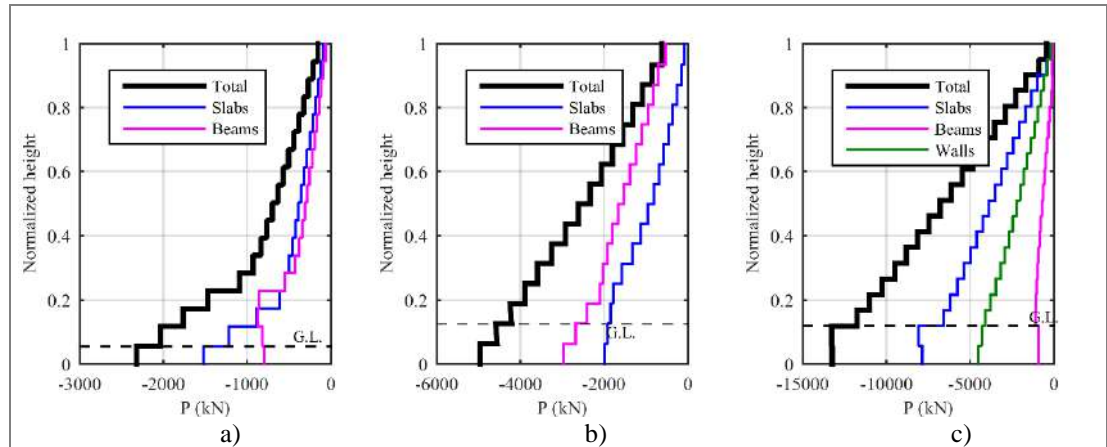


Figure 2- 8: Contribution of the coupling elements to the gravitational axial load in: a) E-CM wall; b) V-AH wall, and c) U-SO wall (G.L. correspond to the ground level).

The envelopes of the compressive seismic axial load demands for walls E-CM, V-AH, and U-SO, for the three seismic records and the two possible orientations of the ground shaking (six seismic cases) are shown in Figure 2- 9. An average seismic axial load of 5,065 kN, 4,602 kN, and 6,240 kN, are predicted in the first story for walls E-CM, V-AH, and U-SO, respectively. These forces correspond to ALRs of 0.46, 0.27, and 0.07, respectively and the largest ALR of 0.83 is predicted for wall E-CM. These large values demonstrate that coupling elements generate significant seismic axial load demands in the studied RC walls. Moreover, even though the ground motions were scaled to the same spectral displacement, significant variation of the axial loads envelopes are predicted by different ground motions, where the coefficient of variation of the ALRs at the first stories are 0.47, 0.46, and 0.33 for walls E-CM, V-AH, and U-SO, respectively. These large variations are influenced by the second component of the seismic records since reduced variations of ALRs were obtained when analyzing the buildings with only one ground motion component.

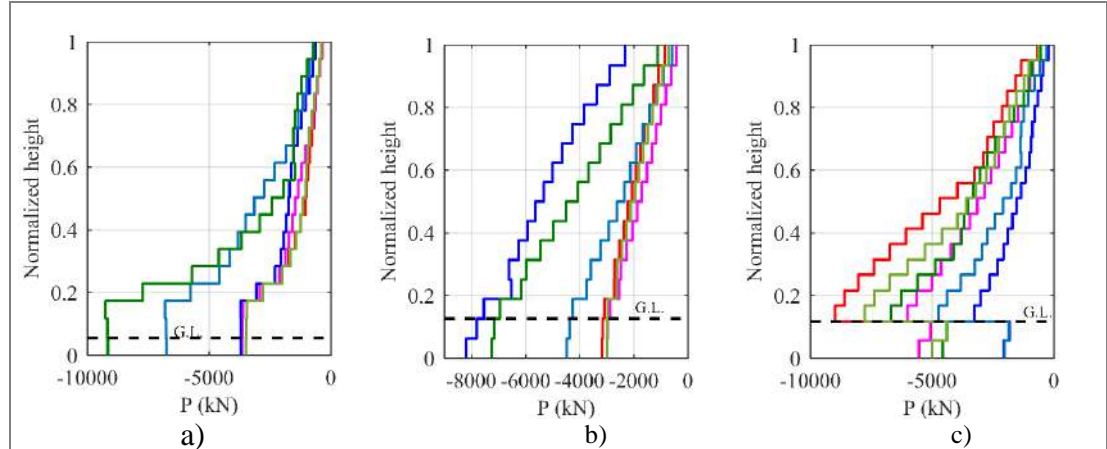


Figure 2- 9: Compressive axial load demand envelopes for the three seismic records and two possible orientations: a) wall E-CM; b) V-AH; and c) U-SO.

The envelopes of the seismic shear demands for the walls E-CM, V-AH, and U-SO for the three seismic records and the two possible orientations of the ground shaking are shown in Figure 2- 10. The maximum shear predicted by different ground motions is located at different heights for the three walls, and abrupt changes are observed at the first story and ground level due to the back-stay effect. Additionally, the shear envelopes for different ground motions vary significantly along the height of the three walls. Consequently, the estimation of the seismic shear demands for designing these coupled walls is complex, even when an elastic analysis is considered.

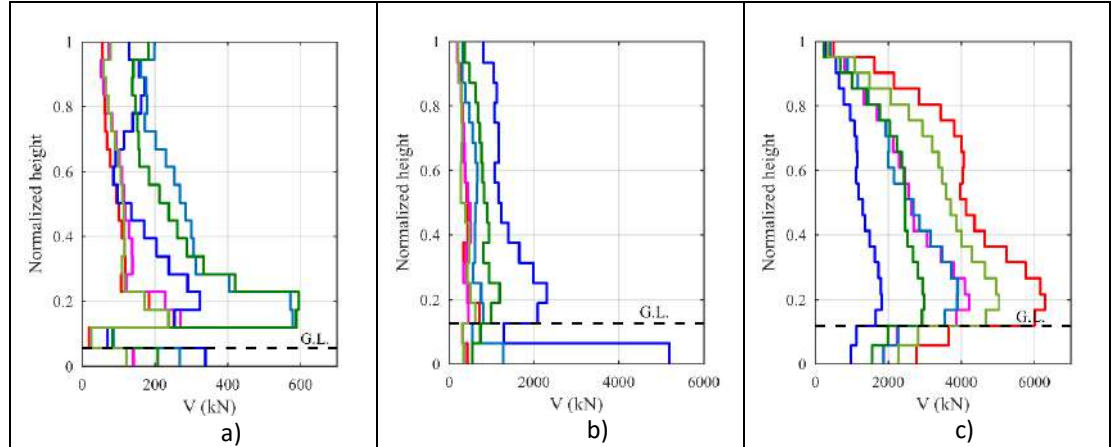


Figure 2- 10: Shear demand envelopes for the three seismic records and two possible orientations: a) wall E-CM; b) V-AH; and c) U-SO.

The envelopes of the seismic moment demand of the three studied walls are shown in Figure 2- 11, for the same six seismic cases considered in Figure 2- 9 and Figure 2- 10. Since the obtained moment diagrams envelopes were relatively symmetric for the three walls, Figure 2- 11 shows only the envelope of the negative moments. The figure shows that the moment profiles of the studied walls have irregular shapes and are different than common profiles observed in cantilever walls (Pugh et al. 2017; Priestley and Amaris 2003; Panagiotou and Restrepo 2009) and in coupled walls through coupling beams (Paulay 1986). Additionally, Figure 2- 11 shows that the maximum moment occurs at different levels and that abrupt changes in the moment diagram are observed for the three walls at the lower stories.

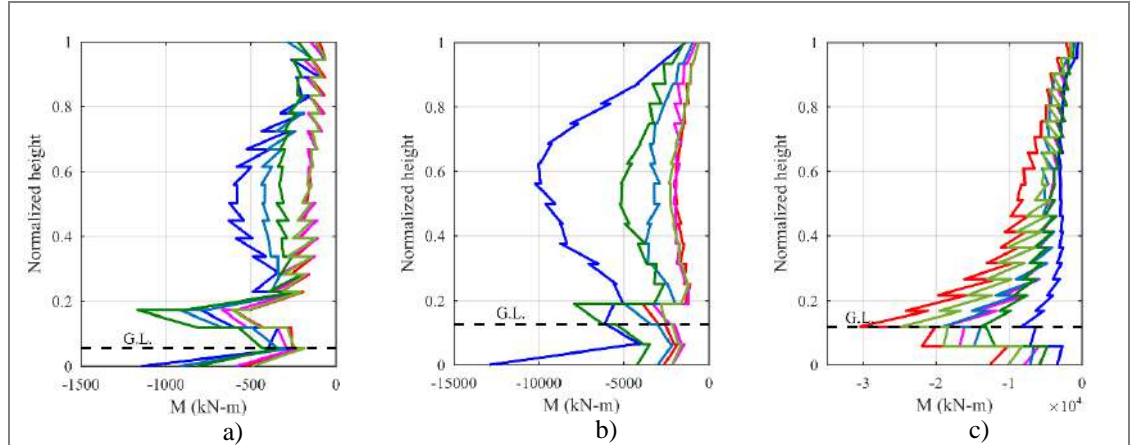


Figure 2- 11: Moment demand envelopes for the three seismic records and two possible orientations: a) wall E-CM; b) V-AH; and c) U-SO.

The contributions of coupling elements to the seismic axial load demands at the first story for the eight damaged walls highlighted in Figure 2- 2 are shown in Figure 2- 12. The median contributions (in percentage) of slabs, beams, and adjacent walls for the six seismic cases at the instants of maximum roof displacement inducing compression and tension forces are shown with bars in Figure 2- 12a) and Figure 2- 12b), respectively.

For walls in the AH and SO buildings, the slabs have the largest contribution to the seismic axial load for both compressive and tensile forces, with contributions that range between 90% and 160%, according to the figure. The cases with contributions over 100% mean that beams exert an opposite effect. For these walls, the contribution of beams is relatively small. For wall U-SO, the contribution of adjacent walls is larger for compressive forces (40% contribution) than for tensile forces (-27% contribution, i.e., the adjacent walls induce compressive forces when the wall is in tension). Figure 2- 12 also shows that the contributions of coupling beams to the axial load demand in walls of CM building are larger than those in walls of AH and SO buildings. In particular, the beams contribution of 57% and 69% to the compressive seismic axial loads of walls E-CM and K-CM, respectively, exceeds the contributions from the slabs.

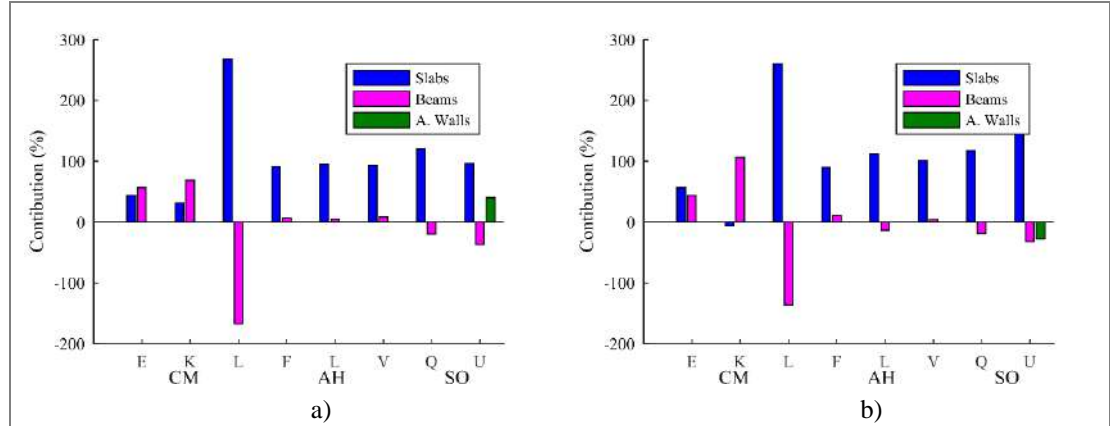


Figure 2- 12: Median contribution of coupling elements to the maximum seismic axial load of walls at the first story for compression (a) and tension (b).

Figure 2- 13a) and Figure 2- 13b) show boxplots of the ALRs obtained from the compression and tension envelopes of the six seismic cases (without scaling), respectively. The compression ALRs in Figure 2- 13a) are shown with positive values. Previous results (Figure 2- 7 and Figure 2- 9 to Figure 2- 12) were shown for scaled ground motion that resulted in the largest compression force. Figure 2- 13 shows that significant seismic ALRs are predicted for the studied walls for both compression and tension cases. Additionally, a large variation of the seismic compression ALR is predicted, with a minimum ratio of 0.05 for the wall Q-SO and a maximum ratio of 1.30 for the wall E-CM. The largest median ALR of 0.65 is obtained for wall E-CM for both compression and tension cases. For walls in the AH building (F-AH, L-AH, and V-AH), the median ALRs for compression and tension cases are about 0.16, while for walls in the SO building (U-SO and Q-SO) the media ALRs are about 0.08.

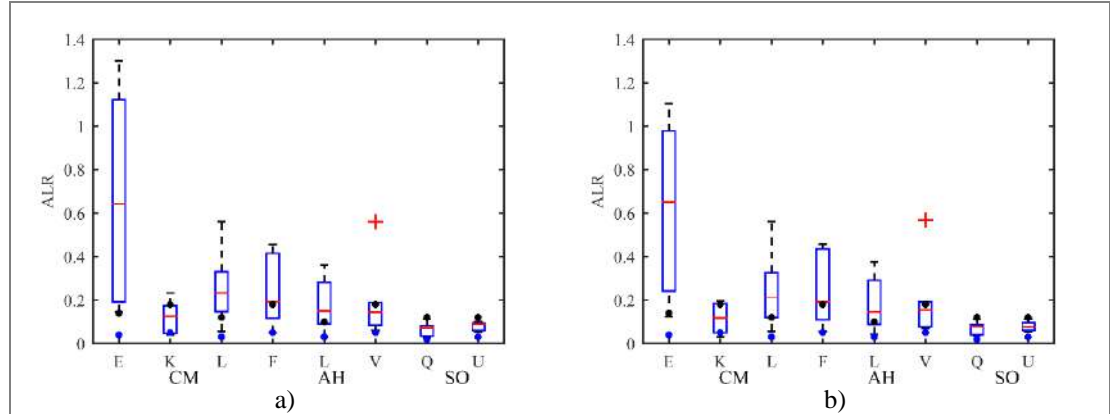


Figure 2- 13: Seismic ALRs of eight walls at the first story in: a) compression (shown with positive values) and b) tension.

Figure 2- 13a) also shows the ALRs of the selected walls for dead and live loads with black and blue dots, respectively. The ALRs for dead and live loads vary from 0.10 to 0.18 and from 0.02 to 0.05, respectively. By comparing the dead ALRs with the compressive seismic ALRs, it is concluded that the median seismic ALRs are larger than the dead ALRs for four of the eight walls (Figure 2- 13a). Additionally, the tensile seismic ALRs for these walls are larger than the gravitational (dead compressive) ALRs, which implies that tension forces are expected to develop at the first story of such walls.

## 2.5 Influence of the modeling assumptions

This section describes the effect of the modeling assumptions on the seismic demands of the studied walls of the three buildings. The results provided in the previous section were obtained with models where the reduced moments of inertia proposed by ACI 318 (ACI 2019) were used. In order to assess the effect of the effective stiffness of the structural elements and the diaphragm flexibility, three additional modeling assumptions are considered for each building (Table II- 4). Model SR1 corresponds to the one used in previous sections (i.e., with a semi-rigid diaphragm in ETABS and

effective stiffness of the elements). Model SR2 is similar to model SR1 but with a larger moment of inertia for slabs to simulate the behavior of less cracked slabs. Model SR3 is similar to model SR1 but considers the gross moment of inertia for all the structural elements. Finally, Model R3 is identical to model SR3, but considers a rigid diaphragm (i.e., infinite in-plane stiffness). This latter model is commonly observed in engineering practice in Chile and worldwide.

Table II- 4: Modelling assumptions considered for each building

Model	Diaphragm	Moment of Inertia			
		Beams	Columns	Walls	Slabs
SR1	Semi-rigid	$0.35 I_g$	$0.70 I_g$	$0.50 I_g$	$0.25 I_g$
SR2	Semi-rigid	$0.35 I_g$	$0.70 I_g$	$0.50 I_g$	$0.40 I_g$
SR3	Semi-rigid	$I_g$	$I_g$	$I_g$	$I_g$
R3	Rigid	$I_g$	$I_g$	$I_g$	$I_g$

The fundamental periods of the analyzed buildings obtained with the four modeling assumptions are summarized in Table II- 5. The fundamental periods with less cracked slabs of models SR2 are on average 4% smaller than those in models SR1. When gross sections are used for the structural elements (model SR3), the fundamental period decreases by 33% compared to model SR1. Finally, if a rigid diaphragm is also considered (model R3), the fundamental period decreases by 35% compared to model SR1. It is important to note that the periods obtained for the R3 models are equivalent to those obtained by previous studies (Westenank et al. 2013; Jünemann et al. 2016a). The in-plane stiffness of the diaphragm has a minimal effect in the fundamental period of the studied buildings since the periods of models R3 are about 3% smaller than those of models SR3. The differences obtained in these latter cases are smaller than those reported by Chacón et al. (2017) for free-plan RC buildings modeled with rigid or flexible diaphragms.

Table II- 5: Fundamental periods of the three buildings with the four modelling assumptions

Model	T (s)		
	CM	AH	SO
SR1	1.242	0.922	1.332
SR2	1.204	0.892	1.274
SR3	0.834	0.628	0.882
R3	0.814	0.603	0.865

The maximum roof drift ratios predicted for the three buildings, with the four modeling assumptions and the considered seismic cases, are shown in Table II- 6. The comparison between the roof drift ratios obtained with model SR1 and SR2 shows that the predicted values using less cracked slabs (SR2 model) are on average 96% of the obtained with the SR1 model. When gross sections are considered (model R3 and SR3), the obtained roof drift ratios are 20% and 17% lower than the obtained with model SR1, respectively. Additionally, a comparison between model SR3 and R3 shows that the in-plane diaphragm stiffness has a negligible influence on the roof drift ratio since values 4% larger are obtained from the SR3 model. The smaller displacements obtained are attributed to the smaller spectral displacements which are at the smaller periods (Figure 2- 2).

Table II- 6: Maximum roof drift ratio (%) predicted for each building for the six ground motions

ID building	Height (cm)	Model	CO		SP		CT	
			E1	E2	E1	E2	E1	E2
CM	4,715	SR1	0.32	0.32	0.36	0.37	0.35	0.34
		SR2	0.31	0.29	0.41	0.36	0.29	0.35
		SR3	0.26	0.12	0.47	0.18	0.35	0.26
		R3	0.25	0.12	0.48	0.18	0.34	0.26
AH	4,107	SR1	0.36	0.35	0.37	0.37	0.60	0.23
		SR2	0.36	0.38	0.36	0.36	0.56	0.21
		SR	0.18	0.25	0.37	0.42	0.49	0.22
		R3	0.17	0.22	0.39	0.37	0.45	0.21
SO	5,064		SC		SN		SPA	
		SR1	0.32	0.31	0.05	0.12	0.30	0.27
		SR2	0.33	0.29	0.05	0.11	0.23	0.24
		SR3	0.20	0.14	0.10	0.07	0.18	0.16
		R3	0.19	0.15	0.10	0.07	0.16	0.16

The seismic demand of axial load, shear, and moment along the building height for walls E-CM, V-AH, and U-SO, considering the four modeling assumptions (SR1, SR2, SR3, and R3), are shown in Figure 2- 14. The figure shows the seismic demands at the instant of maximum roof displacement for the same seismic cases considered in Figure 2- 7 (i.e., one ground motion for each wall-building that induced the maximum compressive axial load in the walls).

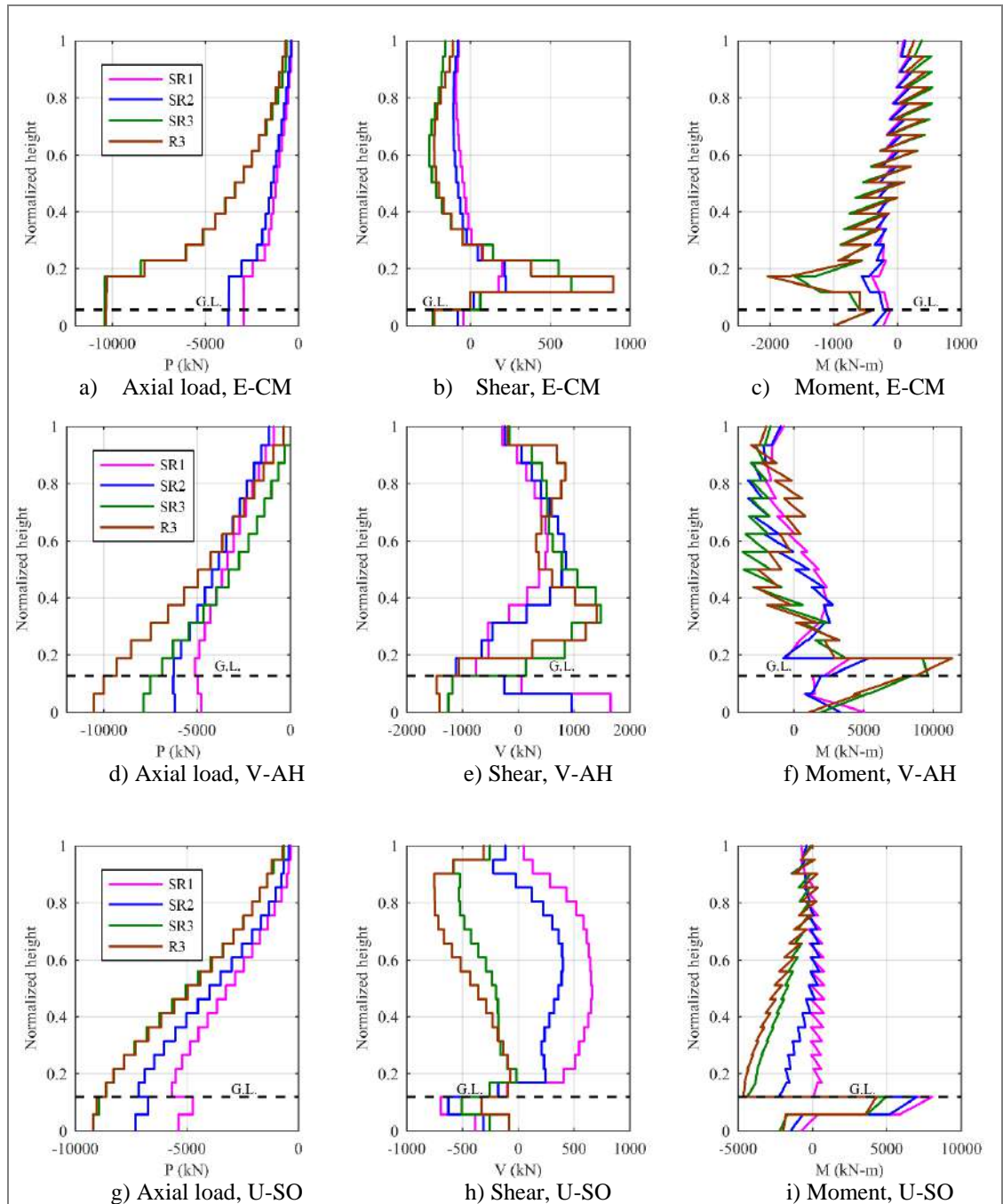


Figure 2- 14: Seismic demand for four modeling assumptions: a) P of E-CM wall; b) V of E-CM wall; c) M of E-CM wall; d) P of V-AH wall; e) V of V-AH wall; f) M of V-AH wall; g) P of U-SO wall; h) V of U-SO wall and i) M of U-SO wall. (GL corresponds to the ground level).

The comparison of the maximum axial load demands for the three walls in Figure 2-14 shows that those predicted with the SR2 model are on average 26% larger than those of model SR1. That supports the idea that the slab stiffness exerts a tangible influence on the prediction of seismic axial load demands of RC walls. When gross sections are considered (model R3 and SR3), the seismic axial loads increase on average by 2.2 times for the model SR3 and 2.4 times for the model R3, compared to the model SR1. Therefore, the assumed stiffness of structural members plays a major role in the prediction of the axial load demands. Finally, a comparison between the models SR3 and R3 shows that the diaphragm stiffness has a notable influence on the axial load demand only for the wall V-AH, since the maximum axial load for the model R3 is 10,560 kN while for the model SR3 is 7,884 kN. For the other two walls, the assumed in-plane stiffness of the diaphragm in model R3 has a negligible influence on the axial load demands of this wall.

The modeling assumption also influences the seismic shear demand. Comparing the SR1 and SR2 models, Figure 2-14 shows that the slab stiffness has a small effect on the estimation of the shear demand for the wall E-CM, whereas it has a larger effect on the estimation for the walls V-AH and U-SO. When gross sections are considered (R3 and SR3), the shear demands for all three walls are significantly different from those of the model SR1. Therefore, the assumed stiffness of structural members exerts an important influence on the prediction of the shear demand. In particular, for the wall V-AH, the back-stay effect and sign changes are more evident in the models SR3 and R3 than in the model SR1. When models with gross stiffness (R3 and SR3) are compared, Figure 2-14 shows that the diaphragm stiffness influences both the magnitude and shape of the shear diagram. In particular, it is observed that for the wall V-AH the shear diagram of the model R3 model has one sign change, whereas that of the model SR3 has three sign changes. Additionally, for the wall E-CM, the maximum predicted shear with the model SR3 is 635 kN, while with the model R3 is 897 kN. The results also show that the location of the maximum shear stress at the wall height is not consistent since they are located in different stories in each wall.

The seismic moment diagrams in Figure 2- 14 show that when less cracked slabs are assumed (model SR2), the shapes and maximum predicted values vary slightly (compared to model SR1), except for the wall U-SO, where differences are observed between 10% and 30% of the building height. The bending moment values and shapes predicted by models SR3 and R3 are significantly different from those predicted by the SR1 model. Particularly for the wall V-AH, the diagram has a double curvature that is more evident for the model SR3 than for the model SR1. That suggests that the stiffness of structural members has an important effect on the predicted bending moment profiles. The comparison between the bending moments predicted with the model SR3 and R3 shows that the diaphragm stiffness has an important influence both in the sign changes as well as in the magnitudes of the moment. The former can be appreciated for the wall V-AH, where a double curvature profile is observed for model SR3 and a triple curvature for model R3. The latter can be observed in the U-SO wall, whose maximum moments occur at the ground level with a different sign, but their magnitudes (in the positive and negative direction) are 4,953 kN-m and 4,308 kN-m, for the models R3 and SR3, respectively.

Table II- 7 gives additional information about the impact of the modelling assumptions on the predicted maximum seismic axial load of the damaged walls of the three buildings Figure 2- 2. The table summarized the average (median) axial load ratios predicted considering all seismic cases and the four modeling assumptions at the instant of maximum roof displacement. The table also includes information about the cross-section area ( $A_g$ ) of the first story (considered the critical story in the three buildings) and the ALR for dead load (D) and live load (L). The ALR for dead loads varies from 0.10 to 0.18 and de ALR for seismic loads varies from 0.04 and 0.44. The results in Table II- 7 show a median difference of 4% between the seismic ALR predicted with the R3 and SR3 models obtaining the highest values with the SR3 model on most walls. When the effective moments of the inertia of the elements is included in the model (SR1 model), the predicted seismic ALRs are 55% lower than that predicted with the SR3 model.

Table II- 7: Axial Loads Ratios for all selected walls in the three buildings.

ID building	Wall	Ag (m <sup>2</sup> )	D	L	SR1	SR2	SR3	R3
CM	E	0.44	0.14	0.04	0.29	0.27	0.41	0.38
	K	1.24	0.18	0.05	0.06	0.08	0.12	0.12
	L	1.15	0.12	0.03	0.07	0.05	0.10	0.08
AH	F	0.68	0.18	0.05	0.19	0.20	0.44	0.42
	L	2.36	0.10	0.03	0.15	0.14	0.31	0.30
	V	0.68	0.18	0.05	0.23	0.21	0.43	0.44
SO	Q	2.14	0.12	0.02	0.06	0.07	0.09	0.09
	U	3.36	0.12	0.03	0.04	0.06	0.09	0.09

Table II- 7 shows that, regardless of the modeling assumption, the axial load ratios, at the first story, that result from the contributions of un-factored dead, live and seismic loads shown in (D+L+E) exceed 0.35 in wall E from CM building and in walls F and V in AH building. The largest value is predicted for F-AH wall with the SR2 model. According to the table, the resulting axial load ratios (un-factored sum of D+L+E) of the K and L wall in CM building are smaller than the 0.35 limited. The ratio of 0.35 was imposed in DS60 (2011) after the 2010 Chile Earthquake, but for ultimate axial loads. Both Q and U walls of the SO building do not exceed the imposed limit in any case.

Based on the detailed results of the three walls, it is concluded that the assumed stiffness of structural elements has a significant influence on the prediction of the seismic demands of axial load, shear, and moment in RC walls. The observed trend suggests that when cracked sections are considered (models SR1 and SR2), the predicted seismic demands are lower than those predicted when gross sections are used (models SR3 and R3). The results also support that the assumed in-plane diaphragm stiffness influences the behavior of the seismic demands, which clearly shows the necessity of including the non-linear behavior of the slabs in tridimensional analyses

to further understand the effect of the slabs on the seismic demands in walls of RC buildings.

The following chapter analyzes the effect of the non-linear behavior of the slabs on the seismic demands of RC walls of a case study RC wall building.

### **3. STATIC ANALYSIS OF RC WALL BUILDING WITH NON-LINEAR COUPLING SLABS**

#### **3.1 Introduction**

The behavior of 3D RC wall buildings with coupling slabs have been studied experimentally using the results from a full-scale 7-story building slice tested at UC–San Diego (Panagiotou and Restrepo 2010; Panagiotou et al. 2011). These studies concluded that the 3D interaction effects caused a significant increase in the system overturning moment capacity. Moreover, the kinematic interaction between walls and the slabs framing them increased the shear demand in the walls and caused significant variation in their resistance to axial force and bending-moment.

On the other hand, important analytical studies have investigated the overall behavior of 3D RC wall buildings with coupling slabs. Conclusions from those works have shown the importance of the slab-wall coupled action on the seismic performance of RC buildings. Jünemann et al. (2016a) concluded that the 3D interaction of the walls with the rest of the structure is a key factor for understanding the seismic behavior of the studied building. Gallardo et al. (2021) concluded about the relevance of the slabs effective stiffness on the non-linear behavior of such types of buildings. Zhang et al. (2017) concluded that the coupling action between slabs and walls along the central corridor of the building is one of the reasons for the large reserve of lateral strength identified in such building. Additionally, the authors concluded that the coupling action between walls and slabs provides additional resistance at the expense of reducing the drift capacity of the building and increasing the shear demand in some walls. Finally, Ugalde et al. (2019) concluded that the stiffness of the slabs affect the analyses of the building and recommended additional research on this modeling issue.

Albeit the advances in RC buildings with coupling slabs, there is still a lack of knowledge and information regarding their seismic behavior. The main objective of

this chapter is to assess the seismic behavior of an RC structural wall building with non-linear coupling slabs. Additionally, this chapter evaluates the effect of the amount of slab reinforcement on the seismic performance of the studied structure.

A case study building, representing a residential structure in Chile, is utilized. The seismic behavior of the case study building is assessed from non-linear static analyses using 3D models with shell-type elements. Seven models of the case study building were created to study the effects of the non-linear behavior of the slab and the reinforcement ratio of the slabs on the seismic response of the structure. The seismic performance is evaluated from roof displacements and shear, moment, and axial forces of the walls. The coupling degree is also computed for each model. Finally, the performance is also evaluated from concrete and steel strain demands in both walls and slabs. Relevant conclusions about the building behavior, slab demands, and failure mode are obtained.

### **3.2 Case study building**

As mentioned in the previous chapter, Chilean residential buildings are characterized by have a floor plan configuration with a central longitudinal corridor structured with long walls and shorter transverse walls that separate habitational spaces (Jünne man et al. 2015). Walls in each principal direction are often connected to form T-shaped or L-shaped cross-sections (Wallace et al. 2012). The walls are framed with coupling slabs, and beams are used in these buildings mainly to support balconies. A simplified RC structural wall building structured with T-shape walls, which represents that configuration, is used as a case study.

The geometry of the case study building was determined considering the characteristics of 36 damaged buildings inventoried by Jünemann et al. (2015). The case study building has 16 identical stories and no basements. The selected story height is 2.6 m and the total height of the building is  $H = 41.6$  m. For the plan dimensions, a length of

36 m and a width of 18 m were selected, Figure 3- 1. The slenderness ratio of the building, defined as the quotient between the total building height and the shorter dimension of the floor plan, is 2.31, which is equivalent to the average slenderness ratio of the inventory of buildings reported by Jünemann et al. (2015). The slab thickness is defined as 15 cm in all stories, which is a common thickness in Chilean buildings (Wallace et al. 2012).

The case study building is a structure with eight identical T-shape walls, Figure 3- 1. A thickness of 30 cm is selected for the web and flange of the T-shape walls. This wall thickness is larger than the average thickness of Chilean buildings reported by Jünemann et al. (2015), but it allows the inclusion of special boundary elements, which are required by the current design code (MINVU 2011). The total length of the web of the walls is 765 cm and the length of the flanges is 750 cm. The width of the longitudinal corridor of the building, measured from the axis of the flanges of the T-shape walls, is 1.8 m.

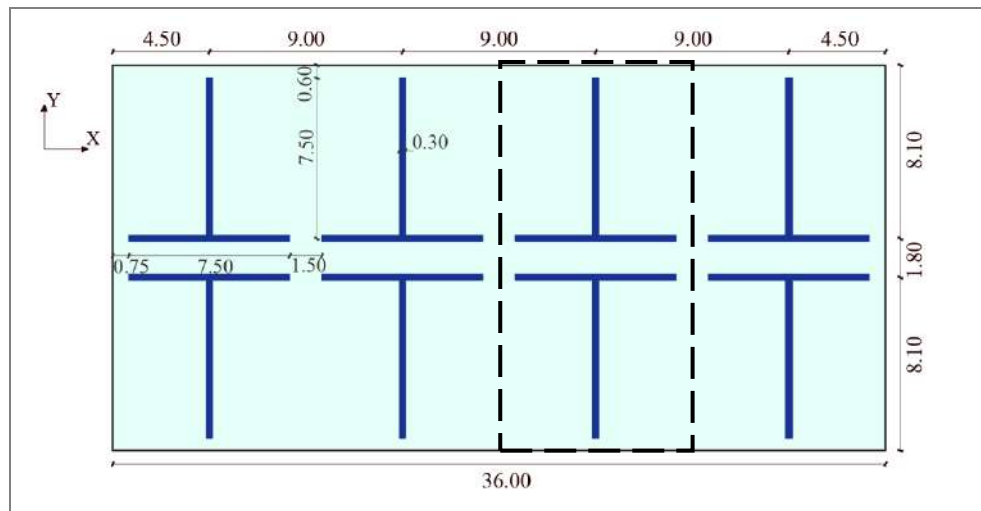


Figure 3- 1: Plan view of case study building, representative of the of residential buildings configuration in Chile.

For designing the case study building, a linear-elastic finite element model was constructed in ETABS 2010 using the gross moment of inertia of the elements. The building is assumed to be located in Santiago in soil type C, according to DS61 (MINVU 2011). A rigid in plane diaphragm was assumed at each floor level and the soil-structure interaction was neglected. Dead loads ( $D$ ) consider the weight of the structural elements and a distributed uniform load of  $2.0 \text{ kN/m}^2$ . This imposed load considers the weight of the wall cover, ceiling, and other non-structural components. For the live loads ( $L$ )  $2.0 \text{ kN/m}^2$  was considered for the apartment spaces according to the Chilean code (INN 1986). The seismic weight of the building, estimated with  $D + 0.25L$ , is  $W = 102,080 \text{ kN}$ . For the material properties, a specified compressive strength of  $25 \text{ MPa}$  is assumed for the concrete and a specified yield strength of  $420 \text{ MPa}$  is assumed for the reinforcing steel. These material properties are common in Chilean buildings (Estay 2008). The seismic demands are estimated from a linear spectrum analysis according to the Chilean code (MINVU 2011).

The case study building is analyzed only in the transverse direction (Y direction); therefore, only information related to this direction is provided. The fundamental period ( $T$ ) of the building is  $0.613 \text{ s}$ , which results in a ratio  $N_T/T = 26.1 \text{ 1/s}$ , where  $N_T = 16$  is the total number of stories. The value of this ratio is consistent with the reported values for RC wall buildings in Chile (Jünemann et al. 2015). The stiffness index of the building is  $H/T = 67 \text{ m/s}$ , which classifies the building as a normal stiffness building according to Guendelman and Lindenberg (2010). A building is classified as stiff when its stiffness index is larger than  $70 \text{ m/s}$ .

The elastic base shear obtained from the response spectrum analysis in the transverse direction is  $V_{\text{elas}} = 46,920 \text{ kN}$  ( $0.459 W$ ). The design of the building is controlled by the minimum base shear defined in DS61 (MINVU 2011) for reduced actions, where the strength reduction factor was calculated to reach the minimum base shear of  $0.05 W = 5,104 \text{ kN}$ . The minimum base shear requirement implies an effective strength reduction factor of  $R_{ef} = 7.41$ . The ultimate base shear used for design, which

includes the 1.4 amplification factor defined in NCh3171 (INN 2010) for the load combinations with earthquake loads, is  $V_u = 8,865$  kN, (0.087  $W$ ).

The walls of the buildings were designed according to the DS60 (MINVU 2011), which adopts ACI 318 (ACI 2008) with some modifications. Considering a cracked period of  $T_{cr} = 1.5T$ , the ultimate roof displacement according to DS61 (MINVU 2011) is  $\delta_u = 12.98$  cm (i.e. roof drift ratio of 0.31%). Special boundary elements are required at the webs of the walls since the estimated compressive strain at the plastic hinge location in the stem of the walls is 0.0037. Boundary elements were also provided at the ends of the flanges and at the web-flange intersection. The considered length of the boundary elements at the edge of the web and the flange ends is 115 cm, and at the web-flange intersection is 70 cm. The longitudinal reinforcement ratio at the web and flange boundaries is 1.23% and at the web-flange intersection is 1.30% (see Figure 3-2). Transverse reinforcement in the special boundary elements was specified to satisfy the DS60 (MINVU 2011) requirements (Figure 3- 2). For the distributed longitudinal reinforcement of the web and flanges of the T-shape walls the minimum reinforcement ratio of  $\rho_l = 0.0025$  is considered (ACI 2019), which is achieved with two layers of  $\phi 10$  mm bars spaced at 20 cm. For the shear design, minimum shear reinforcement in the web of the walls was sufficient; hence they were reinforced with transverse  $\phi 10$  mm bars spaced at 20 cm, which results in a reinforcement ratio of  $\rho_t = 0.0026$ .

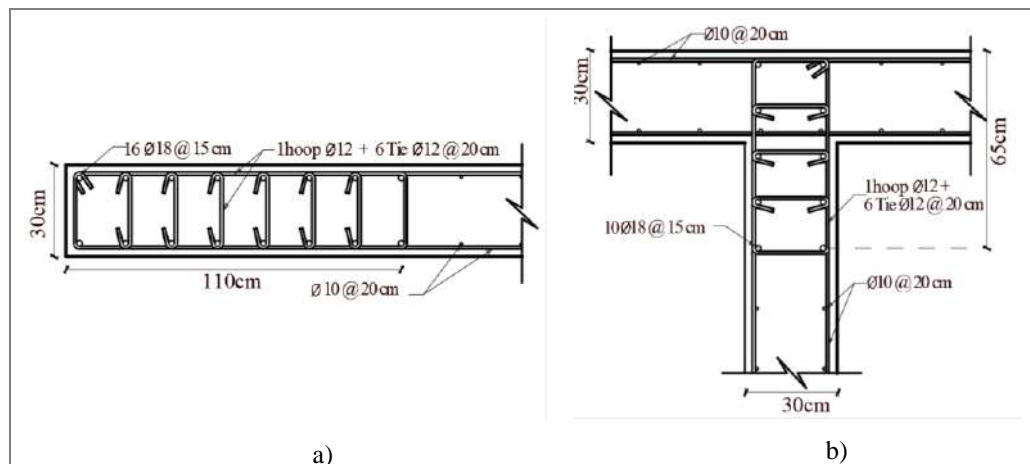


Figure 3- 2: Reinforcement details of the T-shape walls. a) Special boundary elements for both web and flange and b) web-flange intersection.

### 3.3 Non-linear finite element models

The non-linear seismic response of the case study building is evaluated using 3D models in DIANA (TNO DIANA 2017). This software was selected because it has shown good results in previous research regarding RC wall buildings (Jünemann et al. 2016a; Dashi et al. 2014; Jünemann et al. 2016b; Vásquez et al. 2020) and because it allows for the consideration of the non-linear behavior of the slabs. The finite element model is validated with the results of the TW2 wall, a T-shape RC wall tested by Thomsen & Wallace (1995) and with the results of the specimen EUC\_BUILD3, a one-story two-bay wall-slab-wall RC subassembly tested by Brunesi et al. (2018) in the EUCENTRE laboratory.

The TW2 wall is modeled using four-node quadrilateral iso-parametric curved shell elements (Q20SH) with five degrees of freedom per node (three translations and two rotations) and four integration points in each element. Thirty-six quadrilateral elements were considered in the wall height, with a side of approximately 7.5 cm. The concrete behavior at the integration points is modeled considering a smeared cracking approach, following the total strain rotating crack model (TNO DIANA 2017). In this approach, the stresses are evaluated in the directions of the principal strains, which rotate during crack propagation. During loading, the concrete is subjected to both tensile and compressive strains, which can result in cracking or crushing of the material. The compressive behavior is modeled using the parabolic relationship implemented in DIANA (TNO DIANA 2017), which regularizes the stress-strain relationship based on the element size in order to keep the compressive fracture energy  $G_c$  constant. The compression softening effect is considered using the strength reduction due to lateral tensile strains proposed by Vecchio and Collins (TNO DIANA 2017). For the tensile behavior, the Hordijk constitutive relationship is assumed. This approach is based on

the tensile fracture energy  $G_f$  obtained following the CEB-FIP (1990) recommendations.

The reinforcing steel is modeled using the embedded formulation, which assumes a perfect bond between steel and concrete. The reinforcing steel is modeled using both bar and grid elements available in DIANA. The behavior of the steel is represented through the Menegotto-Pinto model (Menegotto and Pinto 1973; Filippou et al. 1983). Neither bar buckling nor bar fracture are accounted for in the proposed model. Values of the initial tangent slope ratio of the hardening branch  $b$ , and the initial curvature parameter  $R_0$ , are assumed following recommendations from the literature (Papadrakakis et al. 2008; Deaton 2013).

The cross-section and reinforcement detailing of the TW2 wall used to validate the numerical model is shown in Figure 3- 3a). The length of the web and flange of the wall is 48 in. and the wall thickness 4 in. (1 in. = 2.54 cm). The distributed longitudinal steel ratio of the web and flange is  $\rho_l = 1.2\%$ , and the transverse steel ratio of the web is  $\rho_t = 0.44\%$ . The material properties used in the DIANA model were taken from Thomsen and Wallace (Thomsen and Wallace 1995). A strength of  $f'_c = 32.2$  MPa is used for concrete and a yield strength of  $f_y = 434$  MPa is used for bars #3 and 3/16". Bar #2 are simulated using  $f_y = 448$  MPa. The wall possesses special boundary elements at the ends of the web and flange, which are modeled using confined concrete with  $f'_{cc} = 57.9$  MPa and 49.6 MPa, respectively. The TW2 wall was tested with a constant axial load of  $0.074 f'_c A_g$  and was subjected to lateral displacement cycles. For the DIANA model, the axial load was uniformly distributed throughout the nodes of the web and flange. The axial load was applied as a first step of the analysis. Subsequently, the lateral displacements of top web nodes were applied following the load pattern used in the experimental test.

The comparison between the experimentally measured and numerically estimated response of the TW2 wall is shown in Figure 3- 3b). Overall, the analytical model is

able to reproduce the experimental results adequately. For positive displacements (i.e., when the flange is in compression), the estimated maximum strength is 7.7% smaller than the measured strength. The analytically predicted strength when the web is in compression (i.e. negative displacements) is 7.0% larger than that from experimental results. The obtained differences are similar to the ones reported by Lu and Panagiotou (2014) when comparing the experimental response of the wall TW2 with the one predicted using the beam-truss model. Finally, Figure 3- 3b) shows that the numerical model is not able to predict the unloading behavior accurately because the analytical response does not show the gradual decrease of stiffness observed in the experimental response, especially when unloading from positive displacements.

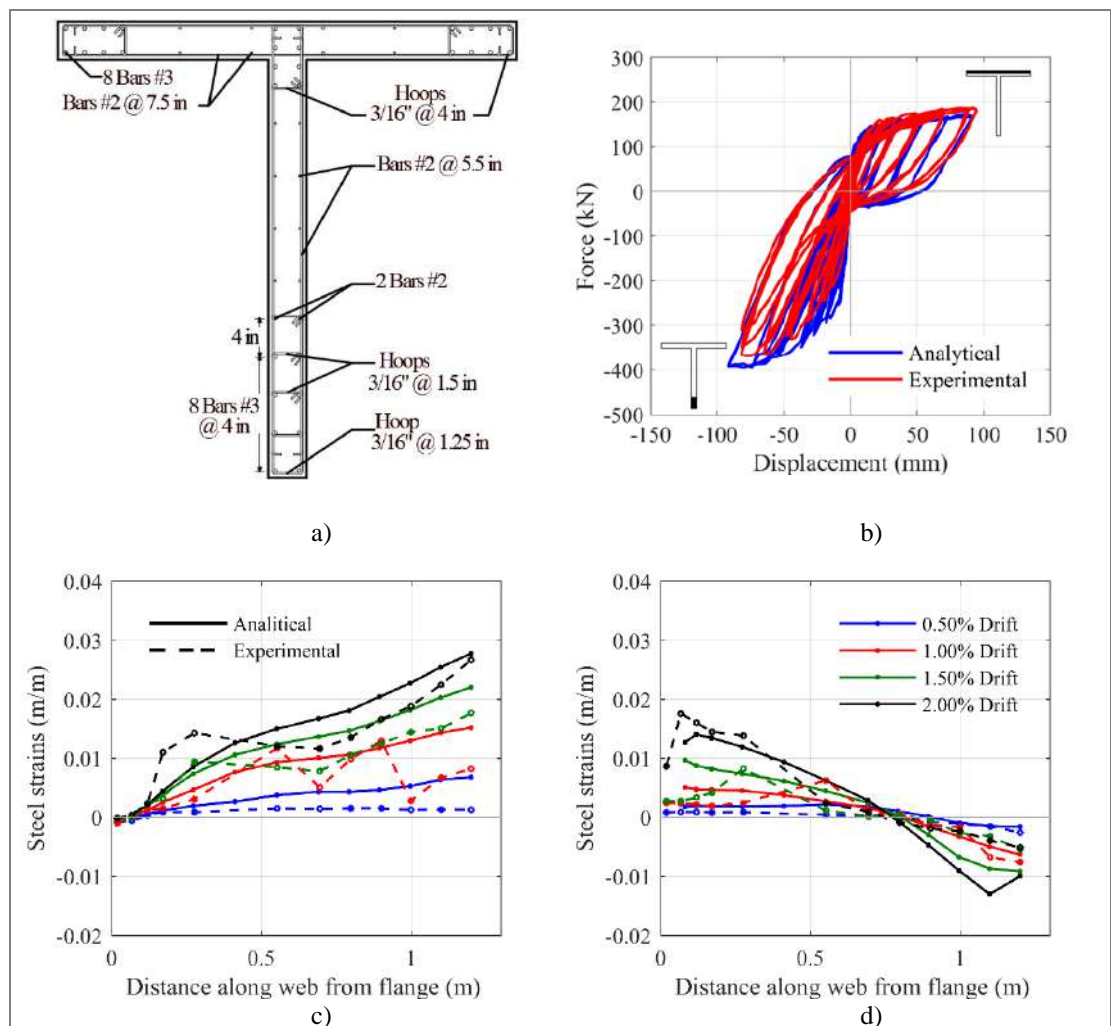


Figure 3- 3: a) Cross-section and reinforcement TW2 wall and b) Experimental and analytical global results; c) and d) Local results for reinforcement strain at the base of the TW2 wall for positive and negative displacement, respectively.

To evaluate the local response of the model, the steel strains measured during the test are compared with those predicted by the DIANA model in Figure 3- 3c) and Figure 3- 3d). The plots compare the strains recorded by the strain gauge located at the base of the TW2 wall with those predicted by the FE model at approximately 7.5 cm above the base of the wall. The figures show that the model predicts the steel strain for negative displacements relatively well, and the difference increases as the drift increases. For positive displacement Figure 3- 3c) shows that the tensile strains at the edge of the web predicted by the model are on average 38% larger than the experimental measurements. Additionally, Figure 3- 3d) shows that the model overestimates the compressive strains for drifts larger than 0.5. It should be noted that the compressive strains predicted by the model at the base of the wall (not at 7.5 cm above the base) are larger than those shown in Figure 3- 3d) due to localization. However, the compressive strain reported in the test were not measured where damage was concentrated (above the base of the wall); hence the experimental strains are compared to the analytical strains measured at the vicinity of the damage concentration.

Figure 3- 4 shows a 3D drawing of the EUC\_BUILD3 specimen tested by Brunesi et al. (2018). The structure prototype consists of three walls and one slab of two bays with dimensions in plane of 8.4 m length and 4.0 m width and a story height of 2.7 m. The floor consists of two 16 cm thick slabs spanning 4.2 m between the walls and the thickness of the three walls is 18 cm.

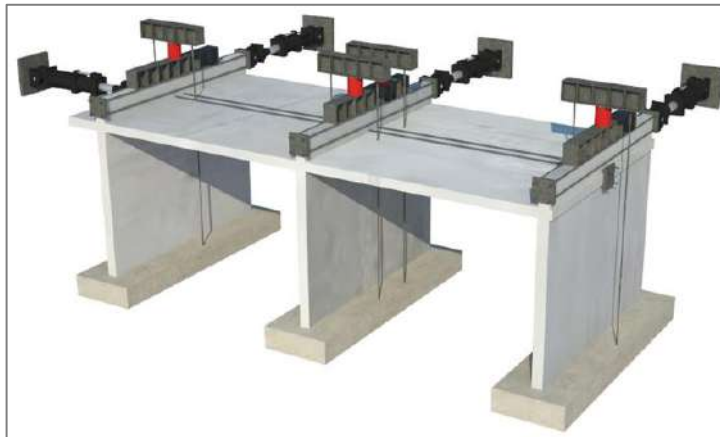


Figure 3- 4: 3D drawing of the full-scale EUC\_BUILD3 prototype (from Brunesi et al. 2018).

The three walls were reinforced with two layers of reinforcement, using  $\phi 8$  mm vertical bars spaced at 25 cm  $\phi 5$  mm horizontal bars spaced at 25 cm. The walls did not have special boundary elements, so they did not have confined concrete. The floor slabs were reinforced with a lower reinforcement layer of  $\phi 10$  mm bars spaced at 18 cm and  $\phi 6$  mm bars spaced at 25 cm distributed uniformly along the length and width of the specimen, respectively. The upper reinforcement layer of the slabs consisted on  $\phi 12$  mm bar spaced at 10 cm (parallel to the length) and  $\phi 8$  bars spaced at 25 cm (parallel to the width).

The EUC\_BUILD3 prototype is modeled in DIANA using the same modeling assumptions as those used for the model of the wall TW2. The four-node quadrilateral iso-parametric curved shell elements (Q20SH) were used. The concrete behavior was modeled considering a smeared cracking approach, following the total strain rotating crack model. The compressive behavior of the concrete was modeled using the same parabolic relationship of the TW2 wall. The compression softening effect was considered using the strength reduction due to lateral tensile strains proposed by Vecchio and Collins, and the concrete tensile behavior was modeled using the Hordijk

constitutive relationship. Specific properties of the concrete were taken from the test campaign report *EUC095/2017U* (Brunesi et al. 2017).

The reinforcing steel of the wall and slabs was modeled using grid elements available in DIANA. The behavior of the steel was represented through the Menegotto-Pinto model (Menegotto and Pinto 1973; Filippou et al. 1983). Values of young modulus, yield strength, and the initial tangent slope ratio of the hardening branch  $b$  were defined according to the material properties reported by Brunesi et al. (2017). The initial curvature parameter  $R0$  and the rest of the necessary parameters were assumed following recommendations from the literature as was made for TW2 model. Figure 3-5 shows the three-dimensional view of the FE model constructed in DIANA.

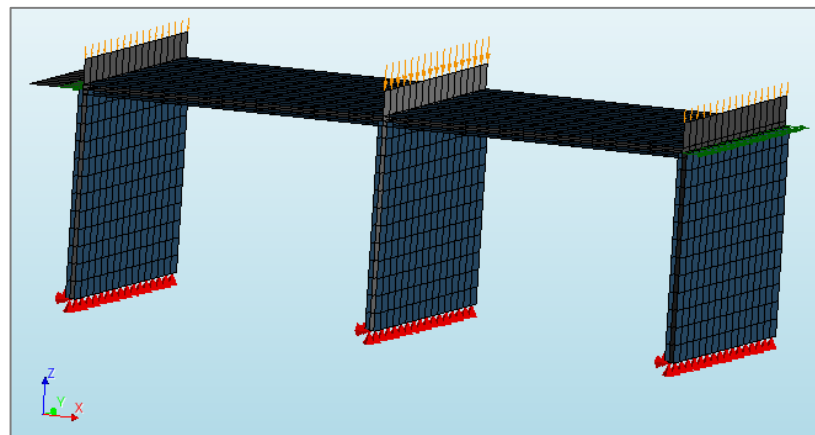


Figure 3- 5. 3D view of the EUC\_BUILD3 DIANA model.

During the test of the EUC-BUILD3, the walls were subjected to constant axial loads, which were monotonically applied to the specimen before the application of the lateral loading protocols through hydraulic jacks. The central wall was loaded with 210 kN of axial load, and lateral walls were loaded with 105 kN. A displacement-controlled protocol was first applied in the longitudinal/weak direction of the specimen and then a different displacement protocol was applied in the transverse/strong direction. For the non-linear static analysis in DIANA, the axial load was distributed uniformly

throughout the nodes of the web of the wall. Subsequently, the model of the EUC-BUILD3 structure was subjected to a non-linear static analysis in the longitudinal direction. Lateral displacements were applied at the top of the web nodes following the same load pattern used in the experimental test.

The cyclic horizontal force-displacement curve obtained from the experimental measurement is compared with the envelope predicted by the DIANA model in Figure 3- 6. The figure shows that the non-linear static analysis predicts reasonably well the envelope of the experimental result. This comparison allows concluding that the DIANA model is able to capture the coupling effect of the slab in the weak direction of the walls. Therefore, the DIANA model is expected to simulate adequately the seismic behavior of walls with coupling slabs.

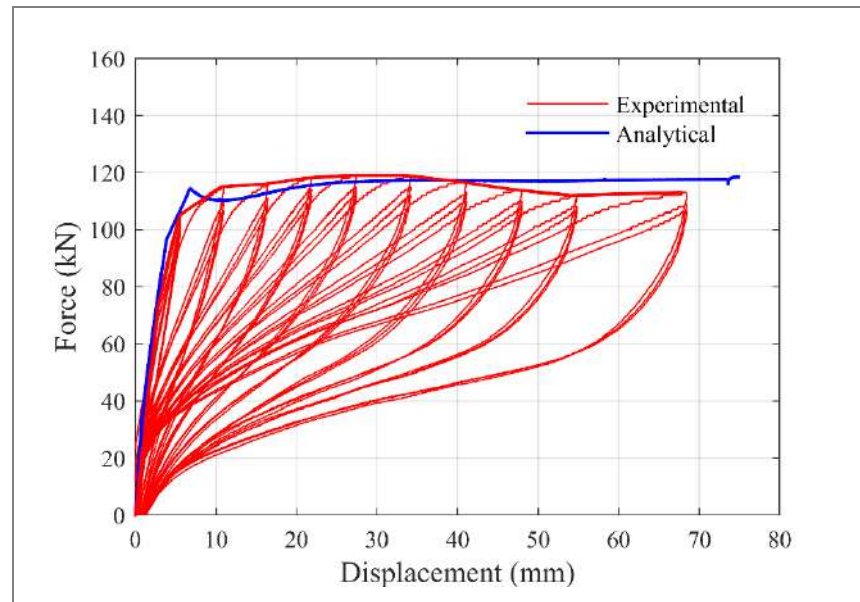


Figure 3- 6: Comparison between experimental cyclic response and monotonic response estimated with the DIANA model.

The 3D model constructed in DIANA to estimate the seismic response of the case study building described in section 3.2 is shown in Figure 3- 7. To save computational efforts and due to the regularity of the case study building, only the representative slice of the building enclosed in Figure 3- 1 is modeled. Representative slices have been used to

simulate the behavior of RC wall buildings by other authors (Deger and Wallace 2015). The elements and material types used to simulate the slice of the building are the same as the ones used to simulate the TW2 wall. The walls and slabs were discretized using regular curved shell elements with a side of approximately 50 cm and the structural element connections considered a compatible mesh. Expected materials properties following the recommendations of PEER/TBI (2017) and ACHISINA (2017) were used. The expected concrete compressive strength is  $f'_c = 32.5$  MPa and the expected yield strength of steel is  $f_y = 491.4$  MPa. Special boundary elements, shown in blue in Figure 3- 7, are simulated using confined concrete material with a compressive strength of  $f'_{cc} = 48.8$  MPa. This strength was estimated following Mander et al. (1988). The values of compressive fracture energy used for confined and unconfined concrete were 722521 N/m and 50167 N/m, respectively. The tensile fracture energy used for both confined and unconfined concrete was 132.4N/m. The slabs and the rest of the walls were modeled using unconfined concrete material.

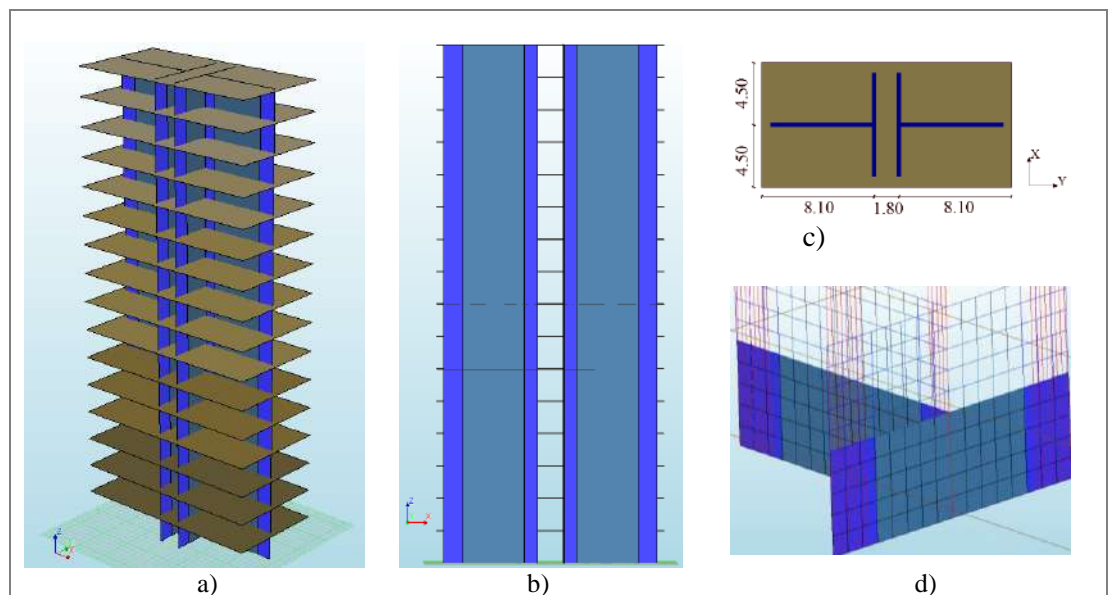


Figure 3- 7: a) Three-dimensional; b) elevation; c) plan and d) special boundary elements reinforcement views of the DIANA model (units in meters).

Distributed longitudinal and horizontal reinforcement of the walls is simulated with a single layer grid reinforcement located at the central axis of the web and flanges (see Figure 3- 7d). The longitudinal reinforcement of the special boundary elements was defined using bar elements (red lines in Figure 3- 7d). The transverse reinforcement of the special boundary elements was not modeled explicitly since its effect is considered through the confined concrete material properties. Finally, the top and bottom reinforcement of the slabs is modeled using two grid reinforcement in each slab.

The model was subjected to a gravity load equivalent to  $D + 0.25L$ . This load was applied as uniform pressure on the slabs. The mass of the building was achieved by specifying a mass density for the concrete material for walls and slabs. The mass density used in the model accounts for the gravity loads. The fundamental period obtained from the DIANA model, using linear elastic material properties, is  $T_1 = 0.601$  s, which is 2.0% smaller than that of a 3D model constructed in ETABS. This small difference is reasonable in models with different element formulations (Chacón et al. 2017).

The sensitivity of the results to the discretization of the mesh is evaluated by comparing the global response of the structure obtained with the model NLS1, with a mesh size 50 cm, with that obtained from models with different mesh sizes. The size of the quadrilateral elements used in the other models are 25 cm, 75 cm and 150 cm. The comparison between the force-displacement curves (base shear versus roof drift ratio) are shown in Figure 3- 8. The figure shows that the models with larger mesh sizes predict similar results than that of the NLS1 model (mesh 0.5 in Figure 3- 8). The response of the model with the mesh size of 25 cm shows major differences with the responses of the other models for roof drift ratios smaller than about 0.38. Nevertheless, for larger roof drift ratios the response predicted by the model with the mesh size of 25 cm is similar than that of the NLS1 model.

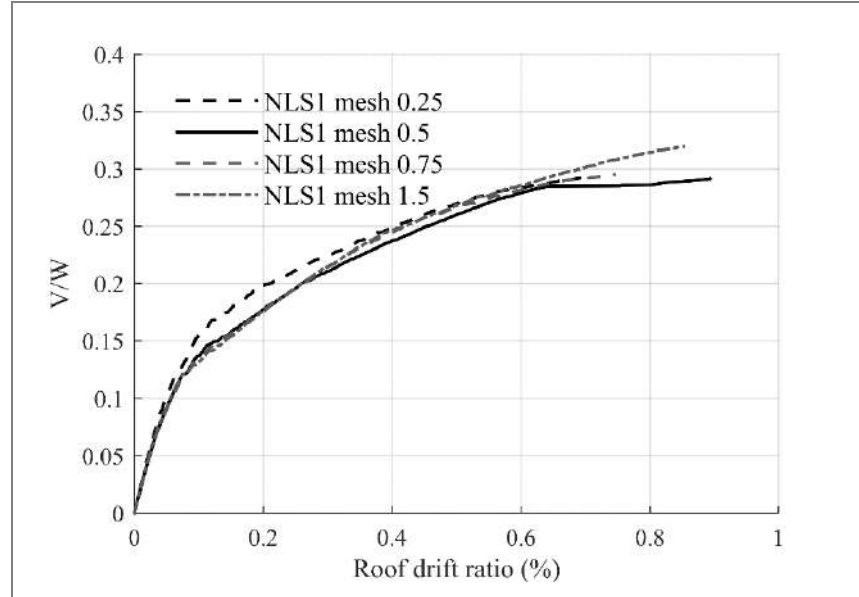


Figure 3- 8: Comparison of global result (roof drift ratio and total base shear) predicted with models with different mesh size for both walls and slabs.

The response of the axial load on each wall, predicted by the four models with different mesh sizes, is compared in Figure 3- 9. The figure shows that the axial loads in both walls predicted by the models with mesh size of 25 cm and 50 cm are similar. The axial loads predicted by the models with mesh sizes of 75 cm and 150 cm are also similar between them, but the axial loads predicted by these models are higher than those predicted with the models with smaller mesh sizes (25 cm and 50 cm)

Table III- 1 summarizes the computational time needed for the models with different mesh sizes to achieve convergence in the non-linear static analyses. The maximum roof drift ratios predicted by the models until convergence was achieved are also listed in the Table III- 1. As expected, the computational time needed when the mesh size is reduced increases significantly. Based on the comparison of the computational time, and on the fact that the models with mesh sizes of 25 cm and 50 cm predicted similar global results, a mesh size of 50 cm considered for the rest of the models in this thesis.

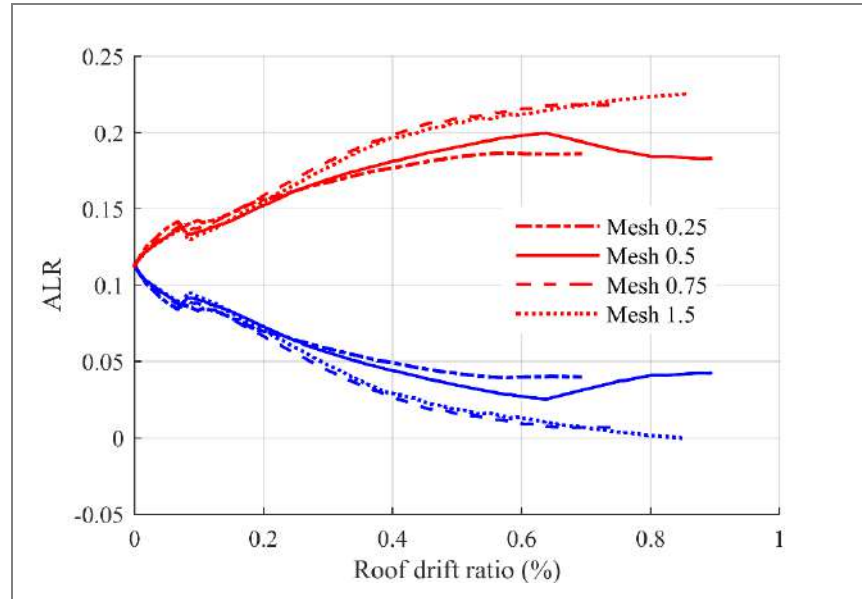


Figure 3- 9: Comparison of the axial load ratio predicted with the four models with different mesh size.

Table III- 1: Computational time needed to obtain the results from models with different mesh size.

Mesh size (cm)	Time	Max drift level achieved
25	7days + 11h	0.69%
50	14h	0.89%
75	5h	0.74%
150	3h	0.85%

Seven models of the case study building were created to study the effects of the non-linear behavior of the slab and the reinforcement ratio of the slabs on the seismic response of the structure (Table III- 2). The first four models (LS100, LS40, LS25, and LS10) consider non-linear behavior for the walls and linear elastic behavior for the slabs. The last three models (NLS1, NLS2, and NLS3) consider non-linear behavior for both walls and slabs. The first four models aim to evaluate the effect of using

reduced (i.e., cracked) moment of inertia of the slabs on the seismic response of the building. The considered moments of inertia are 100%, 40%, 25%, and 10% for the models LS100, LS40, LS25, and LS10, respectively. The reduced moment of inertia of the slabs in these models is achieved by reducing the concrete modulus of elasticity, and the reinforcement of the slabs is not considered. In these four models. Results from these four models are compared with the one obtained from the NLS1 model to identify if models with linear elastic slabs can represent the response of a model with non-linear slabs.

The last three models (NLS1, NLS2, and NLS3) are aimed at evaluating the effect of the reinforcement ratio of the slabs on the seismic response of the building with non-linear slab behavior. The model NLS1 is defined with a top and bottom reinforcement ratio ( $\rho$ ) of 0.002. This reinforcement ratio is equivalent to the minimum flexural reinforcement for non-prestressed slabs, according to ACI 318 (ACI 2019). The negative and positive reinforcements of each slab in NLS1 model are assigned using top and bottom grids of  $\phi 8$  mm bars spaced at 18 cm in both directions. The models NLS2 and NLS3 are identical to the NLS1 model, but the slabs are modeled with two and three times the minimum flexural reinforcement ratio, respectively (Table III-1 Table III- 2).

For each model, the degree of coupling (doc) is computed using the same equation used by Harries (2001), which is shown in equation 3.1.

$$doc = \frac{P \cdot L}{\sum M_w + P \cdot L} \quad (3.1)$$

In equation 3.1,  $P$  the axial load transferred to the walls by the coupling elements and  $L$  is the lever arm between the centroids of walls. Then  $P \cdot L$  is the moment resisted by the walls due to the coupling action. Finally,  $\sum M_w$  is the sum of the overturning moment of the two walls.

Table III- 2: Numerical models of the case study building

Model	Slab behavior	Moment of inertia of slabs	$\rho$
LS100	Linear	100%	--
LS40	Linear	40%	--
LS25	Linear	25%	--
LS10	Linear	10%	--
NLS1	Non-linear	100%	0.002
NLS2	Non-linear	100%	0.004
NLS3	Non-linear	100%	0.006

The fundamental period of the case study building obtained with the NSL1 model is 0.571 s, which is 5.0% lower than that obtained with a linear-elastic model in DIANA (not listed in Table III- 2). The smaller period in the NLS1 model is attributed to the increase of stiffness generated by modeling the reinforcement in the walls and slabs.

After applying the gravitational loads, the seven models were subjected to a non-linear static analysis in the positive Y-direction (Figure 3- 1) using a lateral load distribution associated with the first vibration mode of each model. The lateral loads were applied using more than 650 load increments. The Newton-Raphson iteration method was used at each load increment to achieve convergence. The force, energy, and displacements convergence criteria were used with relative tolerances of 0.001, 0.0001, and 0.01, respectively.

In this study, the failure of the structure was assessed through post-processing the results. Structural failure of the structure is assumed when the compressive strain of confined concrete reaches 0.008. This compressive strain is the limit allowed by DS60 (MINVU 2011) in special boundary elements. For unconfined concrete in walls and slabs, structural failure is assumed when the compressive strain reaches 0.005 is achieved, following the recommendations of previous studies (Lu et al. 2011; Deger and Wallace 2015). Finally, structural failure is also assumed when the tensile strain of

steel exceeds 0.05. This latter strain limit is associated with bar fracture according to the recommendations of Gogus and Wallace 2015, Dabaghi et al. 2019 and Parra and Moehle 2014, to account for low cycle fatigue.

### **3.4 Effect of the reduced moment of inertia of slabs**

This section compares the predicted response of the case study building using non-linear walls and linear slabs with different moments of inertia (models LS100, LS40, LS25, and LS10 in Table III- 2) with that of a full non-linear model (model NLS1). The non-linear static analysis of each model was carried out until convergence was achieved; hence this time step does not necessarily indicate structural failure (Haselton et al. 2009). The global response of the structure predicted with the five models is evaluated to establish the comparisons. A detailed description of the seismic response of the building predicted with model NLS1 is presented in the next section.

The relationship between the normalized base shear ( $V/W$ ) and the roof drift ratio (roof displacement over the building height) of the five models are shown in Figure 3- 10. The plot shows the results until convergence was achieved for each model. The structural failures for the five models (marked with dots in Figure 3- 10) were associated to the exceedance of the compressive strain limit of 0.008 for confined concrete. Structural failure for the LS100, LS40, LS25, and LS10 models occurred at roof drift ratios ( $\delta_{\text{failure}}$ ) of 0.59%, 0.64%, 0.68% and 0.75% respectively, which are 24%, 18%, 13% and 4% smaller than that of the NLS1 model (0.78%). Greater strength on slabs generate a faster damage on walls because of the axial load that those received from this coupling element. The increase of the axial load on the walls increases the compression strain demand on them and causing that the material capacity to be exceeded faster.

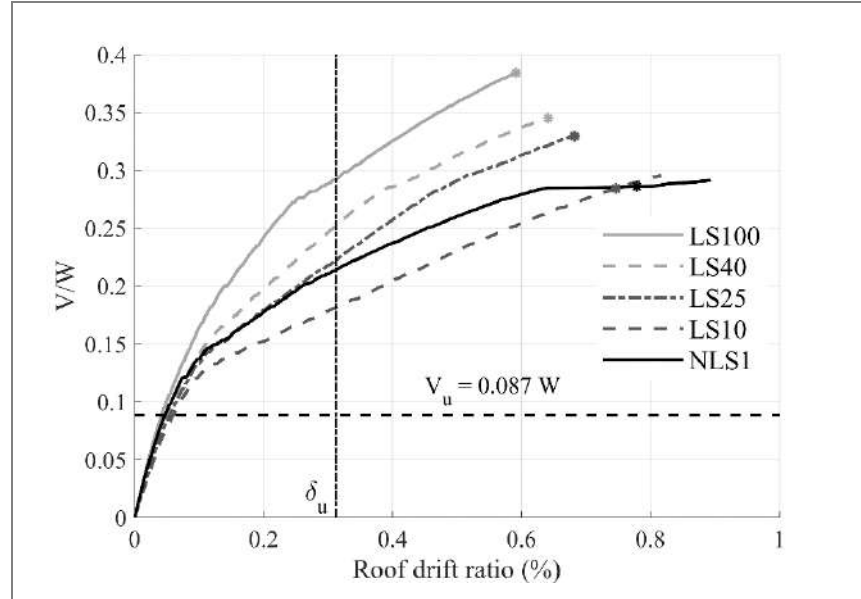


Figure 3- 10: Non-linear static analysis results for the four linear models with linear slabs (LS100, LS40, LS25, and LS10) and the NLS1 model with non-linear slabs. Structural failure is marked with dots.  $\delta_u$  is the design displacement (0.31%) according to DS61 and  $V_u$  the ultimate design shear (0.087W).

The maximum base shears ( $V_{max}$ ) predicted at the end of each analysis are summarized in Table III- 3. Figure 3- 10 and Table III- 3 also show that the maximum strength decreases as the moment of inertia of the slabs decreases. The highest strength (0.38 W) was predicted with the LS100 model and is 31% larger than that of the NLS1 model (0.29 W). The maximum strengths of the models LS40 (0.34 W), LS25 (0.33 W) and LS10 (0.29 W) are 18%, 12% and 1.4% larger than that of the NLS1 model. The roof drift ratios at maximum strength coincide with the point of no convergence for the five models. Nevertheless, the failure of the models LS10 and NLS1 were predicted at smaller roof drift ratios than those of maximum strengths and non-convergence. Figure 3- 10 shows that the roof drift ratio at maximum strength increases as the moment of inertia of the slabs decreases, which implies that the estimated deformation capacity of the building is inversely related to the stiffness of the coupling slabs. When the stiffness of the slabs increases, the axial forces and the strain demands on the wall in

compression increase, reducing the drift capacity of the structure. Finally, Figure 3- 10 shows that the responses of the models with linear slabs do not have a plateau, whereas the response of the NLS1 model has a region with a relatively constant base shear.

The overstrength factors  $\Omega_o$ , defined as the ratio of the failure strength ( $V_{\text{failure}}$ ) to the ultimate design shear ( $V_u = 0.087 W$ ), obtained for the five models, range between 3.26 to 4.41. The calculated factors are smaller than the values of 4.2 to 5.5 reported by Ugalde et al. (2018) for an RC Chilean building. However, the over strength factors calculated in this study (Table III- 3) consider the 1.4 amplification factor for  $V_u$  according to the load combinations of NCh3171 (INN 2010), whereas Ugalde et al. (2018) did not consider this factor. If the 1.4 amplification factor is introduced in the computations of Ugalde et al. (2018), their over strength factors are reduced to a range between 3,0 to 3.9, which agree with the values obtained in this study.

Table III- 3: Strength, overstrength factor and deformation capacity, LS100, LS40, LS25, LS10, and NLS1 models.

	LS100	LS40	LS25	LS10	NLS1
$V_{\text{max}}$ (W)	0.384	0.344	0.326	0.295	0.291
$V_{\text{failure}}$ (W)	0.384	0.344	0.326	0.284	0.286
$\Omega_o$	4.41	3.95	3.75	3.26	3.29
$\delta_{\text{failure}}$	0.59%	0.64%	0.68%	0.75%	0.78%
$\delta_{\text{failure}}/\delta_u$	1.90	2.06	2.19	2.42	2.52

The predicted roof drift ratios at failure (summarized in Table III- 3) are 1.90 times larger than the design displacement  $\delta_u$  (shown with a vertical line in Figure 3- 10) for model LS100 and 2.42 times larger for model LS10. For the model NLS1, the predicted roof drift ratio at failure is 2.52 times larger than  $\delta_u$ . Finally, it is concluded that the roof drift ratios at failure predicted with the five models for the case study building are

similar to the values of 0.65% to 0.75% predicted by Zhang et al. (2017) for a 15-story residential RC wall building in Chile.

The stiffness of the structure in the model LS100 is similar to the one of the NLS1 model up to a roof drift ratio of 0.03% (Figure 3- 10). For larger roof drift ratios, the stiffness of the structure in the model LS100 is larger than that of the model NLS1. Figure 3- 10 also shows that the initial tangent stiffnesses of the four models with linear slabs are similar to that of model NLS1 up to a roof drift ratio of 0.1%. The difference observed beyond this roof drift ratio stems from the non-linear behavior of the slabs in the model NLS1, where the progression of concrete cracking in the slab at the vicinity of the webs of the walls affects the stiffness of the building. For displacement smaller than the design displacement ( $\delta_u$ ) the response predicted by the model LS25 with linear slabs is the most similar to that predicted by the model NLS1 with non-linear slabs. However, the model LS10 is the one that better predicts the maximum strength and roof drift ratio at failure. Therefore, none of the considered models with linear slabs and reduced moments of inertia are able to predict the overall response of the building with non-linear slabs. This result shows the importance of considering the non-linear behavior of the coupling slabs in the studied building.

The degree of coupling obtained for the five models (LS100, LS40, LS25, LS10, and NLS1) is shown in Figure 3- 11. The figure shows the effect of the non-linearity of the slabs in the model NLS1 because a different trend of the doc is observed. For roof drift ratios smaller than 0.1%, the doc of the NLS1 decreases as the roof drift ratio increases. The cracking of the slabs limits the coupling axial forces and generates the reduction of the doc, since the coupling axial forces in the walls increases less than the bending moments of the walls. For larger roof drift ratios, the doc of the NLS1 model increases because the seismic axial forces of the walls increase more than the bending moments of the walls.

On the other hand, Figure 3- 11 shows that the doc of the four models with linear slabs (LS100, LS40, LS25, and LS10) only increases as the roof drift ratio increases. The

increase of the doc is attributed to the non-linearity of the walls, which limits the increase of the bending moment of the walls. At the end of the analyses, the doc values of the models LS100, LS40 and LS25 are relatively constant at about 36%, 33%, and 31%, respectively. Model NLS1 also shows a relatively constant doc value of about 26%, which decreases to 22% at the end of the analysis. On the other hand, LS10 model does not show a region with a constant doc value. Finally, the doc at failure for the models LS100, LS40, LS25, LS10 and NLS1 are 36.5%, 33.8%, 31.8%, 23.4% and 22.2%, respectively. It can be concluded that none of models with linear slabs represent accurately the doc behavior of the NLS1 model with non-linear slabs.

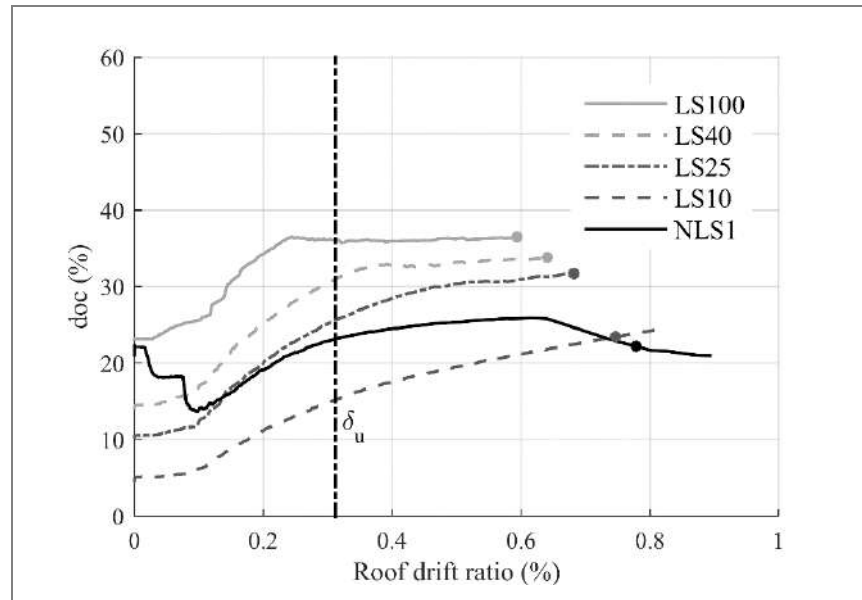


Figure 3- 11 Degree of coupling for the four linear models with linear slabs (LS100, LS40, LS25 and LS10) and the NLS1 model with non-linear slabs.

### 3.5 Seismic behavior of the building with non-linear coupling slabs

This section describes in more detail the seismic behavior of the case study building predicted with the model NLS1, which considers the non-linear behavior of the coupling slabs. First, the deformation and the crack pattern of the building are

evaluated. Second, the global response of the structure is evaluated from the predicted roof displacements and shear, moment, and axial forces of the walls. Finally, the local responses of the walls and slabs are assessed with the estimated stress and strains for both concrete and steel.

The deformation and the crack pattern of the building predicted with the NLS1 model at three different roof drift ratios (0.04%, 0.2%, and 0.6%) are shown in Figure 3- 12. The figure shows the normal crack strains of the webs of the walls. Additionally, Figure 3- 12a) shows the normal crack strains at the slabs which are shown at three-story intervals. Concrete cracking is initiated in the slabs at the vicinity of the web-flange intersection of the walls (Figure 3- 12a). The cracks in the walls are observed after the cracks in the slabs. This cracking sequence was observed experimentally by Schwaighofer and Collins (1977), who tested a subassembly of two rectangular walls coupled with slabs. Figure 3- 12b) and Figure 3- 12c) show that the crack pattern of the right wall is different from that of the left wall. At a drift ratio of 0.2% (Figure 3- 12b), the left wall shows cracks up to the 7<sup>th</sup> floor, whereas the right wall exhibits cracks up to the 4<sup>th</sup> floor. At a drift ratio of 0.6% (Figure 3- 12c) the cracks of the left wall compromise the whole web of the wall, whereas the cracks of the right wall are observed in about 2/3 of the web. Cracking is also predicted at the flanges of the walls. These cracks can be observed in (Figure 3- 12b) and (Figure 3- 12c) at the inner edge of the walls.

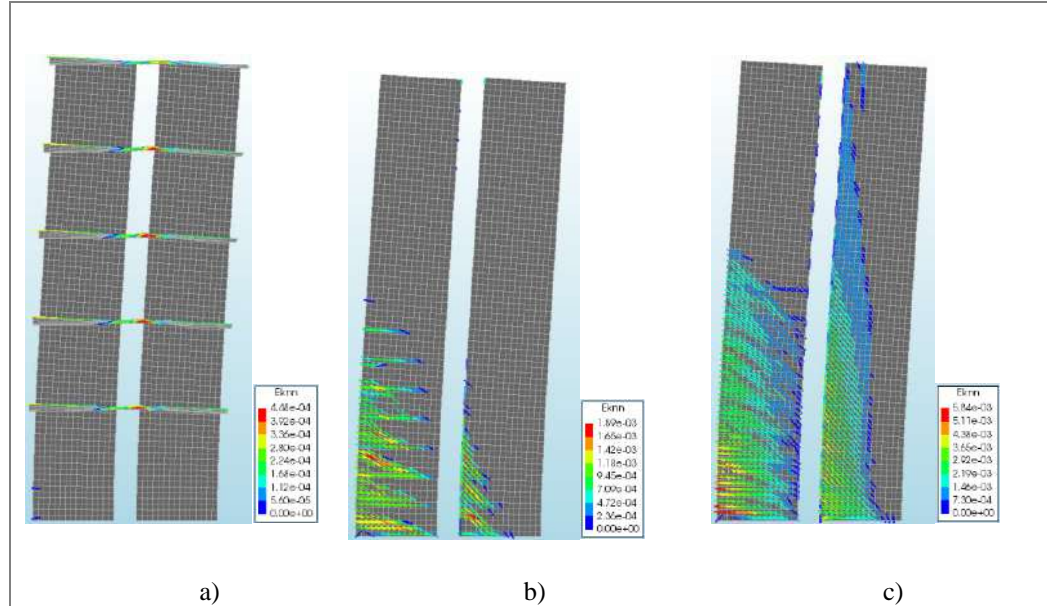


Figure 3- 12: Deformation of the building and normal crack strains in concrete with the NLS1 model for roof drift ratios of a) 0.04% (only the slabs of stories 4,7,10, 13, and 16 are shown), b) 0.20%, and c) 0.6%.

The Axial Load Ratio (ALR) of the two T-shape walls for the NLS1 model as a function of the roof drift ratio is shown in Figure 3- 13a). The ALR is defined as the total axial load relative to  $f'_c A_g$ , where  $f'_c$  is the specified concrete compressive strength (25 MPa) and  $A_g$  is the gross cross-section area of the wall. When the building is subjected to lateral forces, the left wall suffers tension (hereafter  $W_T$ ) and the right wall suffers compression (hereafter  $W_C$ ). Blue lines show the results for  $W_T$ , red lines for  $W_C$ , and the dashed grey line is the constant gravitational ALR. The variation of the axial loads of the walls is generated by the shear forces transferred through the slabs. At zero roof drift ratio, the ALR due to gravity loads of the two walls is 0.11 (Figure 3- 13a). The maximum ALR predicted for the  $W_C$  is 0.20 at a roof drift ratio of 0.64%. At the same roof drift ratio, the minimum ALR predicted for the  $W_T$  is 0.025. Due to the equilibrium of vertical forces, the increase in ALR in the  $W_C$  is equivalent to the decrease in ALR of the  $W_T$ . The variation of the ALR of the walls induced by the lateral load is equal to 78% of the gravitational ALR. Additionally, Figure 3- 13a)

shows an abrupt change of the ALR at a roof drift ratio of about 0.08% in both walls. This change is attributed to the cracking of the slabs at the vicinity of the web-flange intersection of the walls.

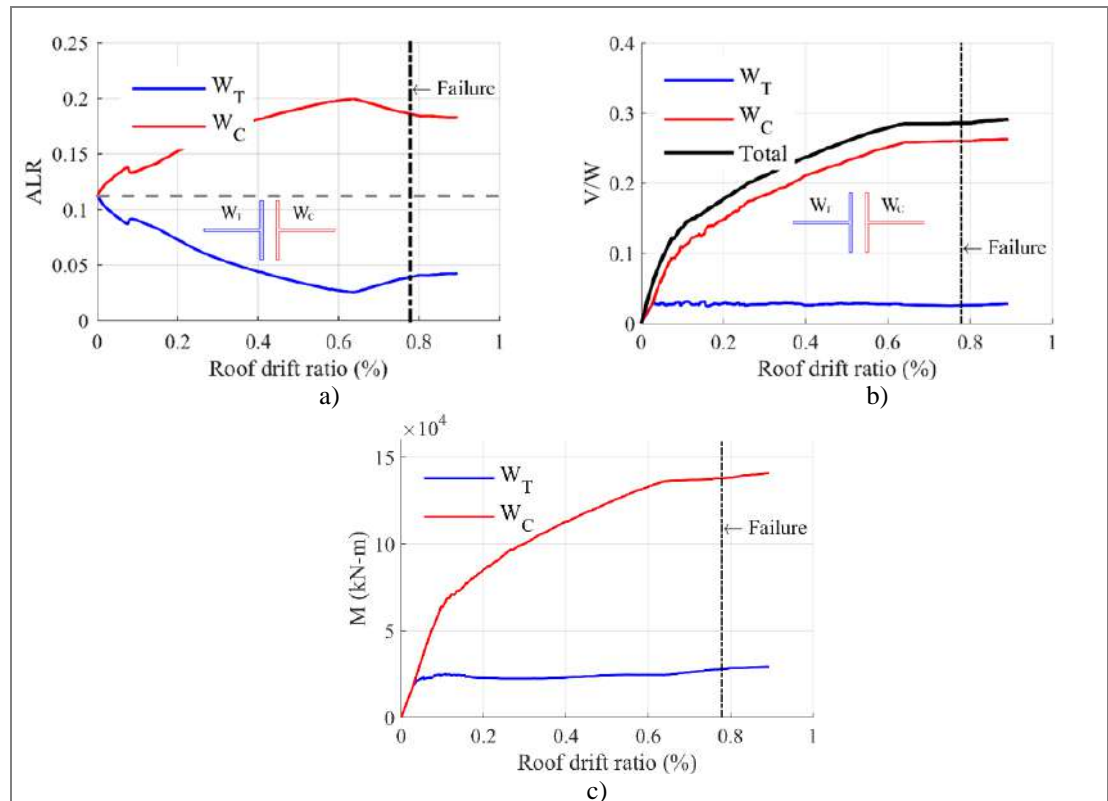


Figure 3- 13: Predicted forces at the base of the walls for the NLS1 model: a) Axial load ratio; b) Normalized base shear force, and c) Bending moment

The normalized shear at the base of the two walls ( $W_C$  and  $W_T$ ) and the total base shear of the building as a function of the roof drift ratio are shown in Figure 3- 13b). For roof drift ratios smaller than 0.03% (i.e., uncracked concrete), the shear of the  $W_C$  is identical to that of the  $W_T$ . For larger roof drift ratios, Figure 3- 13b) shows that most of the shear is taken by  $W_C$ , whereas the shear of  $W_T$  stays relatively constant until failure. At failure, the shear taken by  $W_C$  is 9.78 times larger than that taken by  $W_T$ . At a roof drift ratio of 0.08% (i.e., significant cracking in the slabs),  $W_C$  withstands 80%

of the total base shear, and at a roof drift ratio of 0.55%  $W_C$  withstands 90% of the total base shear. The significant difference in the shear forces taken by coupled walls has been observed previously by Aktan and Bertero (1984). These authors tested a subassembly of two rectangular walls coupled with slabs and observed that the compressed wall resisted 90% of the total base shear.

The bending moments at the base of the two walls as a function of the roof drift ratio are shown in Figure 3- 13c). It can be observed that the distribution of the moments of the  $W_T$  and  $W_C$  are analogous to the distribution of the shear force. For roof drift ratios smaller than 0.03%, the moments withstood by the two walls are similar. For larger roof drift ratios, the moment at the base of the wall  $W_C$  increases significantly (reaching 137,870 kN-m at failure), and the moment at the base of the wall  $W_T$  remains almost constant until failure (at about 25,000 kN-m). At the failure roof drift ratio, the moment at the base of the wall  $W_C$  is 4.9 times larger than that of the wall  $W_T$ . This difference is smaller than that observed for the shear forces of the walls in Figure 3- 13b).

The interaction diagram and the moment-curvature relationships of the T-shape wall are constructed to explain the difference of the moment taken by each of the two walls. The interaction diagram of the T-shape wall was constructed using expected material properties (i.e.  $f'_c = 32.5$  MPa and  $f_y = 491.4$  MPa) and is shown in Figure 3- 14a). The axial load level for gravitational loads ( $P_g = 12,500$  kN) is shown in Figure 3- 14a) with a dashed line. For this axial load, the flexural capacity of the wall when the web is in compression ( $M = 9,790$  kN-m) is 2.3 times larger than the flexural capacity of the wall when the web is in tension ( $M = 4,260$  kN-m).

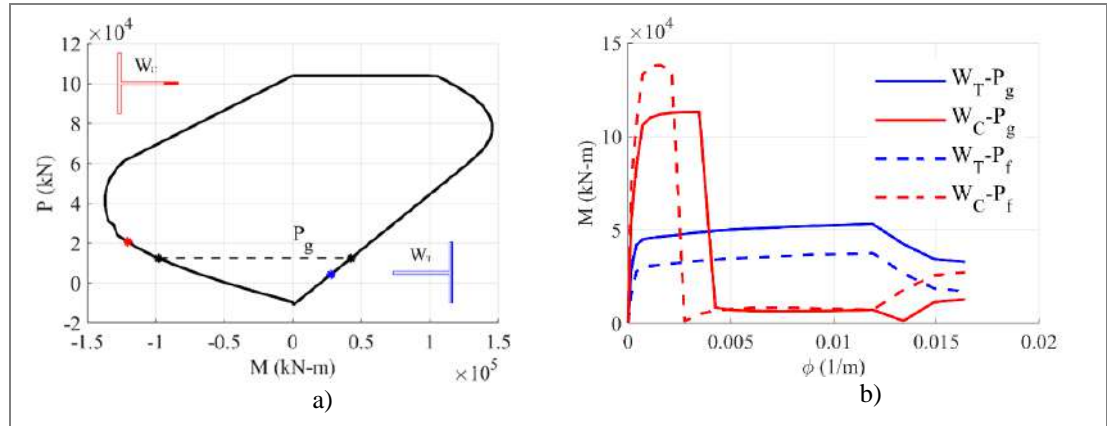


Figure 3- 14: a) Interaction diagram of the T-shape wall and b) Moment-curvature relationships for gravitational axial load and failure axial load in each wall.

Since the ALR of the walls varies significantly when the building is subjected to lateral loads (Figure 3- 13a), the flexural capacity of both walls changes. The flexural capacity of the wall  $W_C$  increases because of the larger axial load, whereas the flexural capacity of the wall  $W_T$  decreases. The predicted axial loads at each wall at failure ( $P_f$ ) are identified in the interaction diagram (Figure 3- 14a) with a red point for  $W_C$  and a blue point for  $W_T$ . The flexural capacity of the wall  $W_C$  for the predicted axial load at failure ( $P_f$ ) is 23% larger than that for the gravitational loads, and the flexural capacity for  $W_T$  (at  $P_f$ ) at failure is 52% lower than that for the gravitational loads. The maximum axial load of wall  $W_C$  (ALR = 0.2,  $P = 22,220$  kN) is reached at a roof drift ratio of 0.64% and the predicted moment at the base is 136,167 kN-m (Figure 3- 13c), which is 10% larger than the flexural capacity (129,775 kN-m) of the  $W_C$  wall for that axial load level (Figure 3- 14a).

Figure 3- 14b) shows the moment-curvature relationships of the T-shape wall considering the two directions of loading. For the wall  $W_C$  the web is in compression and for the wall  $W_T$  the web is in tension. The moment-curvature relationships of the wall were built using Section Designer of SAP 2000 and considering the expected material properties. The Menegotto-Pinto model was used for the constitutive

relationship of the reinforcing steel and the Mander model for both confined and unconfined concrete. The moment-curvature relationships for the gravitational axial loads ( $P_g$ ) are shown in the figure with continuous lines and the relationships for the axial loads at failure ( $P_f$ ) are shown with discontinuous lines. For gravitational axial loads (ALR=0.11), Figure 3- 14b) shows that the flexural strength of  $W_C$  is 2.26 times larger than that of  $W_T$ . If the ALRs at failure are considered (ALR = 0.19 for  $W_C$  and ALR = 0.04 for  $W_T$ ), the flexural strength of the  $W_C$  increases to  $13.8 \times 10^4$  kN-m while for  $W_T$  it decreases to  $3.715 \times 10^4$  kN-m. These variations correspond to a 22% increase and a 43% decrease of the flexural strength for  $W_C$  and  $W_T$ , respectively. Therefore, considering the ALR at failure, the flexural strength of  $W_C$  is 3.71 times larger than that for  $W_T$ . It can be concluded that the difference between the moments at the base of the two walls (Figure 3- 13c) is due to the asymmetric T-shape of the walls and to the variation of the axial loads of the walls, which is generated by the coupling effect of the slabs.

Additional results of the NLS1 model are presented below to further understand the seismic behavior of the building with non-linear slabs. These results correspond to strain demands of walls and slabs. For the walls, the strains of the steel, are obtained from the bars located at 5 cm from the edge of the web and at 49 cm from the flange axis. The strains of the concrete are evaluated at the base of the walls, considering the integration points of the outer finite elements of the web and web-flange intersections. For the slabs of each story, the response is evaluated at the integration points of the finite elements located nearest to the webs of the two walls.

Figure 3- 15 shows the strain demands of the four outer longitudinal bars located at the base of the walls  $W_T$  and  $W_C$ . Two bars are located at the boundaries of the webs of the walls (bars 1 and 4 in Figure 3- 15), and the other two bars are located at the web-flange intersection (bars 2 and 3 in Figure 3- 15). These four bars are embedded in regions of confined concrete. The horizontal dashed lines indicate the yield strain of the steel ( $\epsilon_y = \mp 0.25\%$ ). The figure shows that bar 4, located at the boundary of the

web of the wall  $W_C$  and subjected to compressive strains, is the bar subjected to larger strain demands. Structural failure is identified in bar 4 at a roof drift ratio of 0.78% because the compressive strain reaches the strain limit of 0.008. Failure is identified at this point due to concrete crushing since it is assumed that the strain demand of the concrete is the same as the strain demand of the steel. Bar fracture in tension is not expected since the strain limit of 0.05 is not achieved in any bar. Figure 3- 15 also shows that only one of the four bars is subjected to compression (bar 4 in  $W_C$ ), and the other three bars are subjected to tension.

Yielding in compression is predicted earlier than yielding in tension since yielding in compression is predicted in bar 4 at a roof drift ratio of 0.40% and yielding in tension is predicted in bar 1 at a roof drift ratio of 0.49% (Figure 3- 15). The bars 2 and 3, located at the web-flange intersection, are both subjected to tensile strains, but yielding is predicted only in bar 2 of the wall  $W_C$  at a roof drift ratio of 0.68%. The predicted tensile strains of the bars agree with values reported by previous researchers (Massone et al. 2019) for walls with setback discontinuities. Finally, it is relevant to note that the roof drift ratios for yielding in tension (0.49%) agree with the range of 0.25% - 0.50% drift ratios reported by Thomsen & Wallace (2004) for the bars within the flange of the tested T-shape wall TW2. The reported range indicates a gradual yielding of the tension reinforcement within the flange, with reinforcement closest to the web-flange intersection yielding first and subsequently progressing out from the web-flange intersection as lateral drift levels were increased. The larger compressive strain demands in Figure 3- 15 are attributed to damage localization in compression. Damage localization was also observed in the model of TW2 (Figure 3- 3), but the reported strains in Figure 3- 3c) and Figure 3- 3d) were obtained at the vicinity of the damage localization to be consistent with the measured experimental strains. Further experimental results are required to identify how compressive strains vary along the height in T-shape walls.

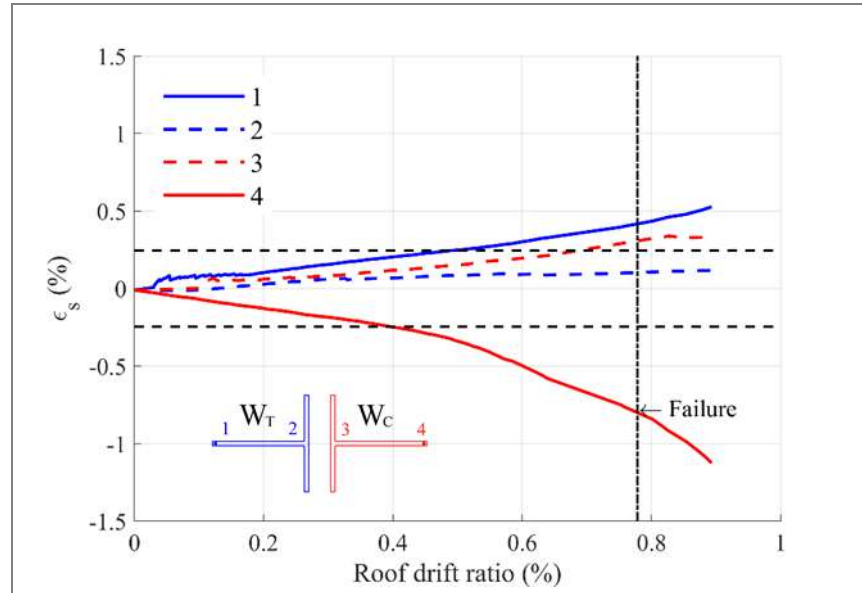


Figure 3- 15: Strain demands in longitudinal bars at the base of the walls in the NLS1 model.

The curvature demands of the two walls at the roof drift ratio of failure can be estimated using the strain demands in the reinforcing steel of the longitudinal bars at the base of the walls (Figure 3- 15). The curvature for the wall W<sub>C</sub> is estimating using  $\phi = (\epsilon_{s_3} + \epsilon_{s_4})/l_w$ , where  $\epsilon_{s_3}$  and  $\epsilon_{s_4}$  are the strain demands of bars 3 and 4, respectively, and  $l_w = 7.3$  m is the horizontal distance between both bars. The curvature demand for W<sub>C</sub> at failure is 0.0015 1/m, which represents 97% of the curvature at maximum flexural capacity and is 28% lower than the curvature where the flexural capacity suddenly decreases (see red dashed line in Figure 3- 14b). It is concluded that at the roof drift ratio at failure, the curvature demand of the wall W<sub>C</sub>, is reaching its flexural capacity.

The gravity loads applied before starting the non-linear static analysis generate compression strains in the longitudinal reinforcement bars of the walls that are not clearly appreciated in Figure 3- 15. Because of that, Figure 3- 16 shows a zoomed view of the strains at the beginning of the non-linear static analysis. The figure shows that

at the beginning of the pushover (i.e. at zero roof drift ratio) the strains of the longitudinal bars corresponds to compressive strains of 0.01 %.

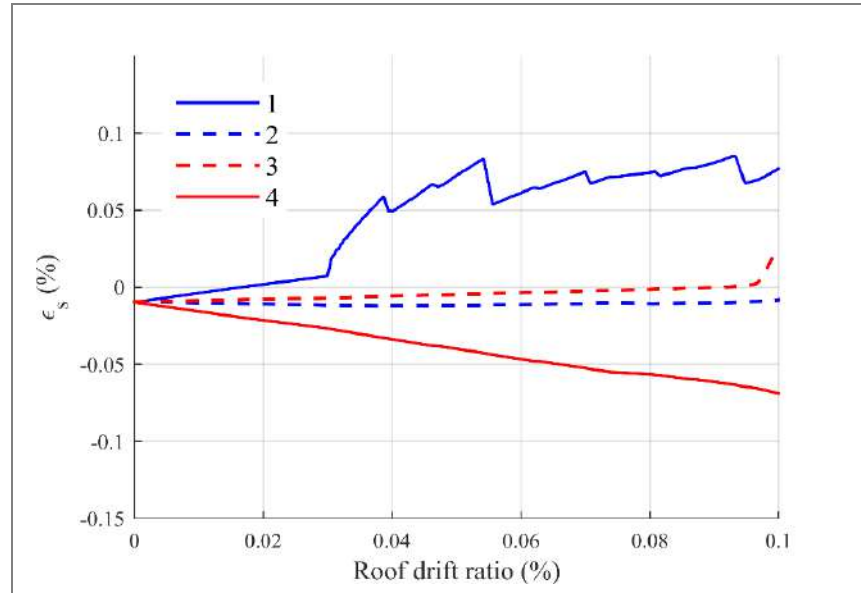


Figure 3- 16: Strains state at the beginning of the non-linear static analysis in longitudinal bars at the base of the walls in the NLS1 model.

Stress-strain relationships of integration points of both concrete and reinforcing steel are presented in Figure 3- 17, at the same locations identified in Figure 3- 15. For the concrete, the compressive response at the integration point 4 in wall  $W_C$  is presented in Figure 3- 17a), which is shown with positive values of both strains and stresses. This figure shows that the concrete reached the maximum compressive strength at a strain of 0.0028 (0.45% roof drift ratio). Beyond that strain, the figure shows that the concrete strength is slightly reduced until the compressive strain limit of 0.008 is reached at a roof drift ratio of 0.78%. The stress-strain relationships of the tensioned bars (1, 2, and 3) are shown in Figure 3- 17b). The presented results reaffirm the previous observations from Figure 3- 15, where yielding in tension is predicted in bars 1 and 3 of  $W_T$  and  $W_C$ , respectively, and no yielding is predicted in bar 2 of  $W_T$ .

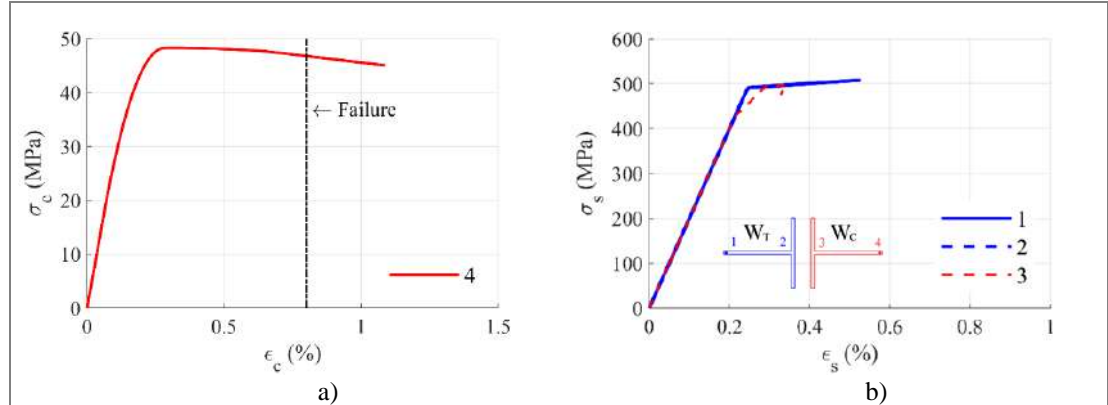


Figure 3- 17: Stress-strain relationships in the longitudinal direction at the base of the walls, NLS1 model: a) Concrete in compression and b) Steel in tension

Figure 3- 18 shows the strain demands of the slab reinforcement at each story for the NLS1 model. The strain demands after applying the gravity loads (i.e., roof drift ratio of 0% in Figure 3- 18) are negligible. The figure shows the strains at the integration points located nearest to the wall webs in each story. Figure 3- 18a) presents the strains of the bottom reinforcement grid closest to  $W_T$ , and Figure 3- 18b) of the top reinforcement grid nearest to  $W_C$ . When the building sways towards the right, tensile strains (i.e., positive strains) are expected in both locations. The figure also shows the yield strain and the roof drift ratio at failure. Both figures show an abrupt strain increment at a roof drift ratio of about 0.1%, which is attributed to the cracking of the slabs. Yielding of the slab reinforcement is initiated at the top reinforcement of the slab of the 13<sup>th</sup> story at a roof drift ratio of 0.25%. The yielding of the slabs is registered before the yielding of the walls, which was registered at a roof drift ratio of 0.40% (Figure 3- 15). For the roof drift ratio at failure, Figure 3- 18b) shows that the top reinforcements of the slabs of all stories are yielding, except the ones of the first and second stories. Additionally, the bottom reinforcement of the first story is the only one which does not yield (Figure 3- 18a). Figure 3- 18 also shows that the maximum strain demand predicted in the slab for the roof drift ratio at failure is significantly lower than that of steel fracture (5%). Compressive stains of the slabs reinforcement (not shown

in Figure 3- 18) were lower than 0.10%, which allows concluding that the surrounding unconfined concrete does not reach the crushing strain limit of 0.50%.

Finally, yielding was identified in different slab elements located near the ends of the flanges of the walls (not shown in Figure 3- 18). This result implies that the slabs yield along the whole wall flange width, which agrees with the findings of Zhang et al. (2017). These authors reported the formation of a longitudinal yield line on each side of the central corridor of a Chilean building subjected to non-linear static and dynamic analyses.

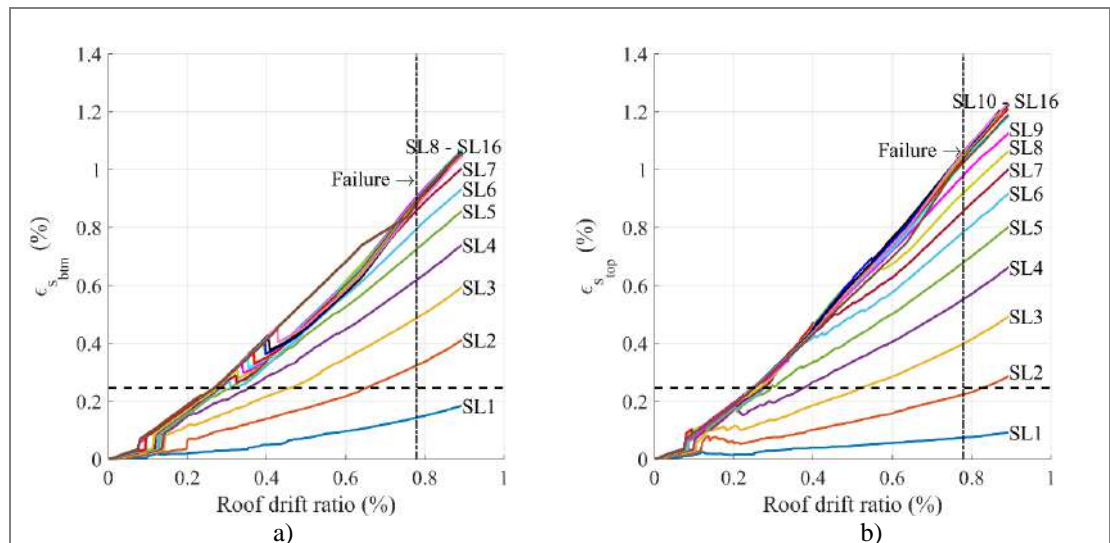


Figure 3- 18: Strain demands of slab reinforcement at each story for a) bottom grid nearest to  $W_T$  and b) top grid nearest to  $W_C$ .

### 3.6 Effect of slab reinforcement

This section describes the effect of the reinforcement ratio of the slabs on the seismic response of the case study building. The global and local responses obtained from the models NLS1, NLS2, and NLS3, are compared. Table III- 4 and Figure 3- 19 compare the general response of the structure for the three models (NLS1, NLS2, and NLS3).

The results for each model are shown until convergence is achieved, and the structural failures are pointed for each building. The figure shows that the maximum strength of the building increases as the slab reinforcement increases. The maximum strengths of the models NLS2 and NLS3 predicted at the end of the analysis are 17% and 14% larger than that of the NLS1 model ( $0.29 W$ ). Additionally, Figure 3- 19 shows that the roof drift ratio at failure decreases as the slab reinforcement increases. The roof drift ratios at failure for models NLS2 and NLS3 are 15% and 20% lower than that predicted for the model NLS1 (0.78%). Additionally, the predicted roof drift ratio at failure is 2.13 and 2.03 times larger than the design displacement of 0.31% ( $\delta_u$  in Figure 3- 19) for the model NLS2 and NLS3, respectively.

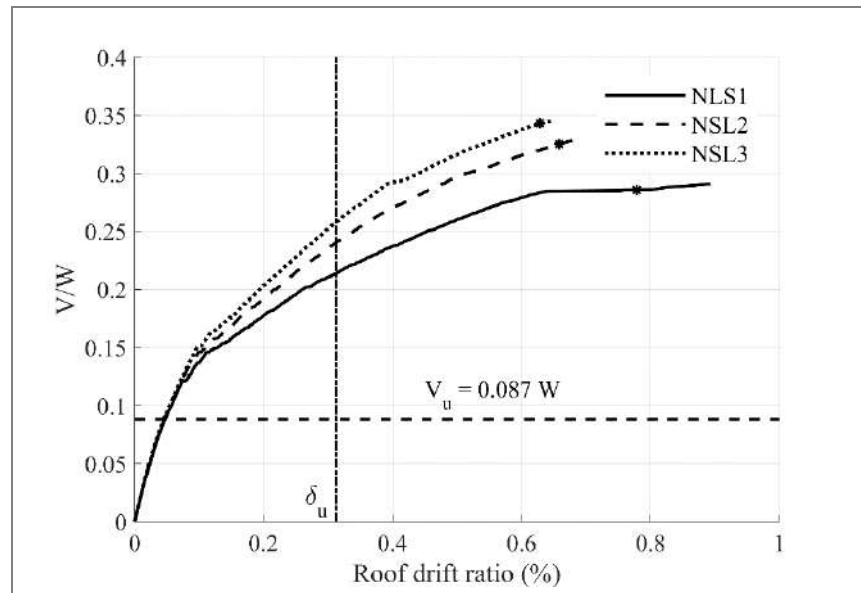


Figure 3- 19: Non-linear static analysis results for NLS1, NLS2 and NLS3 models. Structural failure is marked with dots.  $\delta_u$  is the design displacement according to the DS61 (0.31%) and  $V_u$  the ultimate shear design (0.0087W).

Table III- 4: Strength, overstrength factor, deformation capacity and parameters of the idealized bi-linear constitutive, NLS1, NLS2, and NLS3 models.

	NLS1	NLS2	NLS3
$V_{\max}$ (W)	0.291	0.328	0.345
$V_{\text{failure}}$ (W)	0.286	0.325	0.343
$\Omega_o$	3.34	3.78	3.96
$\delta_{\text{failure}}$	0.78%	0.66%	0.63%
$\delta_{\text{failure}}/\delta_u$	2.52	2.13	2.03
$\delta_y$	0.096%	0.108%	0.110%
$V_y$ (W)	0.168	0.185	0.191
$\alpha$	0.142	0.189	0.208

The idealized bi-linear constitutive relationship of each model was obtained according to FEMA-273 (FEMA 1997) recommendations and are presented in Figure 3- 20. The bi-linear relationships are used to estimate the effective lateral stiffness ( $K_e$ ) and the yield strength ( $V_y$ ), of each building. The stiffness  $K_e$  corresponds to the secant stiffness at a base shear force of  $0.6V_y$ , and  $\delta_y$  is the yield drift of the bi-linear relationship. The ratio between the second slope of the idealized constitutive and the effective lateral stiffness is defined as  $\alpha$  and is listed in Table III- 4. The increase of  $\alpha$  indicates that the post-yield stiffness of the structure increases as the slab reinforcement increases. Nevertheless, the effective lateral stiffness of the three buildings are similar and the values of yield strength of NLS2 and NLS3 models are 9.8 and 14% higher than that of the NLS1 model, respectively.

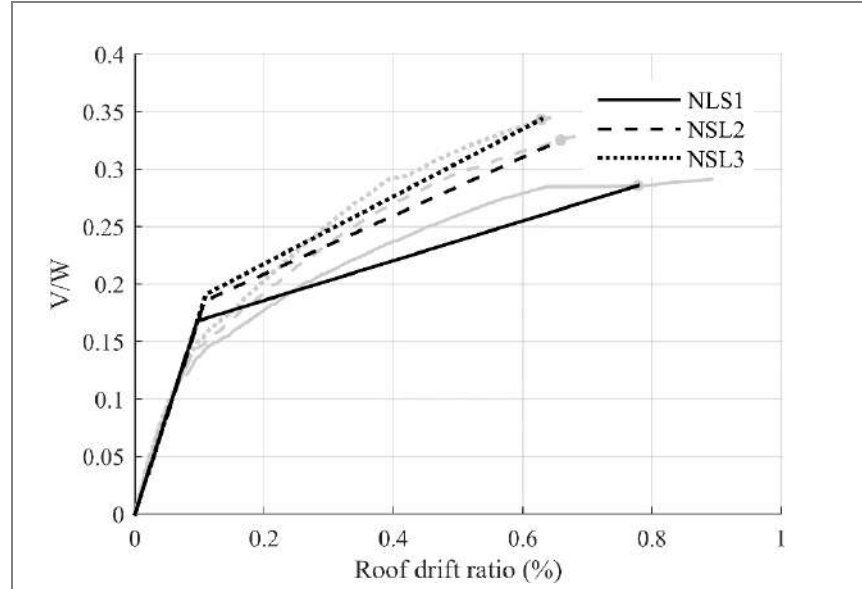


Figure 3- 20: Idealized bi-linear constitutive relationships for NLS1, NLS2, and NLS3 models.

The comparison of the axial load ratios, shear force, and bending moment at the base of the two walls predicted with the models NLS1, NLS2 and NLS3 are presented in Figure 3- 21. Again, blue lines show the results for the wall in tension ( $W_T$ ), red lines for the wall in compression ( $W_C$ ), and the dashed grey line is the gravitational ALR. The responses of the different models are shown with different types of lines, and the failure of each model is marked with dots. Figure 3- 21a) shows that the variation of the ALR increases as the slab reinforcement increases. The predicted ALRs at failure for the wall  $W_C$  are 0.19, 0.23, and 0.24 for the models NLS1, NLS2, and NLS3, respectively. Therefore, the predicted maximum ALR increases 27% when the reinforcement of the slabs is increased from  $\rho = 0.002$  in model NLS1 to  $\rho = 0.006$  in model NLS3.

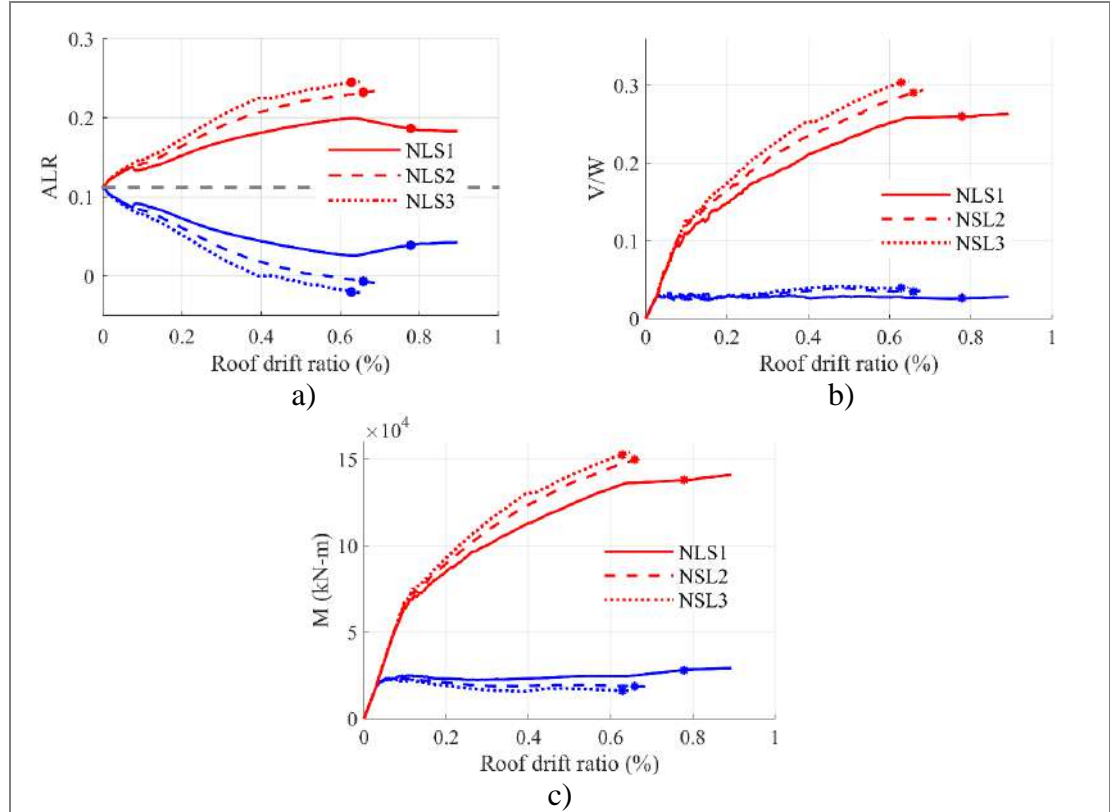


Figure 3- 21: Comparative result for NLS1, NLS2, and NLS3 for the a) Axial load between tensioned and compressed wall; b) Distribution of normalized base shear force and c) Distribution of moment at the base of each wall.

Regarding the shear distribution between the two walls, Figure 3- 21b) shows that the shear force taken by the wall in compression ( $W_C$ ) increases as the slab reinforcement increases. Additionally, the shear force resisted by the wall  $W_C$  at failure for the models NLS2 ( $0.29W$ ) and NLS3 ( $0.30W$ ), are 8% and 13% larger than that obtained for the model NLS1. The percentage of the base shear held by  $W_C$  at the roof drift ratio of failure decreases as the slabs reinforcement increases. The portion of the total base shear resisted by the wall  $W_C$  is 89% and 88% for the models NLS2 and NLS3, respectively, whereas the base shear resisted by the wall  $W_C$  for the model NLS1 is 91%.

Figure 3- 21c) shows that the bending moment at the base of the wall  $W_C$  increases as the slab reinforcement increases. For the roof drift ratio at failure, the predicted moments in  $W_C$  are  $1.38 \times 10^5$  kN-m,  $1.49 \times 10^5$  kN-m, and  $1.53 \times 10^5$  kN-m for the models NLS1, NLS2, and NLS3, respectively. The base moments predicted with the models NLS2 and NLS3 are 8% and 11% larger than that from the model NLS1. Figure 3- 21c) also shows that the moment at the base of the wall  $W_T$  decreases as the slab reinforcement increases. The moments predicted at the base of  $W_T$  for the models NLS2 and NLS3 are 33% and 42%, respectively, smaller than that for the model NLS1. The variations of the moments predicted at the base of the walls were expected because of the variation of the axial loads in models NLS2 and NLS3, which affects the strength of the T-shape walls (Figure 3- 14a).

The comparison of the degree of coupling predicted with the models NLS1, NLS2 and NLS3 is presented in Figure 3- 22. As expected, the figure shows that in general, the doc increases as the slab reinforcement increases. Larger reinforcement in the slabs induces larger coupling axial loads transferred to the walls and then larger doc. For roof drift ratios smaller than 0.10%, the three models trends show different values of the doc. Models NLS1 and NLS2 show minimum values of 13.7% and 17.4%, and model NLS3 reached the minimum value of 20.3%. For roof drift ratios larger than 0.10%, the doc of the three models increases gradually, until relatively constant values of about 26%, 31% and 33% for the NLS1, NLS2 and NLS3 models, respectively. At failure, the degree of coupling for the models NLS2 (31.3%) and NLS3 (33.5%) are 40% and 50% higher than that obtained for the NLS1 model (22.2%).

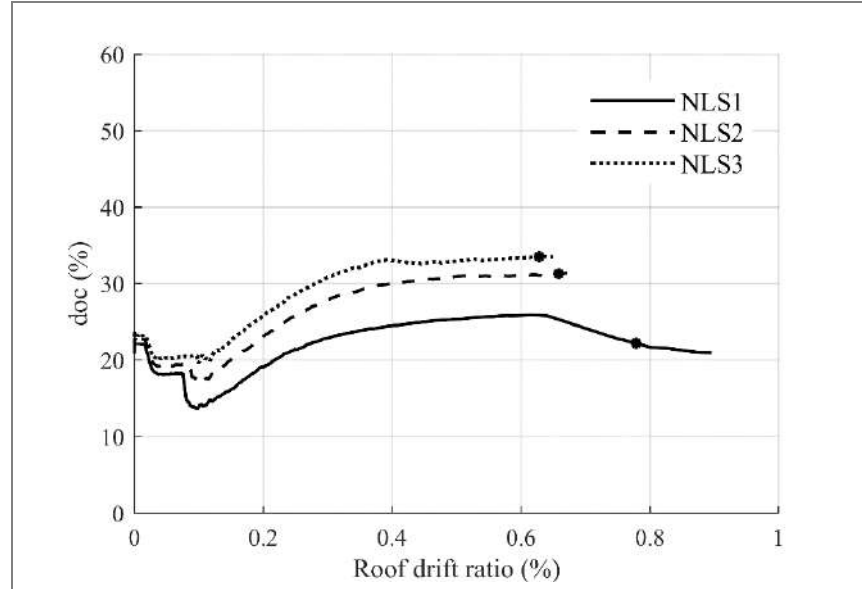


Figure 3- 22 Degree of coupling for the NLS1, NLS2, and NLS3 model.

The strain demands of the critical bars (bars 1 and 4 in Figure 3- 15) at the base of the walls  $W_T$  and  $W_C$  predicted with the models NLS1, NLS2 and NLS3 are shown in Figure 3- 23. Blue lines show the results for bar 1 of the wall  $W_T$ , and red lines show the results for bar 4 for the wall  $W_C$ . The responses of the different models are shown with different types of lines, and the failure is identified with dots. The figure shows that the yielding of the bars in tension and compression is predicted at similar roof drift ratios for the three models (i.e., roof drift ratio of about 0.4%). After yielding, different strain demands are predicted for the models. Figure 3- 23 shows that the compressive strain demand of bar 4 in the  $W_C$  reaches the failure strain (i.e., 0.008) earlier when the reinforcement ratio of the slabs increases. The larger flexural strength of the coupling slabs in models with a larger slab reinforcement ratio increases the axial load demand in the wall  $W_C$ , which increases the strain demand.

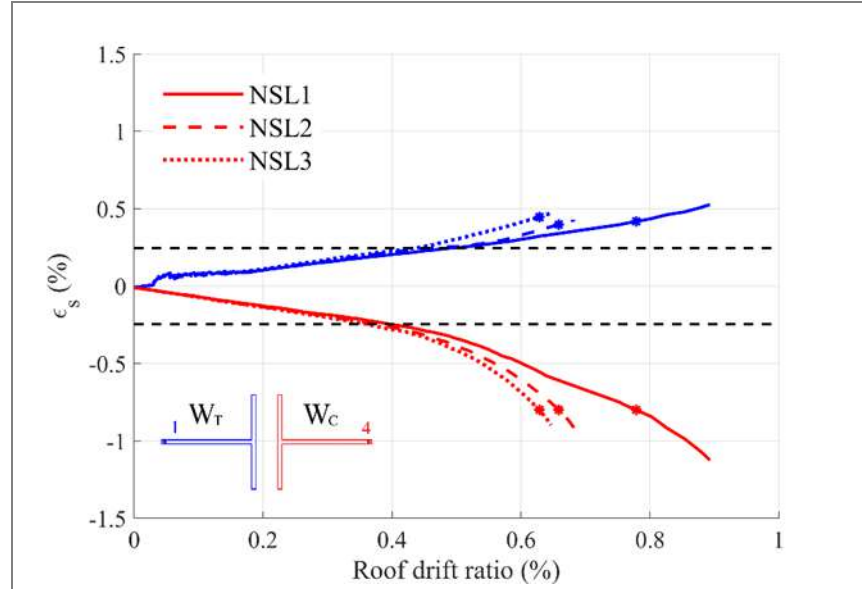


Figure 3- 23: Strain demands in most demanded longitudinal bars at the base of the walls, models NLS1, NLS2 and NLS3.

Figures Figure 3- 24a) and Figure 3- 24b) show the strain demands of the top reinforcement grid of the slabs for the models NLS2 and NLS3. Equivalent to Figure 3- 18, Figure 3- 24 shows the strains in each story at the integration points nearest to the wall webs. The legends in these figures are organized following a decreasing order from the greatest to least demanded slabs. It is evident in both models (NLS2 and NLS3) that the slab of the ninth story is the most demanded one, but the maximum strain predicted for the model NLS2 (0.602 at failure) is 32% higher than that for model NLS3 (0.407). However, these strains are smaller than the largest strain demand (1.06) predicted for story 14 at failure for model NLS1 (Figure 3- 18b). Finally, Figure 3- 24 shows that for the roof drift ratio at failure, the slabs from stories 4 to 16 yield in the model NLS2, whereas the slabs from stories 5 to 15 yield in the model NLS3.

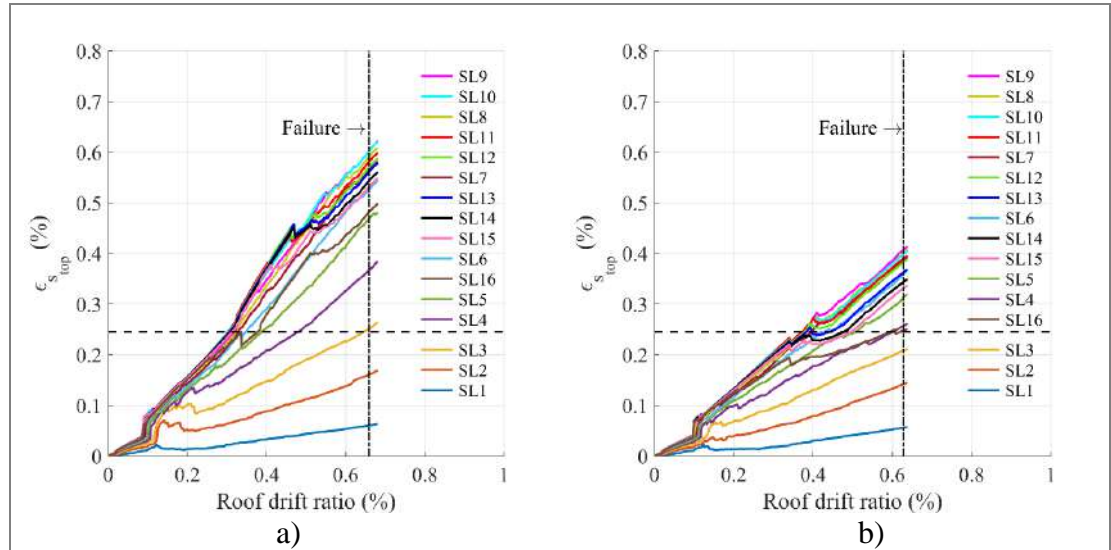


Figure 3- 24: Strain demands of slabs reinforcement at each story for top grid in a) NLS2 model and b) NLS3 model.

## **4. DYNAMIC ANALYSIS OF RC WALL BUILDING WITH NON-LINEAR COUPLING SLABS**

### **4.1 Introduction**

The previous section assessed the coupling effect of the slabs in the response of the case study building using non-linear static analysis. Aimed to validate those previous results, the case study building is subjected to non-linear dynamic analysis. The same model (NLS1) is used to conduct time history analyses using one horizontal component of three seismic records already used in chapter 2 of this thesis. The model NLS1 considers non-linear behavior for both walls and slabs, and the slabs are modeled with a top and bottom reinforcement ratio of  $\rho = 0.002$ . The global seismic response of the case study building is evaluated in this section from roof displacements and forces at the base of the walls (axial load, shear, and bending moment). Additionally, the degree of coupling is evaluated. Finally, the effect of the slab reinforcement in the dynamic response is analyzed using models NLS2 and NLS3 models with varying reinforcement ratio.

### **4.2 Ground motions and analysis considerations**

One of the horizontal component of three ground motions recorded in Santiago during the 2010 Chile earthquake are selected to conduct the dynamic analyses. The three seismic records used are: Santiago Peñalolen (SN) north-south, Santiago Centro (SC) east-west, and Santiago Puente Alto (SPA) east-west. The displacement response spectrum of the records are shown in Figure 2-4. Because of the computational storage limitations and the amount of computational time, only the significant duration of the seismic records, between 5% and 95% of the Arias Intensity (Arias 1970), was considered. The seismic records and their significant duration (in black) are shown in Figure 4- 1. The significant durations of the SN, SC and SPA seismic record are 42s, 34.5 s and 38.5 s, respectively.

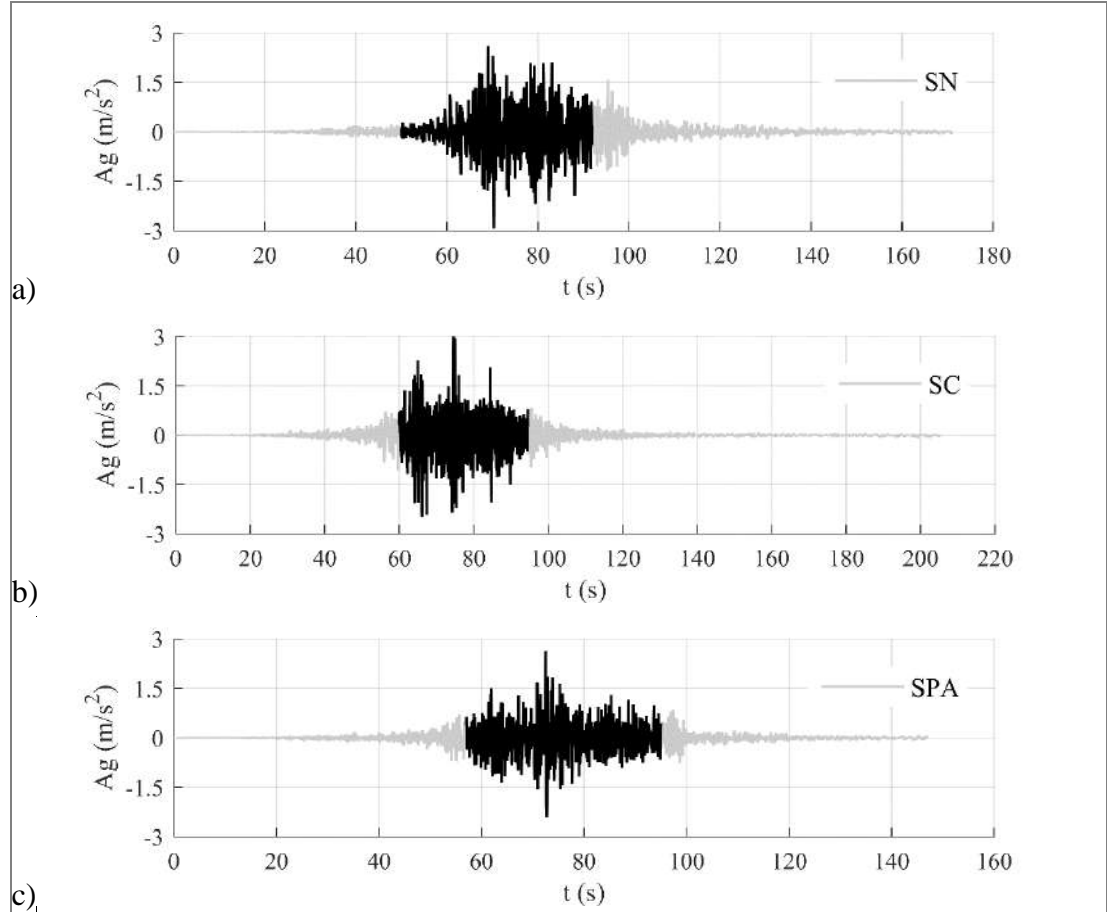


Figure 4- 1: Ground motions and significant duration of the seismic records at station a) SN; b) SC and c) SPA.

The component of each record was applied in the positive Y-direction of the case study building (Figure 3- 1) which is the direction considered in the non-linear static analysis in the previous section. Rayleigh damping was assumed in the model with 5% of the critical damping at the first and second modes of the structure. This damping ratio is larger than the 3% damping ratio used by (Vasqu ez et al. 2020) in a similar building because the model with 3% damping ratio had earlier convergence problems. However, the relevant results from the dynamic analyses for this study are not related to the maximum response of the building, but rather to the coupling behavior. The constants proportional to the mass and stiffness of the Rayleigh damping are  $a = 0.8987$  1/s and  $b = 0.0017$  s, respectively.

The dynamic analyses were conducted using the Newmark integration method with constant acceleration response in each time step (Chopra 2016). The gamma and beta factors of the Newmark method are 0.25 and 0.5, respectively (Chopra 2016). Regular Newton-Raphson iterations were used to obtain convergence in each time step, and the tangential stiffness is used at each sub-iteration. The mass matrix is specified as consistent and does not include the rotational terms. The damping matrix is defined as consistent and uses the current stiffness matrix to define Rayleigh damping. The time step used for the integration is defined invoking a cutback-based automatic time incremental algorithm, which uses the SDIRK2 adaptive time step strategy available in DIANA (TNO DIANA 2017) with a minimum step size  $1e-07$  s and a maximum step size of 0.0085 s. SDIRK2 applies a time integration error control through a second order Runge-Kutta method. In that method, the error is evaluated as the difference between two consecutive solutions of the integration method. The criteria of relative and absolute tolerance for the error are used to reject the time step and estimate the next time step.

### **4.3 Dynamic response of the building with non-linear slabs**

This section presents and describes the dynamic response of the case study building predicted with the NLS1 model for the three ground motions. First, the displacement response of the building is obtained. Second, the base shear response of the building is assessed. Third, the response of the axial load, base shear and moment at the base of each wall is evaluated. Finally, the degree of coupling is computed for each seismic record.

Because of the significant non-linear behavior, convergence problems occurred in the analyses and the response was not obtained for the complete significant duration for the three earthquakes. However, the obtained response allows drawing conclusions of

the behavior of the case study building. Moreover, for two ground motions (SN and SPA), the convergence problem occurred after the peak ground accelerations.

The roof displacement responses (shown as roof drift ratio) of the case study building, obtained for the NLS1 model and the three seismic records, are shown in Figure 4- 2. The X-axis of the plots was set with a range of time to show the significant duration of the three seismic records. The responses of the NLS1 model are shown until convergence was achieved. The figure also shows the roof displacement considering an elastic behavior. The elastic responses were obtained from DIANA models similar than the NLS1 model, but with linear material properties for both concrete and steel. The points marked over the response of the NLS1 model in Figure 4- 2 are used later to assess the behavior of the building at such time steps.

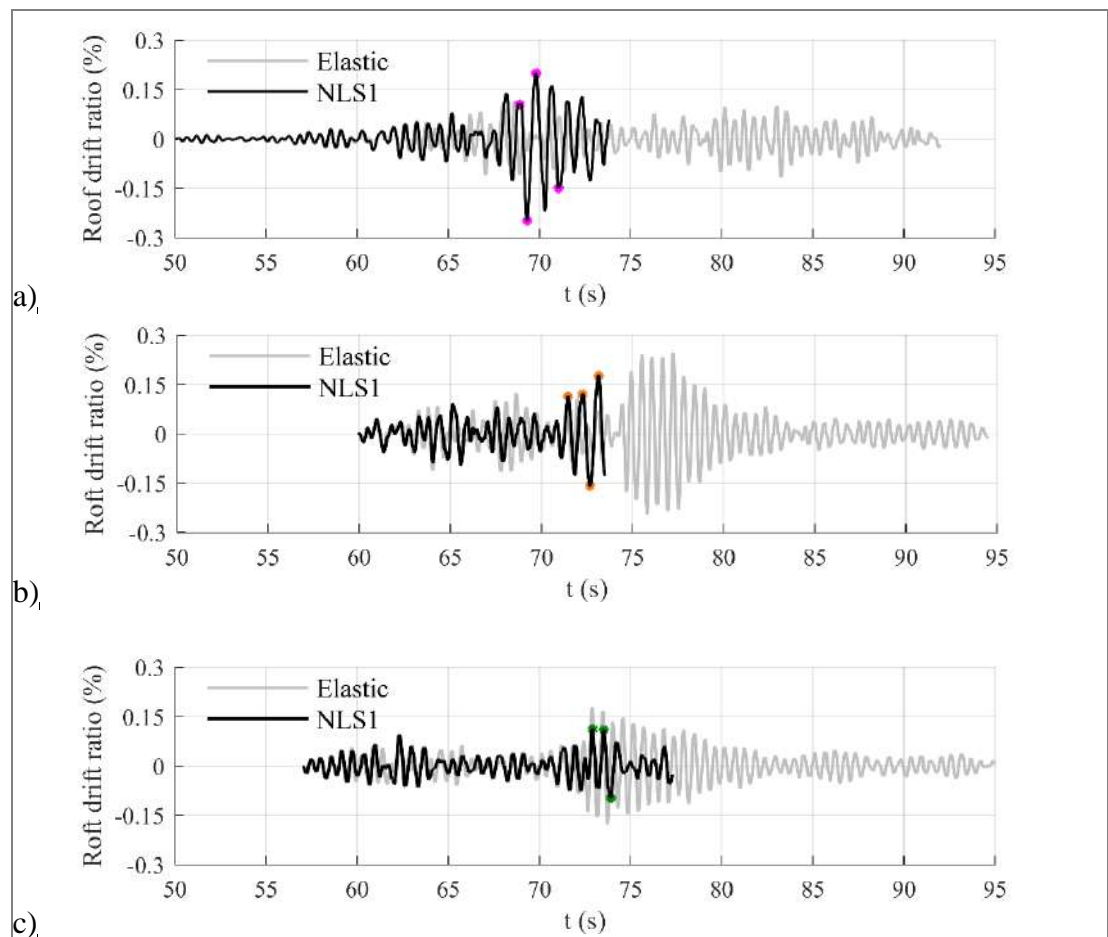
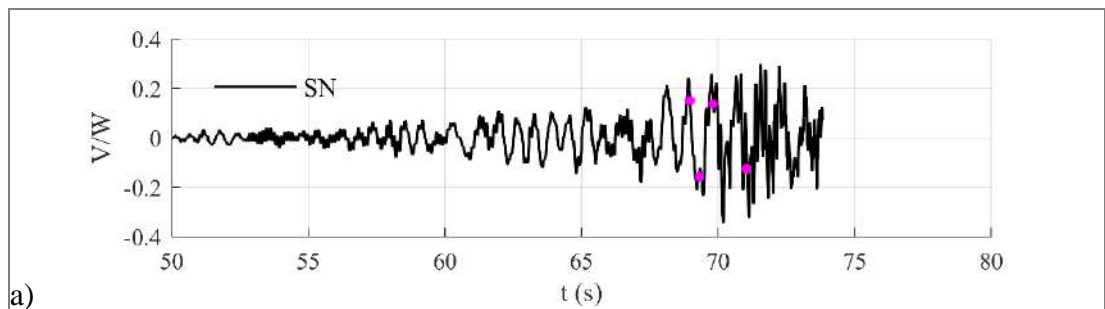


Figure 4- 2: Roof drift ratio of the study case building predicted with NLS1 model and an elastic model for seismic records: a) SN; b) SC and c) SPA.

Figure 4- 2 shows that for the first cycles of the three records, the displacements of the NLS1 models are almost equivalent to the displacements of the elastic model. For subsequent cycles, the displacements of the NLS1 models start to differ from those of the elastic models. Vásquez et al. (2020) obtained similar results when comparing the dynamic response of a building using linear and non-linear models. The maximum roof drift ratio obtained for the elastic models is 0.25% when it is subjected to the SC seismic record. The maximum roof drift ratio obtained for the NLS1 model is 0.25% when it is subjected to the SN seismic record. This maximum displacement occurs at 69.32 s of the seismic record, and does not match with the time of any of the acceleration peaks of the SN ground motion (peak acceleration of SN occurs at 70.35 s). The maximum roof drift ratios of the NLS1 model obtained for the other ground motions are 0.18% and 0.11% for the seismic records SC and SPA, respectively..

The total normalized base shear obtained for the three seismic records are presented in Figure 4- 3. Aimed to improve the visibility of the results, the time axes of these plots are shown with 10 s less than that shown in the

Figure 4- 2. The base shear values predicted at the peak displacement points identified in Figure 4-2 are marked with dots of the same colors in Figure 4- 3. It can be identified that the points of maximum roof displacements does not correspond to the points of maximum base shear. The maximum predicted values of total base shear with SN, SC, and SPA seismic records are 0.34W, 0.26W, and 0.30W, respectively.



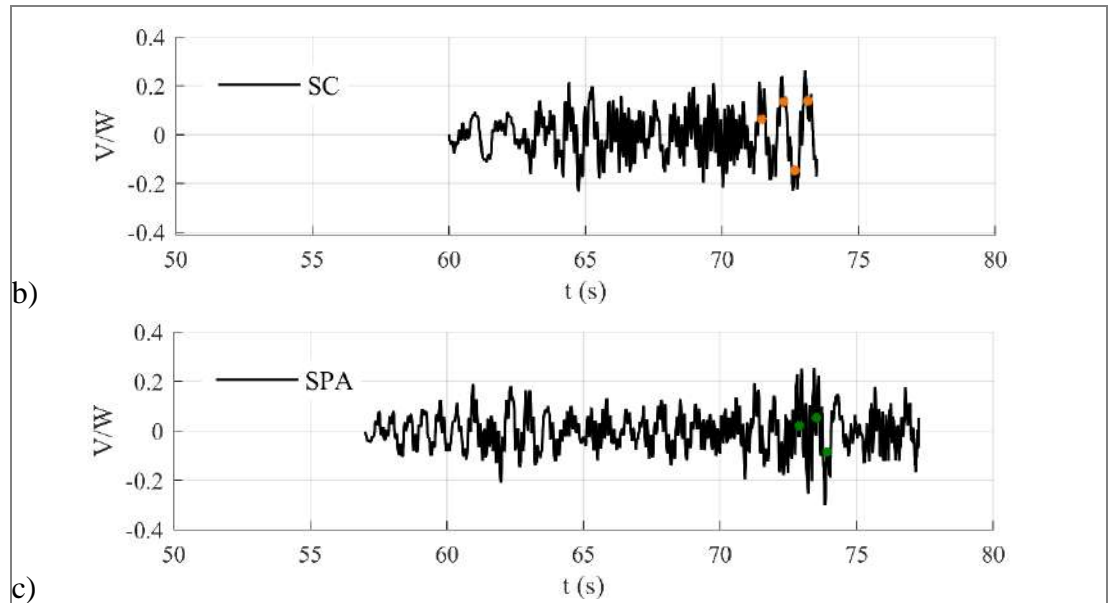
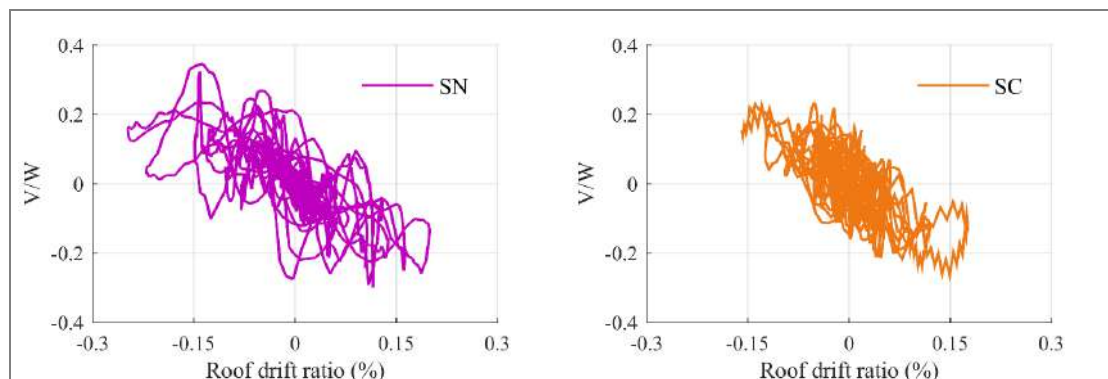


Figure 4- 3: Normalized total base shear ( $V/W$ ) predicted with NLS1 model and seismic records: a) SN; b) SC and c) SPA.

The hysteretic responses of the roof displacement and base shear of the case study building, for the three seismic records, are shown in Figure 4- 4. Again, the figure shows that the maximum values of base shear occur at different instants than those of the maximum roof drift ratios. For example, for the SN ground motion, the maximum base shear is 53% greater than the base shear at the instant of maximum roof drift ratio. For the SC and SPA seismic records, the maximum base shear are 46% and 93% greater than those at the instant of maximum roof drift ratio, respectively.



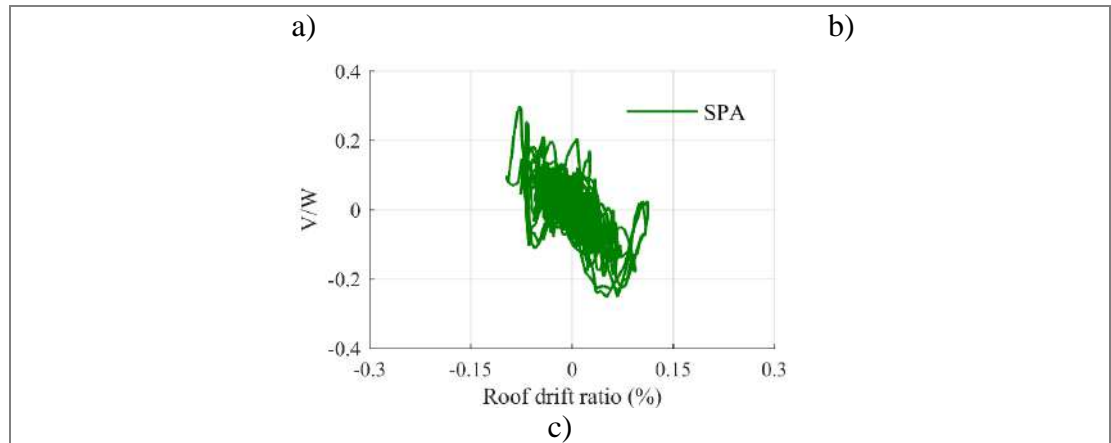


Figure 4- 4: Hysteretic response of the base shear and roof displacements of the case study building, for the seismic records: a) SN; b) SC, and c) SPA

Figure 4- 5 shows the response of the ALR for the two T-shaped walls of the NLS1 model, for the three seismic records. The markers in Figure 4-5 corresponds to the values of ALR predicted at the same time steps of peaks displacements identified in Figure 4- 2. The left wall of the floor plan is named  $W_L$ , and the right wall  $W_R$ . Blue lines in Figure 4- 5 shows results for  $W_L$  and red lines for  $W_R$ . At the beginning of the three ground motions, the figure shows that the ALR of the two walls are the same, and are equal to 0.11, which corresponds to the gravitational ALR. The responses for the rest of the time follows the same trend observed for the non-linear static analysis, where the ALR in one wall increases and the ALR in the other wall decreases. The maximum values of the ALR predicted for the walls are 0.17 for the SN seismic record, and 0.16 for both the SC and SPA seismic records. The maximum ALRs are predicted at time steps close to those of the peak displacement, except for the SN seismic record, where the maximum ALR is predicted at 70.29s.

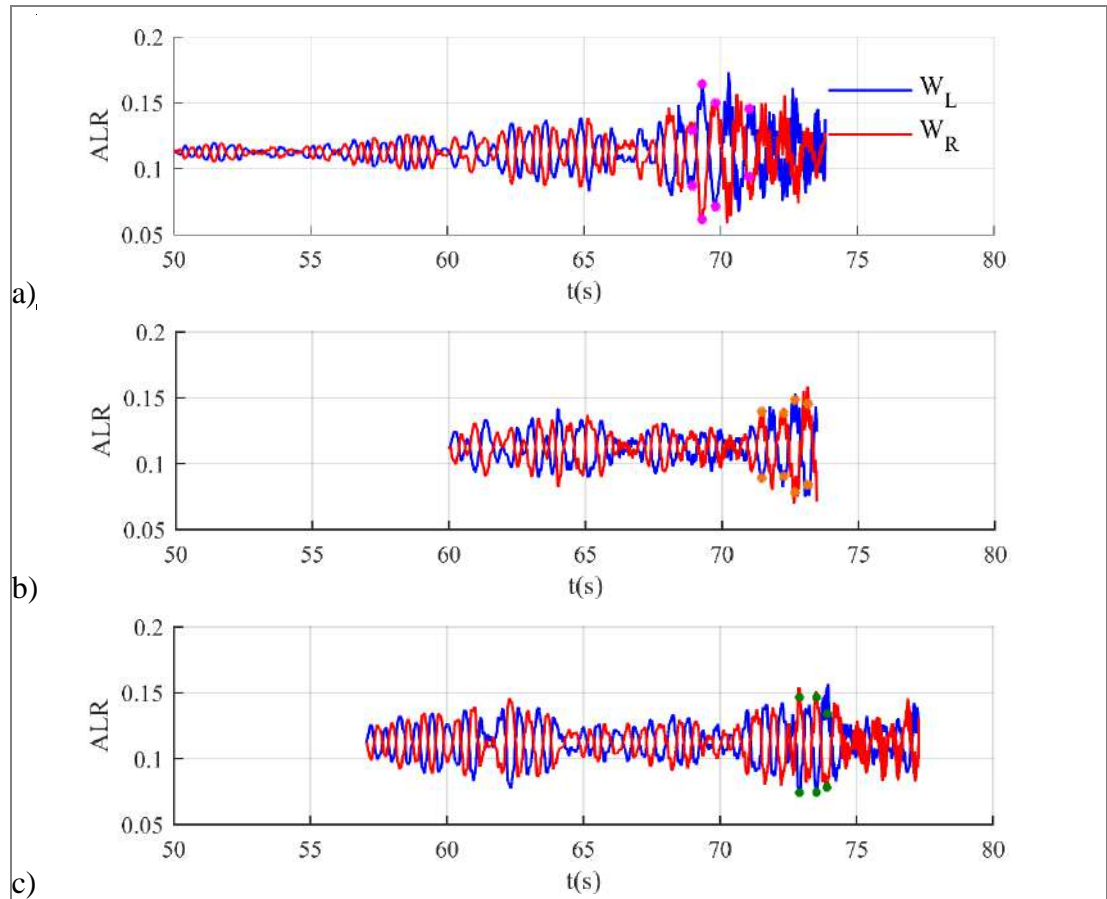


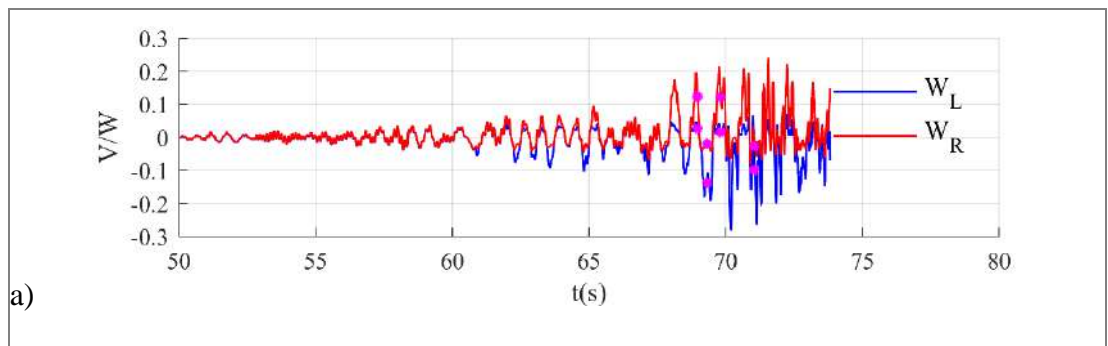
Figure 4- 5: Axial load ratio at the base of each wall predicted with for the NLS1 model for seismic records: a) SN; b) SC, and c) SPA.

The Figure 4- 5 showed that the seismic ALR of each wall vary significantly during time, with respect to the initial gravitational ALR. Table IV- 1 of ALR, Table IV- 1 lists the ALR predicted with the three seismic records at similar roof drift ratios (about 11%). The table shows that those ALRs ( $ALR_{11}$ ) varies from 12.93% to 14.67%, which corresponds to an increase of the ALR (from the gravitational axial load ratio) between 18% and 33%.

Table IV- 1: ALRs predicted with the three seismic records at similar roof drift ratios.

Seismic record	Drift (%)	ALR <sub>11</sub> (%)	ALR <sub>11</sub> /ALR <sub>grav</sub>
SN	0.106	12.93	1.18
SC	0.114	13.95	1.27
SPA	0.109	14.67	1.33

The distribution of the base shear between the two walls, for the three seismic records, is shown in Figure 4- 6. The points with peak roof drift ratios identified in Figure 4.2 are also marked in this plot. The figure shows that for shear forces lower than 0.03W the difference between the shear forces withstood by the two walls is negligible. For larger shear forces, the difference between the shear forces withstood by the two walls is considerable. The predicted trend is similar to the one observed in the non-linear static analysis, where most of the base shear is taken by the wall that is compressed due to the seismic action while the shear force in the other wall reaches a limit of about 0.05W. Finally, the maximum base shear forces predicted for one individual wall are 0.28W, 0.22W, and 0.25W for the SN, SC, and SPA seismic records, respectively. Those forces values correspond to 82%, 85%, and 83% of the total base shear predicted for the entire structure.



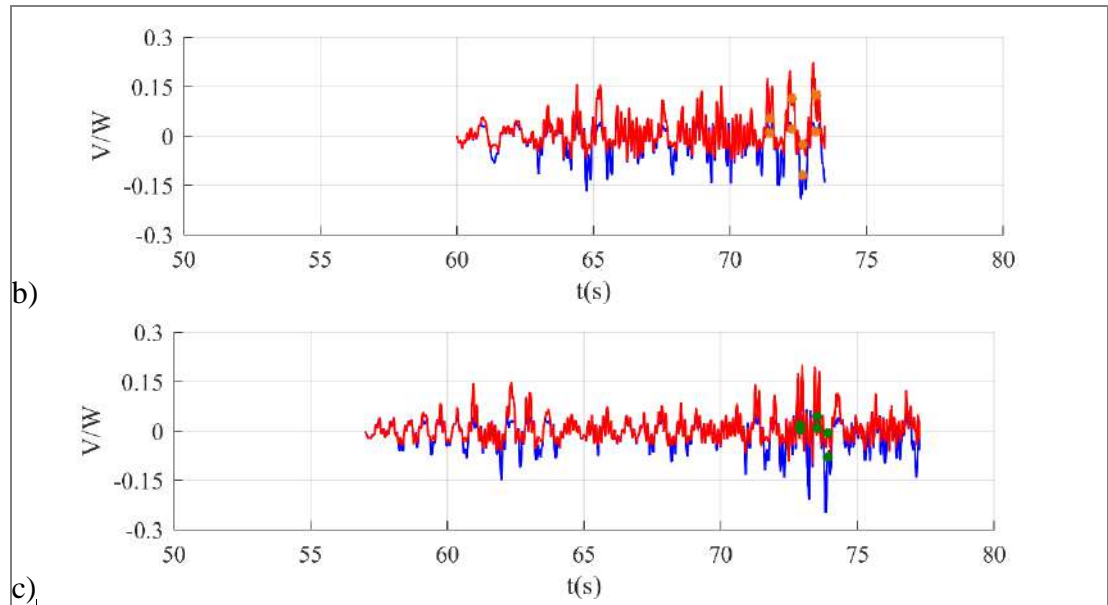


Figure 4- 6 Normalized total base shear ( $V/W$ ) at the base of each wall predicted with NLS1 model and seismic records at stations: a) SN; b) SC and c) SPA.

Figure 4- 7 shows the response of the bending moments at the base of the two walls, for the three seismic records. The observed response is similar to the response predicted by the non-linear static analysis, and similar to the response of the shear forces of the walls. For bending moments lower than about 18,900 kN-m, the predicted moments at the base of the two walls are identical. For larger values, the moment at the base of the wall subjected to tension seismic forces remains almost constant while, the moment at the base of the other wall increases. For example, at 69.32 s of the SN seismic record, the moment of  $W_L$  is 90,300 kN-m and the moment of  $W_R$  is only 21,100 kN-m. For the next peak at 69.81 s the moment of  $W_L$  is 21,700 kN-m and the moment of  $W_R$  is 85,500kN-m.

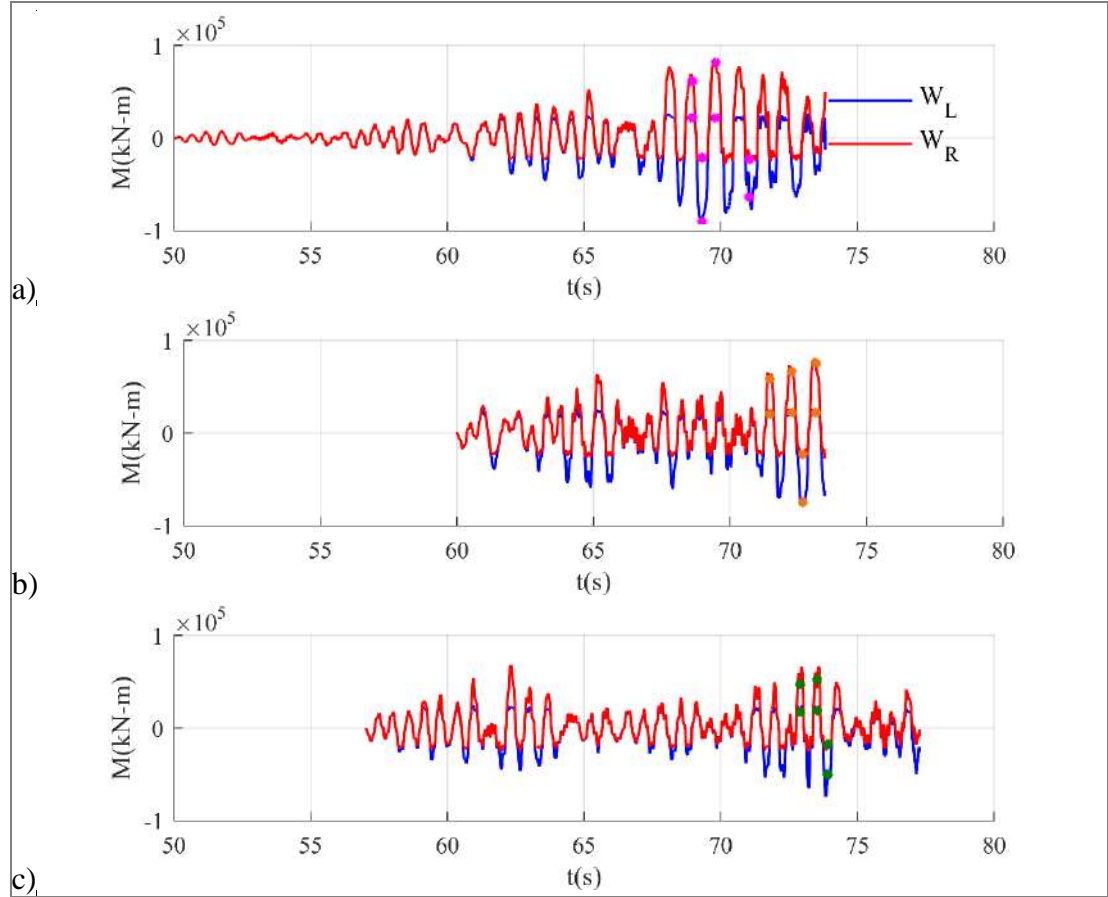


Figure 4- 7: Moment at the base of each wall predicted with NLS1 model and seismic records at stations: a) SN; b) SC and c) SPA.

#### 4.4 Comparison between the dynamic and the static response

This section compares the response of the case study building predicted with the NLS1 model from the non-linear dynamic analyses and the non-linear static analysis. For this comparison, the peak roof displacements of the dynamic analyses (pointed in Figure 4- 2) and the corresponding forces (base shear, axial load, bending moment) predicted at those peaks, are plotted jointly with the response of the static analysis showed in Section 3.

First, the static and dynamic roof displacement responses of the structure are compared. Table IV- 2 summarizes the maximum roof drift ratios and the corresponding base shear forces obtained by the three dynamic analysis. Figure 4- 8 compares these points (marked with circles) with the static analysis results. It can be observed that the maximum roof drift ratios predicted by the dynamic analysis remains in the elastic range of the structure capacity curve. The maximum roof drift ratio predicted by the dynamic analyses was 0.25% for the SN seismic record. This roof drift ratio represents only 32% of the roof drift ratio of failure predicted by the static analysis.

Table IV- 2: Maximum roof drift ratios and corresponding base shear forces predicted with the three seismic records

Seismic record	Max roof drift ratio (%)	Time step (s)	V/W
SN	0.25	69.32	0.16
SC	0.18	73.14	0.14
SPA	0.11	72.91	0.02

On the other hand, it was mentioned in the previous section that base shear forces higher than those predicted at the time step of peak displacements were registered for the dynamic analyses. Table IV- 3 lists those maximum shear forces, the corresponding roof drift ratios, and time steps where those forces were predicted. Those shear forces are plotted with triangles in Figure 4- 8. It can be observed that the dynamic maximum base shears are larger than the shear forces predicted by the static analysis at the corresponding roof displacements. The larger difference was obtained for the dynamic response with the seismic record SN, where the dynamic shear force of 0.35 V/W at a roof drift ratio of 0.14% is 233% larger than the shear forces of 0.15 V/W predicted by the static analysis. The larger shear force obtained by the dynamic analysis is attributed to the dynamic amplification, which is a known behavior of RC wall buildings (Priestley and Amaris 2003; Moehle 2015).

Table IV- 3: Maximum base shear forces and corresponding roof drift ratios predicted with the three seismic records.

Seismic record	Roof drift ratio	Time step (s)	Max V/W
SN	0.14	70.19	0.34
SC	0.15	73.06	0.26
SPA	0.08	73.84	0.30

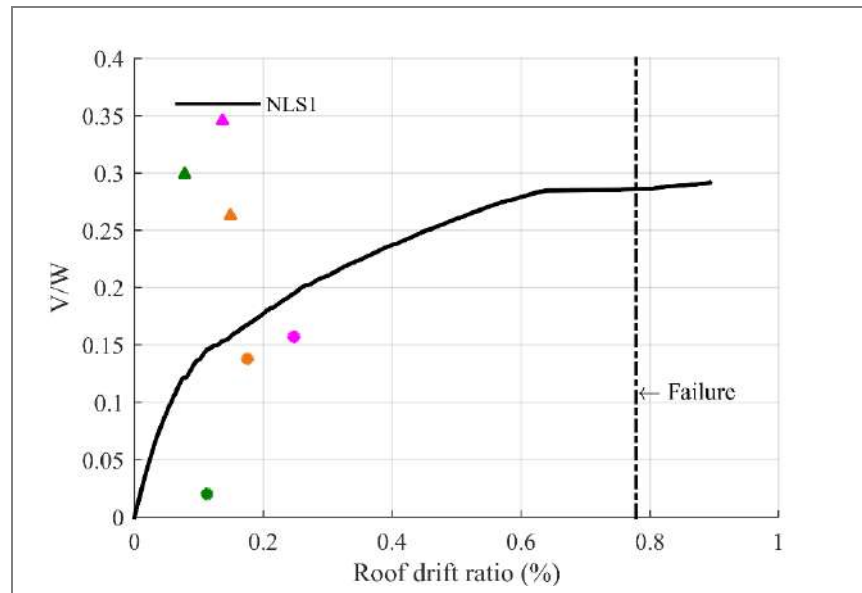


Figure 4- 8: Non-linear static results compared with the maximum values predicted with dynamic analysis, NLS1 model.

Figure 4- 9 compares the forces at the base of the two walls obtained by the static and the dynamic analysis. For the dynamic analysis, the points of maximum displacements identified in

Figure 4- 2 are considered, using the same marker colors used in previous figures. The color of the markers are magenta, orange and green, for the seismic records SN, SC and SPA, respectively. Results related to the WL wall are presented with point markers and the related with the WR wall with cross markers.

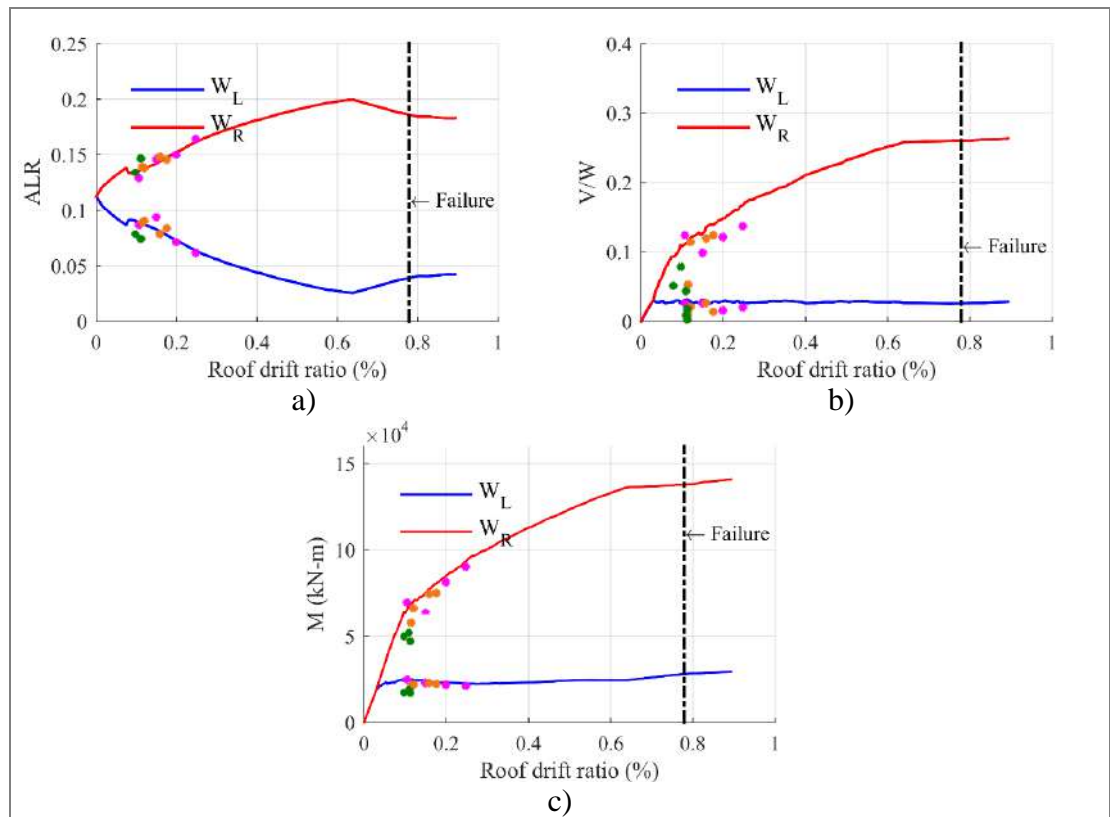


Figure 4- 9: Forces at the base of the walls for the NLS1 model predicted by the static and dynamic analyses: a) Axial load ratio; b) Normalized shear force, and c) Bending moment.

Regarding the ALR, Figure 4- 9a) shows that the results predicted by the non-linear static analysis are a reasonable estimation of the values predicted by the non-linear dynamic analyses. At the maximum roof drift ratio predicted by the non-linear dynamic analyses (0.25%), the maximum ALR was 0.164%, which is 1.5% larger than the ALR of 0.161% of the static response. Finally, it is expected that larger forces will be predicted in the dynamic response as the roof displacement increases.

Figure 4- 9b) shows that the trend of the base shear distribution between the two walls is similar for the static and dynamic analysis. The wall subjected to compressive seismic forces is the one that withstood the majority of the base shear, whereas the

shear force of the other wall stays relatively constant. For the dynamic analyses the shear forces withstood by the compressed wall corresponds to about 85% of the total base shear of the case study building. This same trend is observed for the maximum dynamic base shear force (triangles in Figure 4- 8); the WR wall takes in average 83% of the total base shear force. Instead, for the lineal dynamic analysis, the distribution of the base shear force between walls is equitable.

Figure 4- 9c) shows that the distribution of the moment between the two walls predicted by the dynamic analyses are also similar to the distribution predicted by the static analysis. From the plot is possible to appreciate that the wall subjected to compressive seismic forces withstood the major portion of the base moment and the moment on the tensioned wall remained almost constant. At the maximum roof drift ratio predicted by the dynamic analyses (0.25%), the moment at the base of  $W_R$  (i.e.,  $W_C$  for the static case) is 4.3 times larger than that of  $W_L$ . For the static analysis and for the same roof drift ratio, the moment at the base of  $W_C$  is 4.1 times larger than that of  $W_T$ .

Finally, Figure 4-10 compares the degree of coupling obtained by the dynamic analyses with the one obtained with the static analysis. The degree of coupling for the dynamic analyses was computed at the instant of peak displacements identified in Figure 4- 2. The figure shows that the degree of coupling obtained by the dynamic analysis, from roof drift ratios between 0.12% and 0.23%, is comparable to the degree of coupling obtained for the static analysis. The degree of coupling of the dynamic analysis shown in Figure 4-10 varies from 12% and 27%.

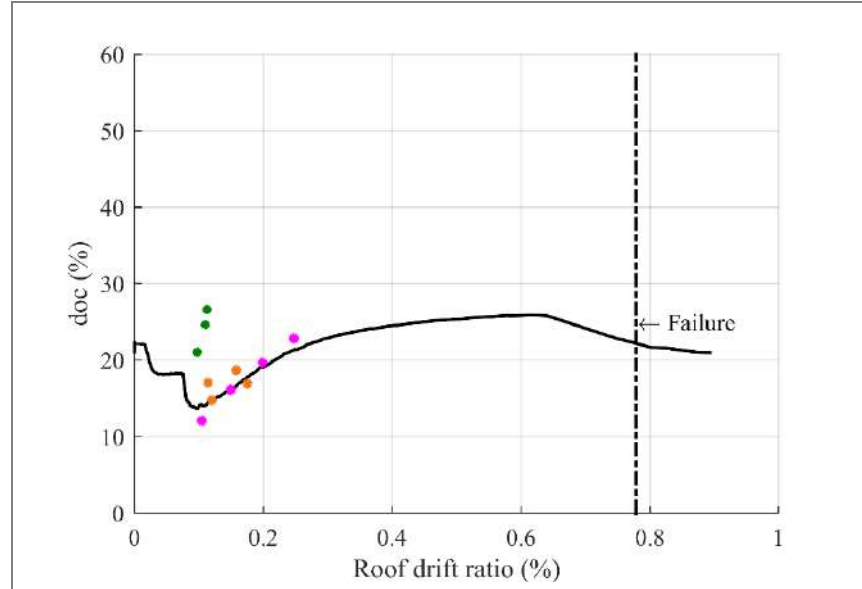


Figure 4- 10: Degree of coupling computed from the static and dynamic analysis

#### 4.5 Effect of the slab reinforcement in the dynamic response.

This section compares the predicted dynamic response of the case study building obtained from non-linear models with varying reinforcement ratio in the slabs. For this section, the SN seismic record was used to conduct the dynamic analyses. The response of the roof drift ratio and of the axial load ratio of the walls, predicted by the models NLS1, NLS2, and NLS3 are compared. Model NLS1 corresponds to the one used in the previous Sections 4.3 and 4.4 to obtain the dynamic responses.

For the two additional models, (NLS2 and NLS3) convergence problems also occurred and the responses were not obtained for the complete significant duration of the SN seismic record. However, it was possible to obtain the response beyond the maximum peak ground acceleration of the ground motions. Then, the obtained results allow drawing conclusions of the behavior of the case study building with varying reinforcement ratio in the slabs.

Figure 4- 11 compares the response of roof drift ratios obtained by the three models with varying slab reinforcement (NLS1, NLS2, and NLS3 models). The figure shows that until about 65 s, the roof drift ratio predicted by the three models are almost identical. At the instant of the maximum roof drift ratio of the NLS1 model (69.32 s), the roof drift ratios of the NLS2 and NLS3 models are also almost identical to the roof drift ratio of the NLS1 model (0.25%). Beyond that time, small differences of the roof drift ratio are noted between the models, and those differences become more evident after 70 s. At the time 70.28 s, the roof drift ratios predicted with NLS2 and NLS3 are 13% and 26% greater than that predicted with NLS1, respectively.

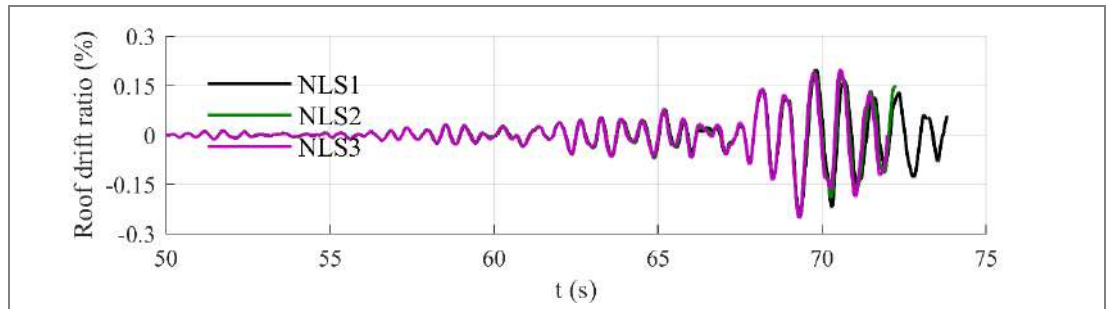


Figure 4- 11: Non-linear dynamic analysis results for NLS1, NLS2 and NLS3 models.

Similar than for the static analysis, the dynamic response of the building shows that the amount of reinforcement affects significantly the axial loads of the walls. Figure 4-12 compares the ALR for the wall  $W_R$  predicted by the three models. The figure shows that the ALR increases as the slab reinforcement increases. The maximum ALR predicted by the NLS1, NLS2 and NLS3 models are 0.18, 0.17 and 0.17, respectively. The ALR increases 18% when the reinforcement of the slabs was increased from  $\rho = 0.002$  in model NLS1 to  $\rho = 0.006$  in model NLS3. As mentioned in Section 3.6, the increase of the ALR of the walls induces larger compressive strains in the walls, and affects the deformation capacity of the building because of strains of failure could be reached earlier.

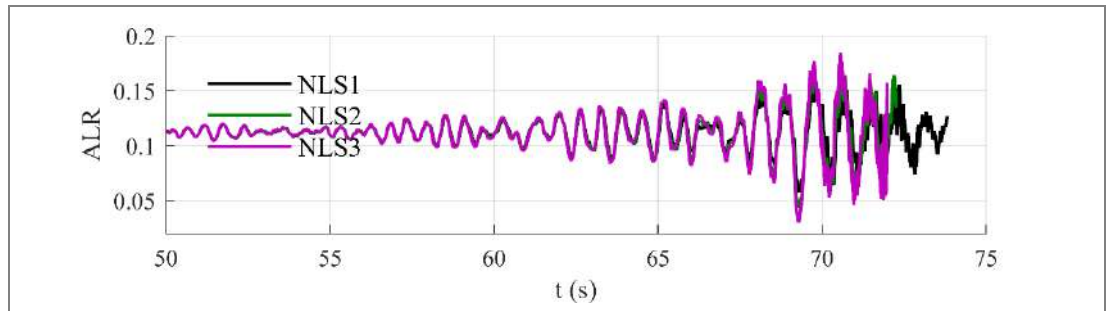


Figure 4- 12: Comparative Axial load ratio results in  $W_C$  from NLS1, NLS2 and NLS3 models.

## 5. CONCLUSIONS

This research presents an analytical investigation aimed to evaluate the seismic demands of walls in RC buildings with coupling slabs. The dissertation is divided into two parts, the first part corresponds to the chapter 2 and the second part corresponds to chapters 3 and 4. The first part considers linear models of existing RC buildings using the software ETABS. These models allowed quantifying the contribution of the coupling elements to the seismic demands of walls. The second part considers non-linear models of a case study building using the software DIANA. This second part is aimed to evaluate the effect of the non-linear behavior and the reinforcement ratio of the slabs on the seismic demands of the walls. From this part of the investigation, relevant conclusions about the building behavior, slab demands, and failure mode were drawn.

The first part of this research (Chapter 2) investigated the contribution of coupling elements to the seismic demands of axial load, shear, and moment of walls in existing RC buildings. The buildings were analyzed considering the 3D interaction of their structural elements using detailed elastic finite element models in ETABS. The influence of using different moments of inertia for the structural elements and different diaphragm assumptions for the slabs were evaluated. The seismic demands of the reference model (SR1) were obtained from linear analyses using reduced moment of inertia to account for the cracking and inelastic action near or beyond the yield level. The obtained results from this part of the research allow drawing the following conclusions:

- 1) The seismic axial load of the analyzed RC walls was mostly transferred by the slabs, which contributed more than 90% in six out of the eight analyzed walls. For the other two walls, the contribution of beams to the seismic axial load was 57% and 69%, exceeding the contributions of the slabs. For the wall connected to adjacent walls (U-SO), such adjacent walls contributed more than the beams to the seismic axial load.

- 2) Large seismic ALRs, up to 0.83, were predicted for the studied walls with the reference model and design-level ground motions. Additionally, for four out of the eight analyzed walls the seismic ALRs exceeded the ALRs obtained from dead load. Therefore, tensile forces are expected to develop at the first story of such walls when seismic forces induce tension forces.
- 3) Large variability of the seismic axial load, shear, and moment demand was predicted using different seismic records scaled at the same intensity. The simultaneous application of both horizontal components of the ground motions influenced this variability.
- 4) The moment profiles obtained for the studied walls are significantly different than common profiles of cantilever walls, which are commonly assumed by design codes (e.g., ACI 318). The obtained profiles were also different than profiles reported for coupled walls through coupling beams. This result suggests that a common design assumption to relate the roof displacement of the building with the curvature demand at the base of a wall (e.g., ACI 318) may be inadequate for the studied walls.
- 5) The assumed stiffness of structural elements showed a significant influence on the prediction of the seismic axial load demands of the studied walls. Increasing the slab stiffness from  $0.25I_g$  to  $0.40I_g$  increased the seismic axial load of the walls by 26% on average. When gross sections are considered, the seismic axial load increased on average by 2.2 times when compared to the reference model with effective stiffness (SR1). Additionally, the use of gross sections also exerts a significant influence on the shape and magnitude of shear and moment diagrams.
- 6) The assumed in-plane stiffness of the diaphragm showed negligible effect on the predicted seismic demand of axial load, shear, and moment. However, in one of the studied walls, it exerted an influence both in the magnitude and the shape of the shear and moment profiles.

The second part of this research (chapter 3 and chapter 4) investigated the non-linear seismic response of an RC structural wall building with coupling slabs. A building representing a residential structure in Chile was utilized as a case study, and the seismic response was assessed from non-linear static analyses using a 3D model with shell-type elements in DIANA. In chapter 3, seven models of the building were created to study the effects of the non-linear behavior of the slabs and the reinforcement ratio of the slabs on the seismic response of the structure. The accuracy of models with linear slabs and reduced moment of inertia of slabs to represent the non-linear response of the structure was also studied. In chapter 4, the results obtained from the static analysis were corroborate by means of non-linear dynamic analysis.

Firstly, important effects were observed when non-linear behavior was considered in both walls and slabs. The following conclusions can be draw from the static analysis of the full non-linear model NLS1:

- The yielding of slab reinforcement was registered prior to yielding of wall reinforcement at a roof drift ratio of 0.25%. At the predicted failure of the building, the maximum strain in the slabs reached 1.06%, whereas the maximum strain in the walls only reached 0.42%. The strains of the slab reinforcement reached the yield strain along the whole corridor width in almost all the stories of the building.
- The coupling axial loads transferred by the slabs generated a significant variation in the axial load of the walls, equivalent to 78% of the gravitational axial load of the walls.
- The bending moment at the base of the wall subjected to larger axial load was 4.9 times larger than the moment of the wall subjected to less axial load. This difference is attributed to the asymmetric T-shape of the walls, which generate different moment capacity of in the two loading directions. The variation of the axial loads transferred by the slabs also affected the moment capacity of the two walls.

- The shear force at the base of the walls is also concentrated in one of them. The shear force at the base of the wall subjected to larger axial load reached about 90% of the total base shear of the structure.

Secondly, the results of the non-linear static analysis allow also concluding about the effect of the reinforcement ratio of the slabs on the seismic response of the structure:

- The strength capacity of the case study building increased as the slab reinforcement increased, whereas the deformation capacity decreased as the slab reinforcement increased. The maximum base shear at failure was 20% larger, and the roof drift ratio at failure was 20% lesser, when the reinforcement in the slabs was increased three times.
- The increment of three times the reinforcement ratio in slabs generated an increment of 27% in the seismic axial load ratio transferred to the compressed wall. Consequently, the concrete compressive strain at failure (0.008), was reached at lower roof drift ratio in the model with larger slab reinforcement ratio.
- The bending moment at the base of the compressed wall also increased as the slab reinforcement increased. Larger amount of slab reinforcement transferred larger axial loads to the compressed wall, increasing its flexural capacity.

Results of the non-linear dynamic analyses allowed to corroborate the behavior predicted through the non-linear static analysis. The non-linear dynamic analyses also showed that the ALR in one wall increased while the ALR in the other wall decreased. The dynamic analysis also showed that the wall that is under compression (due to the seismic action) took the most of the base shear, while the base shear in the other wall reached a limit and remained almost constant. This behavior was also predicted by the dynamic analyses for the bending moments withstood by the walls. Moreover, the dynamic analyses allowed to identify the dynamic amplification of the base shear, since dynamic base shear forces larger than the static forces were predicted.

Additionally, with respect to the accuracy of models with linear slabs with reduced moment of inertia to represent the non-linear response of the building (assessed through non-linear static analyses), the following statements can be made:

- The strength capacity of the case study building with linear slabs decreased as the moment of inertia of the slabs decreased. The lateral strength of the model with 10% moment of inertia of the slabs (NLS10) is 23% lower than that of the model with non-reduced moment of inertia of slabs (NLS100). In addition, the deformation capacity of the model NLS10 increased 27% compared to that of the model NLS100.
- The model NLS10 (with 10% of the moment of inertia of the slabs), was the model with linear slabs that better predicted the maximum strength and deformation capacity of the model with non-linear slabs (NLS1). Nevertheless, the force-displacement response of the structure was underestimated with the model NLS10.
- The model NLS25 predicted accurately the force-displacement response of the model NLS1 with non-linear slabs until the design displacement.
- None of the considered models with reduced moment of inertia for the slabs was able to predict accurately the force-displacement relationship of the model with non-linear slab behavior.

Finally, based on the obtained results of this thesis, the following recommendation for the design of RC walls buildings can be made:

- It was observed that models with non-linear walls and linear slabs do not reproduce accurately the full non-linear behavior of the case study building. Full non-linear models of RC wall buildings demand high computational efforts and common softwares used in design offices do not allow modelling the non-linear behavior of the slabs (e.g. PERFORM 3D), then considering the slabs as linear elements results a reasonable alternative. Therefore, for such non-linear models with linear slabs it is recommended to

simulate the slabs using a moment of inertia of  $0.25I_g$  to capture the behavior until the ultimate displacement and a moment of inertia between  $0.10I_g$  and  $0.25I_g$  for analyses aimed to identify the ultimate strength and displacement capacity of the buildings.

- The additional slab reinforcement, commonly used by design offices in Chile to increase the slabs strength, is detrimental for the seismic behavior of RC wall buildings. Even though the additional reinforcement increases the lateral strength of the building, it decreases the deformation capacity of the building. It is not recommended to increase the reinforcement in coupling slabs to avoid affecting the deformation capacity of the buildings.

Future work to study the seismic demands in RC buildings with coupling slabs may consider buildings with different number of stories and structural configurations. Additionally, the coupling effect when buildings sways in the two directions can be studied. Future studies of the case study building can consider additional non-linear dynamic analyses aimed to review the response of the slabs during time and identify the sequence of yielding along the building height. However, significant computational time and large storage capacity may be required to collect the results. Experimental analyses of RC walls with coupled slabs are also recommended to corroborate the results presented in this investigation and to further study the seismic behavior of RC wall buildings with coupling slabs.

## REFERENCES

- Aktan AE, Bertero VV. (1984). Seismic response of R/C frame-wall structures. *Journal of Structural Engineering*, **110**(8), 1803-1821. [http://dx.doi.org/10.1061/\(ASCE\)0733-9445\(1984\)110:8\(1803\)](http://dx.doi.org/10.1061/(ASCE)0733-9445(1984)110:8(1803)).
- Aksogan O, Turkozer CD, Emsen E, Resatoglu R. (2014). Dynamic analysis of non-planar coupled shear walls with stiffening beams using Continuous Connection Method. *Thin-Walled Structures*, **82**, 95-104. <http://dx.doi.org/10.1016/j.tws.2014.03.018>.
- Alarcón C, Hube MA, De la Llera JC. (2014). Effect of axial loads in the seismic behavior of reinforced concrete walls with unconfined wall boundaries. *Engineering Structures*, **73**, 13-23. <http://dx.doi.org/10.1016/j.engstruct.2014.04.047>.
- Alarcón C, Hube MA, Jünemann R, de la Llera JC. (2015). Characteristics and displacement capacity of reinforced concrete walls in damaged buildings during 2010 Chile earthquake. *Bulletin of Earthquake Engineering*, **13** (4), 1119-1139. <http://dx.doi.org/10.1007/s10518-015-9727-0>.
- Albert KW Lim. (1989). Non-linear Response of Reinforced Concrete Coupling Slabs with Drop Panel in Earthquake-resisting Shear Wall Structures. Master of Engineering Thesis. McGill University.
- American Concrete Institute (ACI) (1995). Building code requirements for structural concrete and commentary, (ACI 318-95), Farmington Hills, Michigan.
- American Concrete Institute (ACI) (2008). Building code requirements for structural concrete and commentary (ACI 318-08), Farmington Hills, Michigan.
- American Concrete Institute (ACI) (2014). Building code requirements for structural concrete and commentary, (ACI 318-14), Farmington Hills, Michigan.
- American Concrete Institute (ACI) (2019). Building code requirements for structural concrete and commentary, (ACI 318-19, Farmington Hills, Michigan.
- American Society of Civil Engineers. (ASCE) (2017). 7-16. Minimum design loads and associated criteria for buildings and other structures. Reston, Virginia.
- American Society of Civil Engineers. (ASCE) (2017). 41-17. Seismic Evaluation and Retrofit of Existing Buildings. Reston, Virginia.
- Arias A. (1970). A Measure of earthquake intensity. In *Seismic design for nuclear power plants*, R. Hanson, ed, MIT Press 1970, Cambridge, Massachusetts, 438-483.
- Arteta CA, To DV, Moehle JP. (2014). Experimental response of boundary elements of code-compliant reinforced concrete shear walls. In *Proceedings of 10<sup>th</sup> US National Conference on Earthquake Engineering*, Anchorage, Alaska.
- Asociación Chilena de Sismología e Ingeniería Antisísmica. Performance-Based Seismic Design: an alternative procedure to the analysis and design seismic of buildings. ACHISINA. 2017. (In Spanish)

- Bertero VV, Atkan AE, Charney F, Sause R. (1985). Earthquake simulator tests and associated experiments, analytical and correlation studies of one-fifth scale model. Earthquake effects on reinforced concrete structures, U.S. – Japan research. *ACI Publication SP-84*, 375–424.
- Blandón CA, Arteta CA, Bonett RL, Carrillo J, Beyer K, Almeida JP. (2018). Response of thin lightly reinforced concrete walls under cyclic loading. *Engineering Structures*. **176**, 175–187. <http://dx.doi.org/10.1016/j.engstruct.2018.08.089>.
- Boroschek, RL, Contreras V, Kwak DY, Stewart JP. (2012). Strong ground motion attributes of the 2010 Mw 8.8 Maule, Chile, earthquake. *Earthquake Spectra*, **28** (S1), S19-S38. <https://doi.org/10.1193%2F1.4000045>.
- Bruegen, BL. Performance of T-shaped reinforced concrete structural walls under multi-directional loading. 2010. PhD Thesis, University of Minnesota, US.
- Brunesi E, Peloso S, Pinho R, Nascimbene R. (2017). Cyclic testing of a full-scale cast-in-place reinforced concrete wall-slab-wall structure representative of the Groningen building stock. Report EUC095/2017U, *EUCENTRE*, Pavia, IT.
- Brunesi E, Peloso S, Pinho R., Nascimbene R. (2018). Cyclic testing and analysis of a full-scale cast-in-place reinforced concrete wall-slab-wall structure. *Bulletin of Earthquake Engineering*, **16** (10), 4761-4796.
- Building Seismic Safety Council. (BSSC)(2015). NEHRP Recommended Seismic Provisions for New Buildings and Other Structures, 2015 Edition, Volume I: Part 1 Provisions, Part 2 Commentary, FEMA Rep. No. P-1050-1.
- Cando MA, Hube MA, Parra PF, Arteta CA. (2020). Effect of stiffness on the seismic performance of code-conforming reinforced concrete shear wall buildings. *Engineering Structures*. **219**, 110724. <http://dx.doi.org/10.1016/j.engstruct.2020.110724>.
- Carpenter LD, Naeim F, Lew M, Youssef NF, Rojas F, Saragoni GR, Adaros MS. (2011). Performance of tall buildings in Viña del Mar in the 27 February 2010 offshore Maule, Chile earthquake. *The Structural Design of Tall and Special Buildings*, **20**(1), 17–36. <http://dx.doi.org/10.1002/tal.672>.
- Centro Sismológico Nacional (CSN), Universidad de Chile, Facultad de ciencias Físicas y Matemáticas: <http://www.sismologia.cl/>. Accessed march 2016.
- Chacón MF, de la Llera JC, Hube MA, Marques J, Lemnitzer A. (2017). Epistemic uncertainty in the seismic response of RC free-plan buildings. *Engineering Structures*, **141**, 687-702. <http://dx.doi.org/10.1016/j.engstruct.2017.03.015>.
- Chandran R, Kartha U, Prabhakaran R. (2014). Comparative study on solid and coupled shear Wall. *International Journal of Civil Engineering & Technology*. **5**, 117133.
- Chen B, Tan J, Oyang Y. (2011). An improved simulation model of shear wall structures of tall building. *Procedia Engineering*, **12**, 127-132. <http://dx.doi.org/10.1016/j.proeng.2011.05.021>.
- Chopra AK. (2016). Dynamics of Structures: Theory and Applications to Earthquake Engineering. ISBN: 978-0-134-55512-6. Pearson.

- Chowdhury SR and Orakcal K. (2013). Analytical Modeling of Columns with Inadequate Lap Splices. *ACI Structural Journal*, **110**(5), 765-744.
- Comité Euro-International du Béton. CEB-FIP model code 1990, Thomas Telford, London, 1990.
- Computers and Structures, Inc. (CSI) (2010). ETABS 2010. Extended Tridimensional Analysis of Building Structures.
- Computers and Structures, Inc. (CSI) (2017). SAP 2000 v19.2.1. Berkeley, California.
- Dabaghi M, Saad G, Allhassania N. (2019). Seismic Collapse Fragility Analysis of Reinforced Concrete Shear Wall Buildings. *Earthquake Spectra*, **35** (1), 383-404. <http://dx.doi.org/10.1193/121717EQS259M>.
- Dashti F, Dakhal RP, Pampanin S. (2014). Numerical simulation of shear wall failure mechanisms. In *Proceedings of New Zealand Society for Earthquake Engineering 2014 Conference*, Auckland, New Zealand.
- Deaton JB. (2013). Non-linear finite element analysis of reinforced concrete exterior beam-column joints with non-seismic detailing. Diss. Georgia Institute of Technology.
- Deger ZT and Wallace JW. (2015). Collapse assessment of the Alto Rio building in the 2010 Chile earthquake. *Earthquake Spectra*, **31** (3), 1397-1425. <http://dx.doi.org/10.1193/060812EQS209M>.
- Englekirk RE. (2003). Seismic design of reinforced and precast concrete buildings. 848 pages. ISBN: 978-0-471-08122-7. John Wiley & Sons.
- Estay CG. (2008). Characteristics of Reinforced Concrete Walls designed in Chile. Civil Engineering Thesis. University of Chile. (in Spanish).
- Federal Emergency Manage Agency FEMA (1997). Guidelines for the seismic rehabilitation of buildings. (FEMA-273), Washington, D.C.
- Filippou FC, Bertero VV, Popov EP. (1983). Effects of Bond Deterioration on Hysteretic Behavior of Reinforced Concrete Joints. Earthquake Engineering Research Center, University of California, Berkeley, Tech. Rep. EERC **83** (19), 137-147.
- Fischinger M, Kante P, Isakovic T. (2017). Shake-table response of a coupled RC wall with thin T-shaped piers. *Journal of Structural Engineering*, **143**(5), 04017004. [http://dx.doi.org/10.1061/\(ASCE\)ST.1943-541X.0001718](http://dx.doi.org/10.1061/(ASCE)ST.1943-541X.0001718)
- Fox M, Sullivan T, Beyer K. (2014a). Comparison of force-based and displacement-based design approaches for RC coupled walls in New Zealand. *Bulletin of the New Zealand Society for Earthquake Engineering*, **47** (EPFL-ARTICLE-202735), 190-205. <http://dx.doi.org/10.5459/bnzsee.47.3.190-205>.
- Fox M, Sullivan T, Beyer K. (2014b). Capacity design of coupled RC walls. *Journal of Earthquake Engineering*, **18** (5), 735-758. <http://dx.doi.org/10.1080/13632469.2014.904255>.

- Gallardo JA, De la Llera JC, Santa María H, Chacón MF. (2021). Damage and sensitivity analysis of a reinforced concrete wall building during the 2010, Chile earthquake. *Engineering Structures*, **240**, 112093. <http://dx.doi.org/10.1016/j.engstruct.2021.112093>.
- Gogus A, Wallace JW. (2015). Seismic safety evaluation of reinforced concrete walls through FEMA P695 methodology. *Journal of Structural Engineering*, **141**(10), 04015002. [http://dx.doi.org/10.1061/\(ASCE\)ST.1943-541X.0001221](http://dx.doi.org/10.1061/(ASCE)ST.1943-541X.0001221).
- Guendelman T, Lindenberg J. (2010). Change in seismic demands in buildings. In Seminar Earthquake Effects on the New Seismic and Structural Design in Chile, ICH November 2010 (in Spanish).
- Gullu MF and Orakcal K. (2021). Non-linear finite element modeling of reinforced concrete walls with varying aspect ratios. *Journal of Earthquake Engineering*. **25**(10), 2033-2064. <https://doi.org/10.1080/13632469.2019.1614498>.
- Habibullah A. (1992): ETABS users' manual. Computers and Structures, Inc., Berkeley, California, USA.
- Hamburger R, Moehle J, Baker J, Bray J, Crouse CB, Deierlein G, Hooper J, Lew M, Maffei J, Mahin S, Malley J, Naeim F, Stewart J, Wallace JW. (2017). Tall buildings initiative: Guidelines for performance-based seismic design of tall buildings. Pacific Earthquake Engineering Research Center. PEER Report 2017/06.
- Harries KA. (1995). Seismic design and retrofit of coupled walls using structural steel. PhD Thesis, McGill University, US.
- Harries KA. (2001). Ductility and deformability of coupling beams in reinforced concrete coupled walls. *Earthquake Spectra*, **17** (3), 457-478. <http://dx.doi.org/10.1193/1.1586184>.
- Harries KA, Moulton JD, Clemson RL. (2004). Parametric study of coupled wall behavior-implications for the design of coupling beams. *Journal of Structural Engineering*, **130** (3), 480-488. [http://dx.doi.org/10.1061/\(ASCE\)0733-9445\(2004\)130:3\(480\)](http://dx.doi.org/10.1061/(ASCE)0733-9445(2004)130:3(480)).
- Haselton CB, Liel AB, Deierlein GG. (2009). Simulating structural collapse due to earthquakes: model idealization, model calibration, and numerical solution algorithms. In *Proceedings of ECCOMAS Computational Methods in Structural Dynamics and Earthquake Engineering (COMPDYN)*, Rhodes, Greece.
- Hossain KMA. (2003). Non-linear performance of slabs in coupled shear wall structures. *Advances in Structural Engineering* 2003, **6**(4), 339-352. <http://dx.doi.org/10.1260/136943303322771718>.
- Hube MA, Marihuén A, De la Llera JC, Stojadinovic B. (2014). Seismic behavior of slender reinforced concrete walls. *Engineering Structures*, **80**, 377-388. <http://dx.doi.org/10.1016/j.engstruct.2014.09.014>.
- Instituto Nacional de Normalización, INN (1986). Structural design of buildings - permanent loads and overloads of use, NCh1537.Of.1986. Santiago, Chile (in Spanish).
- Instituto Nacional de Normalización, INN (2008). Reinforced concrete – design and calculation requirement, NCh430 Of.2008. Santiago, Chile (in Spanish).

- Instituto Nacional de Normalización, INN (2010). Structural design - General provisions and load combinations, NCh3171.Of.2010. Santiago, Chile (in Spanish).
- Instituto Nacional de Normalización, INN (1996). Earthquake resistant design of buildings, NCh433 Of.1996. Santiago, Chile (in Spanish).
- Jünemann R, de La Llera JC, Hube MA, Cifuentes LA, Kausel E. (2015). A statistical analysis of reinforced concrete wall buildings damaged during the 2010, Chile earthquake. *Engineering Structures*, **82**, 168-185. <http://dx.doi.org/10.1016/j.engstruct.2014.10.014>.
- Jiang H, Kurama YC. (2010). Analytical Modeling of Medium-Rise Reinforced Concrete Shear Walls. *ACI Structural Journal*, **107** (4).
- Jünemann R, de la Llera JC, Hube MA, Vásquez J, Chacón MF. (2016a). Study of the damage of reinforced concrete shear walls during the 2010, Chile earthquake. *Earthquake Engineering and Structural Dynamic*, **45** (10), 1621-1641. <http://dx.doi.org/10.1002/eqe.2750>.
- Jünemann R, de la Llera JC, Hube MA, Vásquez J, Chacón MF. (2016b). Inelastic finite element models to assess earthquake damage of RC Wall buildings. In *Proceedings of New Zealand Society for Earthquake Engineering – 2016 Technical Conference & AGM*, Christchurch, Nueva Zealand.
- Kam WY, Pampanin S, Elwood K. (2011). Seismic performance of reinforced concrete buildings in the 22 February Christchurch (Lyttleton) earthquake. *Bulletin of the New Zealand Society for Earthquake Engineering*, **44**(4), 239-278. <https://doi.org/10.5459/bnzsee.44.4.239-278>.
- Kaushik S and Dasgupta K. (2016). Seismic damage in shear wall-slab junction in RC buildings. *Procedia Engineering*, **144**, 1332-1339. <http://dx.doi.org/10.1016/j.proeng.2016.05.162>.
- Kolozvari K, Orakcal K, Wallace JW. (2015). Modeling of cyclic shear-flexure interaction in reinforced concrete structural walls. I: Theory. *Journal of Structural Engineering*, **141**(5), 04014135. [http://dx.doi.org/10.1061/\(ASCE\)ST.1943-541X.0001059](http://dx.doi.org/10.1061/(ASCE)ST.1943-541X.0001059).
- Kolozvari K, Tran TA, Orakcal K, Wallace JW. (2015). Modeling of cyclic shear-flexure interaction in reinforced concrete structural walls. II: Experimental validation. *Journal of Structural Engineering*, **141**(5), 04014136. [http://dx.doi.org/10.1061/\(ASCE\)ST.1943-541X.0001083](http://dx.doi.org/10.1061/(ASCE)ST.1943-541X.0001083)
- Kolozvari K, Arteta C, Fischinger M, Gavridou S, Hube M, Isaković T, et al. (2018). Comparative study on state-of-the-art macroscopic models for planar reinforced concrete walls. *ACI Struct Journal*, **115**(6), 115-1637. <http://dx.doi.org/10.14359/51710835>.
- Kolozvari K, Biscombe L, Dashti F, Dhakal RP, Gogus A, Gullu MF, Henry RS, Massone, LM, Orakcal K, Rojas F, Shegay A, and Wallace J. (2019). State-of-the-art in non-linear finite element modeling of isolated planar reinforced concrete walls. *Engineering Structures*, **194**(June), 46–65. <http://dx.doi.org/10.1016/j.engstruct.2019.04.097>
- Lepage A. (1998). Non-linear drift of multistory RC structures during earthquakes. In *Proceedings of Sixth National Conference on Earthquake Engineering*, Seattle, Washington.

- Lehman DE, Turgeon JA, Birely C, Hart CR, Marley KP, Kuchma DA, Lowes N. (2013): Seismic behavior of a modern concrete coupled wall. *Journal of Structural Engineering*, **139**(8), 1371-1381. [http://dx.doi.org/10.1061/\(ASCE\)ST.1943-541X.0000853](http://dx.doi.org/10.1061/(ASCE)ST.1943-541X.0000853).
- Lu X, Lu X, Zhang W, Ye L. (2011). Collapse simulation of a super high-rise building subjected to extremely strong earthquakes. *Science China Technological Sciences*, **54**(10), 2549. <http://dx.doi.org/10.1007/s11431-011-4548-0>.
- Lu Y, Henry RS, Gultom R, Ma QT. (2016). Cyclic testing of reinforced concrete walls with distributed minimum vertical reinforcement. *Journal of Structural Engineering*, **143**(5), 04016225. [http://dx.doi.org/10.1061/\(ASCE\)ST.1943-541X.0001723](http://dx.doi.org/10.1061/(ASCE)ST.1943-541X.0001723).
- Lu Y, Panagiotou M. (2016). Three-dimensional beam–truss model for reinforced concrete walls and slabs – part 2: modeling approach and validation for slabs and coupled walls. *Earthquake Engineering & Structural Dynamics* **45** (11), 1707-1724. <http://dx.doi.org/10.1002/eqe.2720>.
- Lu Y, Panagiotou M, Koutromanos I. (2014). Three-Dimensional Beam-Truss Model for Reinforced-Concrete Walls and Slabs Subjected to Cyclic Static or Dynamic Loading. *Pacific Earthquake Engineering Research Center*. PEER Report 2014/18.
- Magna-Verdugo CE, Kunnath SK. (2014). Non-linear response analysis of reinforced concrete shear walls using multispring macro-models. In *Proceedings of 10th National US Conference on Earthquake Engineering*, Anchorage, Alaska.
- Mander JB, Priestley MJ, Park R. (1988). Theoretical stress-strain model for confined concrete. *Journal of structural engineering*, **114**(8), 1804-1826. [http://dx.doi.org/10.1061/\(ASCE\)0733-9445\(1988\)114:8\(1804\)](http://dx.doi.org/10.1061/(ASCE)0733-9445(1988)114:8(1804)).
- Massone LM, Bonelli P, Lagos R, Lüders C, Moehle J, Wallace JW. (2012). Seismic design and construction practices for RC structural wall buildings. *Earthquake Spectra*, **28**(S1), S245-S256. <http://dx.doi.org/10.1193/1.4000046>.
- Massone LM, Manríquez I, Díaz S, Rojas F, Herrera R. (2019). Experimental cyclic response of RC walls with setback discontinuities. *Engineering Structures*, **178**, 410-422. <http://dx.doi.org/10.1016/j.engstruct.2018.10.054>.
- Massone LM, Manríquez I, Díaz S, Rojas F, Herrera R. (2019). Understanding the Cyclic Response of RC Walls with Setback Discontinuities Through a Finite Element Model and a Strut-and-Tie Model. *Bulletin of Earthquake Engineering*, 1-17. <http://dx.doi.org/10.1007/s10518-019-00579-3>.
- Massone LM, Polanco P, Herrera P. (2014). Experimental and analytical response of RC wall boundary elements. In *Proceedings of 10<sup>th</sup> National US Conference on Earthquake Engineering*, Anchorage, Alaska.
- Meftah SA, Mohri F, Daya EM. (2013). Seismic behavior of RC coupled shear walls with strengthened coupling beams by bonded thin composite plates. *KSCE Journal of Civil Engineering*, **17** (2), 403-414. <http://dx.doi.org/10.1007/s12205-013-1286-9>.
- Mejia LG, Ortiz JC, Osorio LI. RC Structural Wall Buildings. World Housing Encyclopedia, Report 109.

- Menegotto M and Pinto PE. (1973). Method of Analysis for Cyclically Loaded Reinforced Concrete Plane Frames Including Changes in Geometry and Nonelastic Behavior of Elements Under Combined Normal Force and bending. In *IABSE Symposium on Resistance and ultimate Deformability of Structures Acted on by Well-Defined Repeated Loads*, Lisbon.
- Ministry of Housing and Urbanism, MINVU, DS61, Earthquake resistant design of buildings, replacing D.S. N 117 2010. Official Diary, 13 December 2011 (in Spanish).
- Ministry of Housing and Urbanism, MINVU, DS60, Reinforced concrete design code, replacing D.S N 118. 2010, Official Diary; 13 December 2011 (in Spanish).
- Moehle JP. (1992). Displacement-based design of RC structures subjected to earthquakes. *Earthquake Spectra*, **8** (3), 403-428. <http://dx.doi.org/10.1193/1.1585688>.
- Moehle JP. (2015). Seismic design of reinforced concrete buildings. 760 pages. ISBN: 978-0-07-183945-7. McGraw-Hill Education.
- National Institute of Standards and Technology (NIST) (2014). Recommendations for seismic design of reinforced concrete wall buildings based on studies of the 2010, Maule, Chile Earthquake. NIST GCR 14-917-25. US Department of Commerce. Gaithersburg, Montgomery.
- Orakcal K, Wallace JW, Conte JP. (2004). Flexural modeling of reinforced concrete walls-model attributes. *ACI Structural Journal*, **101** (5), 688-698.
- Orakcal K, Wallace JW, Conte JP. (2006). Flexural modeling of reinforced concrete walls-experimental verification. *ACI Structural Journal*, **103** (2), 196-206.
- Panagiotou M, Restrepo JI, Conte JP. (2011). Shake table test of a 7-story full scale reinforced concrete wall building slice, phase I: rectangular walls. *Journal of Structural Engineering*, **137** (6), 691-704. [https://doi.org/10.1061/\(ASCE\)ST.1943-541X.0000332](https://doi.org/10.1061/(ASCE)ST.1943-541X.0000332).
- Panagiotou M, Kim G, Barbosa A, Restrepo JI. (2009). Response verification of a reinforced concrete bearing wall building located in an area of high seismic hazard. *Rep. prepared for the Portland Cement Association*.
- Panagiotou M and Restrepo JI. (2009). Dual-plastic hinge design concept for reducing higher mode effects on high-rise cantilever wall buildings. *Earthquake Engineering and Structural Dynamics*, **38** (2), 1359–1380. <http://dx.doi.org/10.1002/eqe.905>.
- Panagiotou M and Restrepo JI. (2010). Displacement-based method of analysis for regular reinforced-concrete wall buildings: Application to a full-scale 7-story building slice tested at UC–San Diego. *Journal of Structural Engineering*, **137**(6), 677-690. [http://dx.doi.org/10.1061/\(ASCE\)ST.1943-541X.0000333](http://dx.doi.org/10.1061/(ASCE)ST.1943-541X.0000333).
- Panagiotou M, Restrepo JI, Schoettler M, Kim G. (2012). Non-linear cyclic truss model for reinforced concrete walls. *ACI Structural Journal*, **109**(2), 205-214.
- Papadrakakis M, Charnpis DC, Tsompanakis Y, Lagaros ND. (2008). Computational Structural Dynamics and Earthquake Engineering: Structures and Infrastructures. 613 pages. ISBN: 978-0415452618. CRC Press.
- Paulay T and Taylor RG. (1981). Slab coupling of earthquake-resisting shearwalls. *Journal Proceedings*, **78**(2): 130-140.

- Paulay T. (1986). The design of ductile reinforced concrete structural walls for earthquake resistance. *Earthquake Spectra*, **2** (4), 783-823. <http://dx.doi.org/10.1193/1.1585411>.
- Parra PF and Moehle JP. (2014). Lateral buckling in reinforced concrete walls. In *Proceedings of 10<sup>th</sup> US National Conference on Earthquake Engineering*, Anchorage, Alaska.
- Pennucci D, Sullivan TJ, Calvi GM. (2015). Inelastic higher-mode response in reinforced concrete wall structures. *Earthquake Spectra*, **31** (3), 1493-1514. <http://dx.doi.org/10.1193/051213EQS123M>.
- Pozo JD, Hube MA, Kurama YC. (2020). Quantitative assessment of non-linear macro-models for global behavior and design of planar RC walls. *Engineering Structures*. **224**, 111190. <http://dx.doi.org/10.1016/j.engstruct.2020.111190>.
- Pozo JD, Hube MA, Kurama YC. (2021). Effect of material regularization in plastic hinge integration analysis of slender planar RC walls. *Engineering Structures*. **239**, 112302. <http://dx.doi.org/10.1016/j.engstruct.2021.112302>.
- Pugh JS, Lowes LN, Lehman DE. (2015). Non-linear line-element modeling of flexural reinforced concrete walls. *Engineering Structures*, **104**, 174-192. <http://dx.doi.org/10.1016/j.engstruct.2015.08.037>.
- Pugh JS, Lowes LN, Lehman DE. (2017). Accurate methods for elastic seismic demand analysis of reinforced concrete walled buildings. *Journal of Structural Engineering*, [http://dx.doi.org/10.1061/\(ASCE\)ST.1943-541X.0001669](http://dx.doi.org/10.1061/(ASCE)ST.1943-541X.0001669).
- Priestley MJ and Amaris A. (2003). Dynamic amplification of seismic moments and shear forces in cantilever walls. *Proceedings, Fib Symposium, Concrete Structures in Seismic Regions*, Athens, Greece.
- Ramos L and Hube M A. (2017a). Seismic assessment of reinforced concrete buildings with coupled walls. In *Proceedings of the 16th World Conf. on Earthquake Engineering*.
- Ramos L and Hube M A. (2017b). Efecto del modelamiento estructural en la demanda de carga axial sísmica en muros de edificios de concreto reforzado. In *Proceedings of VIII Congreso Nacional de Ingeniería Sísmica*.
- Ramos L and Hube M A. (2018). Contribution of coupling elements to the seismic axial load demands in walls of reinforced concrete buildings. In *Proceedings of 11th U.S National Conf. on Earthquake Engineering*.
- Ramos L and Hube MA. (2020). Contribution of coupling elements to the seismic demand of walls in reinforced concrete buildings. *Latin American Journal of Solids and Structures* 2020, 17(2).
- Ramos L and Hube M A. (2021). Seismic response of reinforced concrete wall buildings with non-linear coupling slabs. *Engineering Structures*, **234**, 111888. <http://dx.doi.org/10.1016/j.engstruct.2021.111888>.
- Rojas F, Naeim F, Lew M, Carpenter LD, Youssef NF, Saragoni GR, Adaros MS. (2011). Performance of tall buildings in Concepción during the 27 February 2010 moment magnitude

- 8.8 offshore Maule, Chile earthquake. *The Structural Design of Tall and Special Buildings*, **20**(1), 37–64. <http://dx.doi.org/10.1002/tal.674>.
- Santa María H, Hube MA, Rivera F, Yepes-Estrada C, Valcárcel JA. (2017). Development of national and local exposure models of residential structures in Chile. *Natural Hazards*, **86**(1), 55-79. DOI 10.1007/s11069-016-2518-3.
- Schwaighofer J and Collins MP. (1977). Experimental Study of the Behavior of Reinforced Concrete Coupling Slabs. *Journal Proceedings*, **74**(3), 123-127.
- Segura Jr and Wallace JW. (2018). Seismic Performance Limitations and Detailing of Slender Reinforced Concrete Walls. *ACI Structural Journal*, **115**(3): 849-859. <http://dx.doi.org/10.14359/51701918>.
- Sezen H and Moehle JP. (2004). Shear strength model for lightly reinforced concrete columns. *Journal of Structural Engineering*, **130**(11), 1692-1703. [http://dx.doi.org/10.1061/\(ASCE\)0733-9445\(2004\)130:11\(1692\)](http://dx.doi.org/10.1061/(ASCE)0733-9445(2004)130:11(1692)).
- Sritharan S, Beyer K, Henry RS, Chai YH, Kowalsky M, Bull D. (2014). Understanding poor seismic performance of concrete walls and design implications. *Earthquake Spectra*, **30**(1), 307-334. <http://dx.doi.org/10.1193/021713EQS036M>.
- Thomsen JH and Wallace JW. (1995). Displacement based design of reinforced concrete structural walls: an experimental investigation of walls with rectangular and t-shaped cross-sections: a dissertation. Diss. Clarkson University.
- Thomsen JH, and Wallace JW. (2004). Displacement-based design of slender reinforced concrete structural walls-experimental verification. *Journal of structural engineering*, **130**(4), 618-630. [http://dx.doi.org/10.1061/\(ASCE\)0733-9445\(2004\)130:4\(618\)](http://dx.doi.org/10.1061/(ASCE)0733-9445(2004)130:4(618)).
- TNO DIANA. 2017. DIANA finite element analysis user manual (Release 10. 2DIANA FEA BV, Delft, The Netherlands). Available at: <https://dianafea.com/> (accessed October 2018).
- Ugalde D, Parra PF, Lopez-Garcia D. (2018). Overstrength of 3D Fully Modeled RC Shear Wall Buildings. In *Proceedings of 11<sup>th</sup> US National Conference on Earthquake Engineering*, Los Angeles, California.
- Ugalde D, Parra PF, Lopez-Garcia D. (2019). Assessment of the seismic capacity of tall wall buildings using non-linear finite element modeling. *Bulletin of Earthquake Engineering*, 1-25. <http://dx.doi.org/10.1007/s10518-019-00644-x>.
- Ugalde D and Lopez-Garcia D. (2020). Analysis of the seismic capacity of Chilean residential RC shear wall buildings. *Journal of Building Engineering*, 101369. <http://dx.doi.org/10.1016/j.jobbe.2020.101369>.
- Universidad de Chile, Departamento de Ingeniería Civil and Oficina Nacional de Emergencia Chile (ONEMI) (2016). Earthquakes of Chile 2010, <http://terremotos.ing.uchile.cl/2010>. Accessed march 2016.
- Vásquez JA, De la Llera JC, Hube MA. (2016). A regularized fiber element model for reinforced concrete shear walls. *Earthquake Engineering & Structural Dynamics*, **45** (13), 2063-2083. <http://dx.doi.org/10.1002/eqe.2731>.

- Vásquez JA, Jünemann R, de la Llera JC, Hube MA, Chacón MF. (2020). Three-dimensional non-linear response history analyses for earthquake damage assessment: A reinforced concrete wall building case study. *Earthquake Spectra*, **37** (1), 235. <http://dx.doi.org/10.1177/8755293020944180>.
- Wallace JW, Massone LM, Bonelli P, Dragovich J, Lagos R, Lüders C, Moehle J. (2012). Damage and implications for seismic design of RC structural wall buildings. *Earthquake Spectra*, **28** (S1), S281-S299. <http://dx.doi.org/10.1193/1.4000047>.
- Westenenk B, de la Llera JC, Besa JJ, Jünemann R, Moehle J, Lüders C, Inaudi JA, Elwood K, Hwang SJ. (2012). Response of reinforced concrete buildings in Concepción during the Maule earthquake. *Earthquake Spectra*, **28** (S1), S257-S280. <http://dx.doi.org/10.1193/1.4000037>.
- Westenenk B, de la Llera JC, Jünemann R, Hube MA, Besa JJ, Lüders C, Inaudi JA, Riddell R, Jordán R. (2013). Analysis and interpretation of the seismic response of RC buildings in Concepción during the February 27, 2010 Chile Earthquake. *Bulletin of Earthquake Engineering*, **11** (1), 69–91. <http://dx.doi.org/10.1007/s10518-012-9404-5>.
- Wong PS, Vecchio FJ, Trommels H. (2002). VecTor2 & FormWorks user's manual. 2nd ed. Toronto: Analysis.
- Zhang P, Restrepo JI, Conte J P, Ou J. (2017). Non-linear finite element modeling and response analysis of the collapsed Alto Rio building in the 2010 Chile Maule earthquake. *The Structural Design of Tall and Special Buildings*, **26**(16), e1364. <http://dx.doi.org/10.1002/tal.1364>.